We are IntechOpen,
the world's leading publisher of Open Access books
Built by scientists, for scientists

6,900
Open access books available

186,000
International authors and editors

200M
Downloads

Our authors are among the

154
Countries delivered to

TOP 1%
most cited scientists

12.2%
Contributors from top 500 universities

CLARIVATE ANALYTICS
BOOK CITATION INDEX
INDEXED

WEB OF SCIENCE™

Selection of our books indexed in the Book Citation Index
in Web of Science™ Core Collection (BKCI)

Interested in publishing with us?
Contact book.department@intechopen.com

ultraMEDIS – Ultra-Wideband Sensing in Medicine

Ingrid Hilger, Katja Dahlke, Gabriella Rimkus, Christiane Geyer, Frank Seifert, Olaf Kosch, Florian Thiel, Matthias Hein, Francesco Scotto di Clemente, Ulrich Schwarz, Marko Helbig and Jürgen Sachs

Additional information is available at the end of the chapter

1. Introduction

The exploitation of electromagnetic interaction with matter specifically with organic tissues is a powerful method to extract information about the state of biological objects in a fast, continuous and non-destructive (i.e. painless) way. These interactions are mainly based on two groups of phenomena.

One proceeds on an atomic and molecular level, which is typically described by the macroscopic quantities permittivity ε, permeability μ and conductivity σ. The physical reasons of possible interactions may be quite manifold. Here, in connection with ultra-wideband sounding, we restrict ourselves to pure electric interactions which affect the permittivity and conductivity via the motion of free charge carriers (free electrons and ions), the Maxwell-Wagner polarization (also Maxwell-Wagner-Sillars polarization) at boundaries, reordering of dipolar molecules or oscillations on an atomic or nuclear level. We assume that all involved substances have the permeability of vacuum $\mu = \mu_0$. An overview of relevant interaction mechanisms for biological tissue is given in [1], and sub-chapter 3 deals with some selected examples. The related effects are scattered over a huge frequency band covering 15…18 decades. In this paper, we limit ourselves to RF and lower microwave frequencies. Water – the key building block of life – shows dipole relaxation within the considered frequency band. Additionally, it has a very high permittivity in comparison with other natural substances. Hence, water will play an important role for UWB-sounding of biological tissue or human and animal subjects. Examples exploiting this fact are discussed in sub-chapter 5 dealing with breast cancer detection or in [2], which refers to lung edema. The frequency bands of our experiments were selected depending on physical requirements (propagation attenuation, relaxation time) and implementation issues of the sensor electrodes (e.g. antennas).

The second group of phenomena refers to macroscopic effects like reflection and refraction of electromagnetic waves. These effects appear at boundaries between substances of different permittivity or conductivity. Thus, a human body illuminated by radio waves will generate new waves which may be registered by an UWB radar sensor. The strongest waves are provoked by the skin reflection due to the large contrast between air and skin. But also inner organs will leave a trace in the scattered waves since firstly, electromagnetic waves within the lower GHz range may penetrate the body, and secondly, the various organs have different permittivity (e.g. due to different water content) leading to reflections at the organ boundaries. These waves can be used to reconstruct high resolution 3D microwave images of external or internal body structures and also to track their shape variation and motion.

It should be emphasized that motion is a strong indicator of vital activities like breathing, heartbeat or walking which can be registered remotely via UWB-radar sensing. This opens up new approaches of medical supervision as exemplified in sub-chapter 4, rescue of people in dangerous situation [3], [4] or supervision of people in need [5], [6].

In what follows, we like to review first some important requirements and technical solutions of high-resolution short-range UWB-sensor aimed at medical applications before we discuss a couple of selected aspects of medical ultra-wideband sensing in greater detail as for example:

a. Impedance (or dielectric) spectroscopy: It is performed to quantify and qualify biological tissue and cells. Here, we have to deal with reflection measurements at an open ended coaxial probe which is in direct contact to the material under test.
b. Organ motion tracking: It is aimed to observe temporal shape variations of the heart and the lung in order to trigger a magnetic resonance (MRI)-tomography. This task requires a remotely operating MIMO-antenna array with an up-date rate which is sufficiently high to follow mechanical motions up to 200 Hz.
c. Remote microwave imaging for surface reconstruction: It may be used as first step in a chain of further UWB-investigations based on remote sensing for inner organ evaluation. In the scope of this work, the data capture was implemented by scanning a torso. Under real conditions, such measurements must be made in real time using a large MIMO array (large in the sense of the number of antennas) in order to avoid artifacts due to body motions during the scan time.
d. Contact-based microwave imaging: In this case, the antennas are placed onto the skin either directly or through a thin dielectric layer in order to emphasize the radiation into the body. Applications are cancer detection or organ supervision and monitoring requiring densely occupied MIMO-arrays based on small radiators.

2. ultraMedis sensing devices

2.1. Requirements

The following overview summarizes some technical key features and requirements to be satisfied by the sensor electronics corresponding to the application types a) – d).

Bandwidth: UWB sensing is an indirect measurement method. As a general rule of thumb, one can state that the quantity respectively the reliability of the gathered information increases with the bandwidth of the sounding signal. It is predetermined and limited by the physical effects involved as well as technical implementation issues. In the case of impedance spectroscopy (application type a)), we applied Network Analyzers or M-sequence devices (see below) whose operational band was spanned from several hundred KHz to some GHz. For UWB-radar experiments, the frequency band was typically limited to 1-13 GHz or to 1-4…8 GHz. The lower cut-off frequency is typically determined by the size of the antennas while wave penetration into the body limits the upper frequencies. Correspondingly, the first frequency band was applied for application type c) which involves only propagation in air. The sensor device was a modified M-Sequence radar [7], [8]. If the sounding field must penetrate the body (applications b) and d)), the upper frequency may be reduced since wave attenuation dominates the other effects. Some details concerning the sensor structure are summarized in the next sub-chapter.

Field exposition: The strength of field exposition appearing in connection with UWB-sensing is usually harmless for biological tissue. Nevertheless, one should distinguish between an average charge and a short impact. A certain average charge of the test objects is required in order to achieve a given quality (in terms of signal-to-noise ratio) of the captured signals. The strength of the maximum impact is related to the type of sounding signals applied by the sensor. Sine waves and M-sequences cause maximum impacts of about the same strength as their average exposition is. In contrast, pulse systems lead to high-peak impacts even if their average charge keeps the same value as for sine waves or M-sequences. Hence, some attention should be paid to the selection of the sensor principle if applicators in direct contact with tissue and short electrode distances are involved (applications of type a) and d)) since this may lead to high field strengths within the test objects causing non-linear effects or even local damages.

Time stability: Here, the term 'time stability' refers to a summary of several facets of sensor performance like precision of equidistant sampling (i.e. linearity of time axis), long-term stability (drift), and short-term stability (jitter). These aspects pertain to all applications. They strongly affect the quality of the captured signals and, hence, the achievable results of the signal processing. In detail, the following items are concerned:

- the quality of time-frequency conversions via FFT, which is an important tool for signal processing
- the quality and durability of sensor calibration (3- or 8-term calibration),
- the limits of super-resolution techniques and the quality of background removal,
- the capability to detect weak targets in the neighborhood of strong ones, and
- the micro-Doppler sensitivity with respect to weak target detection and slow motions tracking.

Some additional aspects of this topic are summarized in Chapter 14. A thorough discussion of related problems and their linkage to the sensor principles is given in [9].

Measurement rate, channel number, data handling: Except for impedance spectroscopy, the applications mentioned above require MIMO-sensor arrays which have to run at a reasonable update rate. On the one hand, this assumes cascadable sensors in order to build multi-channel systems, and on the other it poses some challenges for the data handling resulting from the large number of measurement channels and the high measurement rate. Chapter 14 (section 2.1) adverts to some measures which avoid redundant and inefficient data. Irrespective of these measures, the data throughput will be still quite high so that standard PCs and interfaces quickly reach their capacity limits.

Radiators: The radiators represent the interface between sensor electronics and test object for applications b) – d). They have to convert guided signals into free waves and vice versa. As they are linear and time-invariant devices, they may be operated with any type of signals. Certainly, their major features are the bandwidth and the beam width which should be as large as possible if they are applied for UWB imaging. However, these characteristics describe their performance only insufficiently particularly for UWB short-range applications. Ideal UWB antennas for our purposes should provide a short and angular independent impulse response (time shape and wave front), they should convert the incoming signal completely into a free wave, and the incident fields should be converted into voltage signals avoiding any re-radiation or scattering by the antenna. These conditions are contradictory and cannot be met by a physically realizable antenna.

A short impulse response is needed for high range and image resolution as well as the ability to recover weak targets closely behind surfaces. Otherwise, we risk the loss of the target since a slowly decaying surface reflex distorts the target response. If that signal is too abundant, even sophisticated background removal strategies will not be able to dig it out.

The angular independent impulse response is important for the imaging algorithm. For every image pixel or voxel, it has to coherently integrate signals which are captured from different positions. In order to ensure the coherence of this integration, the propagation time to the considered pixel (voxel) must exactly be known. This involves the knowledge of the propagation speed as well as the knowledge of the deviation from a spherical wave front created by the antennas. In order to achieve a simple and manageable imaging algorithms, the involved antennas should avoid such distortions, hence they should be (electrically) small [9].

However, this contradicts the physical conditions for an efficient conversion between guided signals and freely propagating waves (see Bode-Fano limit and Chu-Wheeler limit [10]). Additionally, efficient antennas backscatter (re-radiate) half of the incident power in the ideal case. For targets in close proximity of the antennas, this leads to multiple reflections which are hardly to remove by signal processing. As we saw for the impulse behavior, the inefficient antennas behave again best regarding their re-radiations (structural antenna reflections are omitted here for shortness). Hence, one has to find a reasonable compromise between efficiency and impulse as well as scattering performance. Antenna efficiency is an important issue in connection with noise suppression and high path losses. For imaging at very close distances, noise induced measurement errors are falling below

the strength of clutter and systematic deviations. Here, efficiency should take a back seat in antenna design in favor of a clear impulse response and low self-reflections. The sensitivity of the sensor electronics should compensate for the efficiency degradation of the antennas.

Furthermore, radiator related items concern array aspects such as the geometric shape of the array, radiator density (depending on antenna size and acceptable cross talk) and distribution within the array as well as polarimetric issues.

In the context of this chapter, we distinguish two types of antenna modes. For the first one, the antenna radiates in air, whereas the other mode refers to interfacial antennas which are in contact with the test object. In both cases, due to the short target distance, we have to deal with spherical waves and their specific reflection and refraction behavior which are accompanied by wave front deformations as well as the generation of evanescent and head waves [9].

Device miniaturization: The application of unusual radiators and the operation of dense MIMO-arrays require new sensor concepts avoiding long RF-cables (which have to be matched at both sides) as well as large and heavy measurement devices as network analyzers. Future MIMO-array implementations for medical microwave imaging should have jointly integrated radiator and sensor electronics in order to permit the operation of mismatched antennas, to increase the stability of the system, to reduce its susceptibility to environmental conditions (e.g. temperature variation or strong magnetic fields) and to simplify its handling. The project HaLos (Chapter 14) was addressing related questions of sensor integration.

2.2. ultraMEDIS sensor electronics

In view of the previous discussion, we mostly abstain from the use of network analyzers since they will not meet the requirements of future developments of the sensing technology even if they best fulfill the demands with respect to sensitivity, bandwidth and reliability of measurement data. A new sensor concept with comparable performance but higher measurement speed, better MIMO capability and integration friendly device layout exploits ultra-wideband pseudo-noise sequences (namely M-sequences) for the target stimulation instead of the sine waves of a network analyzer. This measurement approach was favored for our investigations. Device concepts applying sub-nanosecond pulses were rejected due to their inherent weakness concerning noise and jitter robustness. The interested reader is referred to Chapter 14 and [9] for further discussions of the pros and cons of various sensor principles.

The block schematics of the M-sequence prototype devices applied by ultraMEDIS are depicted in Figs. 4 and 6 in Chapter 14. The integrated RF key components were provided by the project HaloS while the implementation of prototype devices was performed by MEODAT GmbH and later on by ILMSENS. A special issue of an M-sequence device provides 12 GHz bandwidth. Its implementation is based on [8].
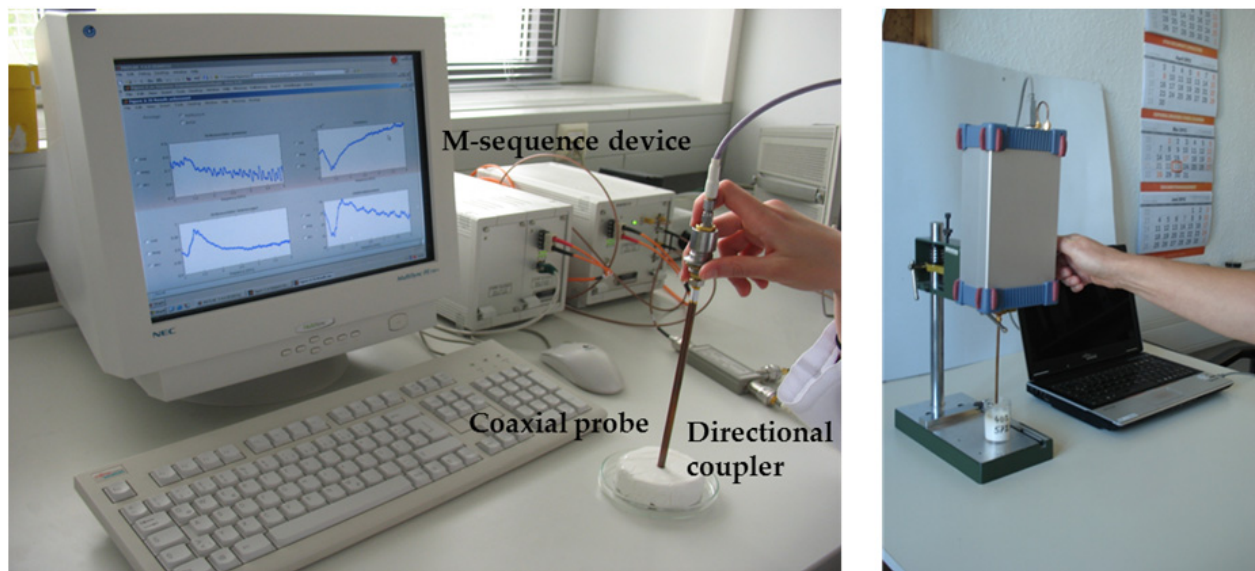
Figure 1. M-sequence based impedance spectroscopy (bandwidth 17 MHz – 4 GHz; 9th order M-sequence). Left: Device implementation with external coupler. Right: M-sequence device with internal coupler and rigid probe connection to improve measurement reliability.

Figure 4 of Chapter 14 (HaLoS-project) relates to the basic structure which can be found in all device modifications. Such device configurations were applied in an early project state for microwave imaging and organ motion tracking experiments. Involving a directional coupler, it is further used for impedance spectroscopy as exemplified in Fig. 1. Multi-channel systems and MIMO-arrays are based on the device philosophy as illustrated in Fig. 6 of Chapter 14. Implemented examples are depicted in Fig. 2 to Fig. 4.

Figure 2. M-sequence two-port network analyzer (operational band 40 MHz – 8 GHz, 9th order M-sequence, USB2 interface). It can be extended by an RF-switch matrix for MIMO-radar imaging.
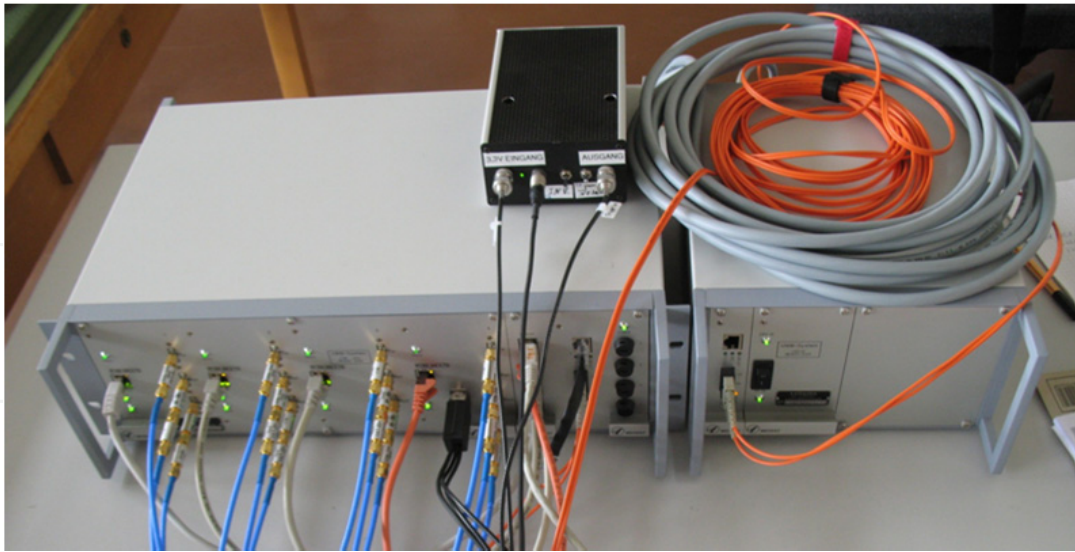
Figure 3. 4Tx-8 Rx MIMO device for organ motion tracking in MRI tomographs. (operational band 17 MHz – 4.5 GHz; 9th order M-sequence; maximum up data rate 530.4 Hz, Ethernet data link, data acquisition on Linux PC)

Figure 4. 8 Tx-16 Rx MIMO radar for microwave breast imaging (operational band 20 MHz – 6 GHz; 9th order M-sequence, USB2 interface). M-sequence units (as shown in Fig. 6 of Chapter 14) and RF-front ends are separated to get more flexibility for experimental purposes.

2.3. Antennas and sensor elements

2.3.1. Introduction

The exploitation of UWB microwave technologies for biomedical diagnostics requires the development of antennas and sensors tailored to this application. The integration of the antennas as a part of a complex system leads to serious compatibility and functionality constraints, which must be properly addressed for high system performance. Within ultraMEDIS, two goals were pursued: Firstly, the detection of early stage breast cancer and secondly, the development of a magnetic resonance imaging (MRI) compatible navigator

system (Section 4). These two goals provide different challenges in terms of antenna design, implementation, and experimental evaluation, both with respect to mechanical and electrical constraints [10]. As both applications involve different approaches, they will be treated separately.

2.3.2. Dielectrically scaled antennas

For the process of detecting early stage breast cancer by means of microwave imaging (Section 5), the antenna size, the effective radiation of electromagnetic energy into the body, and the operational bandwidth turn out to be the main constraints regarding the design of the antenna.

The miniaturization of the antenna is of main concern to meet the requirements of the devised imaging technique (Section 5) of placing an array of many antennas surrounding the target under investigation (i.e. the human breast), considering also the small anatomic dimensions on the scale of the wavelengths of operation. In general, electrically small antennas are mismatched or narrowband [10], [11]. One possibility to overcome these obstacles is to use the antenna in *contact mode*, i.e., placing the antennas in contact with the target under investigation (e.g., the human body). With this *modus operandi* the antenna will radiate into a dielectric material (the human body), and it can be geometrically scaled by a factor of about $\sqrt{\varepsilon}$, where ε represents the dielectric permittivity of the target, without changing its electrical dimensions and, therefore, its radiative properties [12].

The *contact mode* presents advantages also with respect to the constraint of the effective radiation of electromagnetic energy into the body. In fact, it will not suffer from reflections occurring at the air-skin interface, due to the dielectric mismatch between the two grossly different media. This will also simplify the imaging processing since it prevents the need of surface reconstruction [10], [12]. Though, for practical and hygienic reasons, it is less convenient to put the array of antennas in direct contact with the patient's skin. However, the addition of a further layer, e.g. a disposable thin dielectric film, could spoil the effective radiation into the body[1]. Electromagnetic simulations (confirmed by measurements, Section 5.4) have shown that even the addition of a thin layer (~ 0.5 mm) can reduce the radiated power to less than half compared to the direct contact case. The implementation of a matching layer (with similar permittivity to human body tissues) can cure this effect (Fig. 5).

Eventually, particular attention has to be paid to the operational bandwidth of the antenna, especially to the lower cut-off frequency, which limits the penetration depth into the target. Based on a specific 14-layer model mimicking a trans-thoratic slice from the visual human data set, we have computed the penetration of electromagnetic waves into a human body, as shown in Fig. 6 [13], [14] and [15]. A strong increase of the signal attenuation with increasing frequency is clearly seen. Therefore, the lower cut-off frequency has to be set between 1 GHz and 2 GHz.

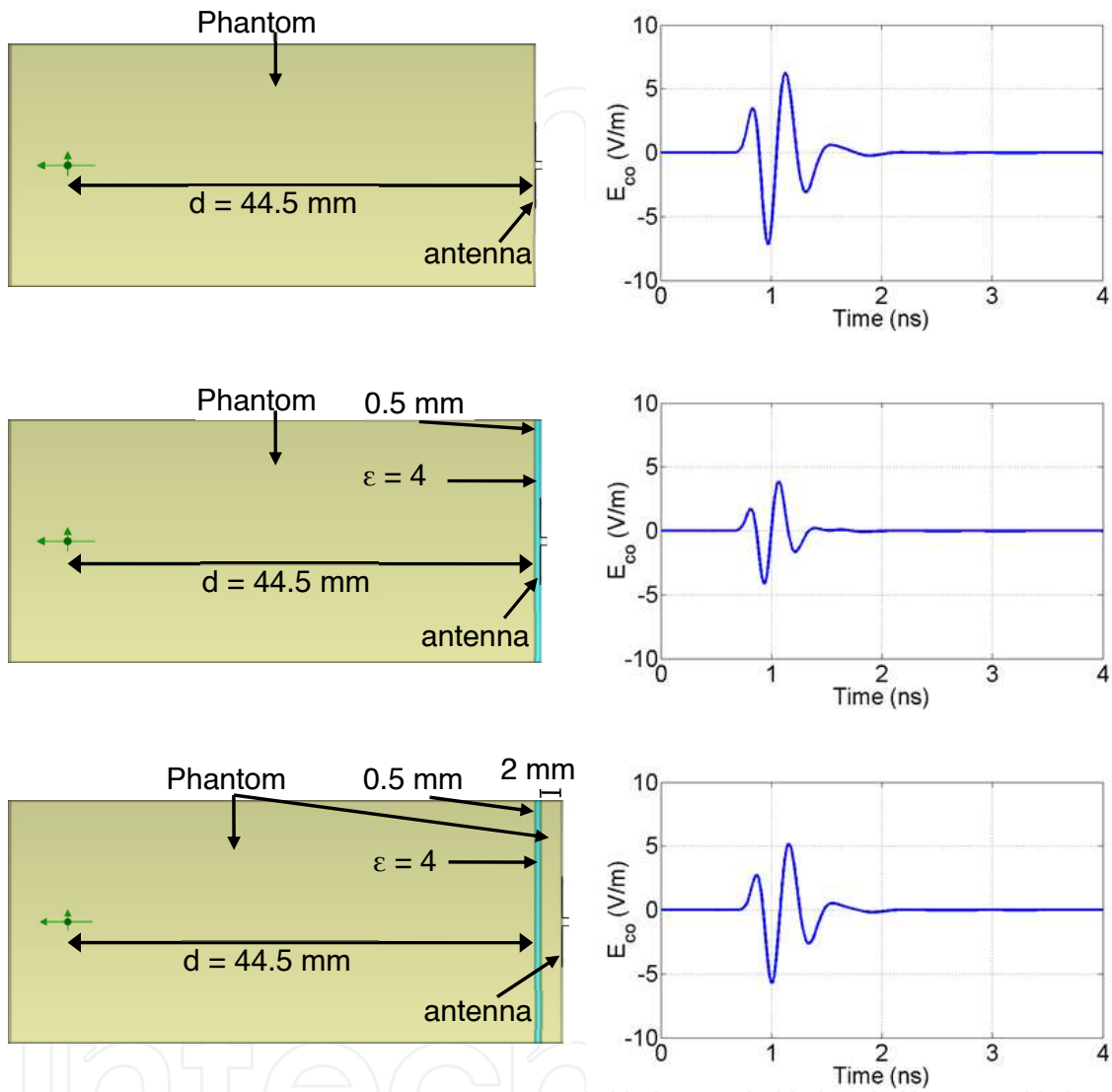[1] The relevance of this phenomenon depends also on the antenna type used

Figure 5. Simulated scenarios to investigate the effective radiation of electromagnetic energy into the body (on the left). The antenna used is a bow-tie excited by a Gaussian pulse of a duration of around 80 ps FWHM. The *Phantom* material is a homogenous dispersive material simulating the dielectric behavior of the human body tissues. The results (on the right) represent the time-dependent co-polar component of the electric field evaluated at a distance of 44.5 mm from the phantom interface (the green spot in the figure). The examined cases are, from top to bottom: the antenna in direct contact with the phantom; with the implementation of a thin dielectric layer; with the implementation of a matching layer plus a thin dielectric layer, respectively.
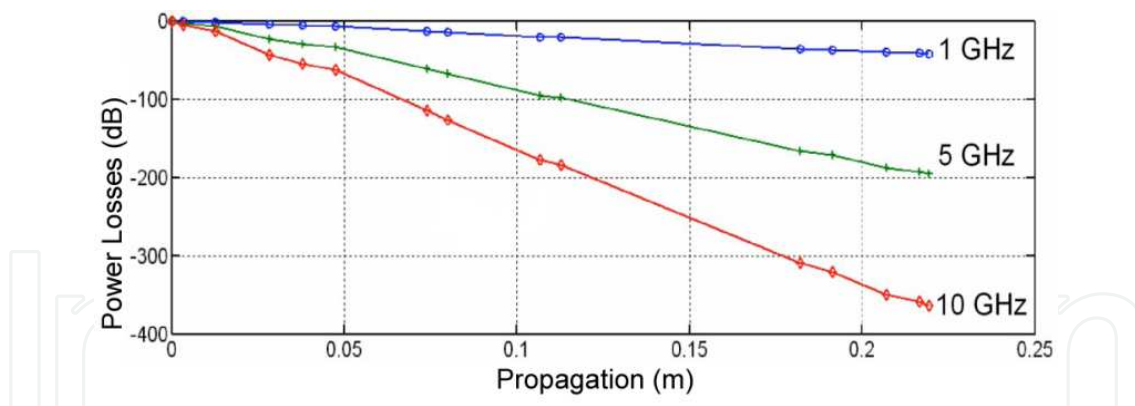
Figure 6. Penetration depth into a 14-layer model computed for different frequencies (see legend) [13].

The dielectric scaling of traveling-wave antennas, like tapered slot antennas and horn antennas, has to consider all three factors - the phase constant, the wave impedance, and the feeding structure [16]. Accordingly, extended iterative full-wave simulations were performed. The key parameters of the wideband radiation properties of double-ridged horn (DRH) antennas turned out to be the curvature of the ridges, the spacing between them, and the geometry of the pyramidal casing itself. Traveling-wave antennas have the benefit that the dielectric medium used to scale the antenna will serve as an embedded *matching medium*.

Our initial design was based on the immersion of dielectric liquids into the sinkhole of a dielectrically scaled DRH antenna [15]. The antenna could successfully be manufactured, using acetone as dielectric medium, with a scaling factor of about 4, but it was still insufficient to obtain a sufficiently compact antenna. The straight-forward approach to solve this problem was to replace the acetone by alternative high-permittivity dielectric materials, like a solid sintered ceramic. The ceramic powder is the commercial product LF-085 manufactured by MRA Laboratories based on neodymium titanate [17].

As the complex permittivity ε of the ceramic body of the antenna plays an important role not only in terms of antenna design but also in terms of *matching medium*, we performed measurements to access the complex permittivity following two different strategies: employing a split-post dielectric resonator (SPDR, [18]) and a dielectric resonator (DR) technique [19][20]. Both techniques are resonant methods and, hence, limit the experimental studies to a small set of discrete frequencies, because specific sample geometries are required for each measured frequency. The results showed that the sintered ceramic presents low frequency dispersion with a mean value of the real part of the permittivity $\varepsilon' \cong 72$ [21], offering the potential for a scale factor of around 8.

The exploitation of the full potential of dielectric scaling leads to an aperture size of only 11 mm × 16 mm, but also to the reduction of the input impedance by the same scaling factor as by which the geometrical dimensions are scaled, resulting in a low value below 10 Ω. This value implies a large mismatch in terms of standard electronic equipment, which is usually designed for a characteristic impedance of 50 Ω. In order to maintain the compatibility with standard electronic equipment, the antenna retains an aperture size of 24 mm × 24 mm, and a frequency bandwidth ranging from 1.5 to 5.5 GHz (Fig. 7).
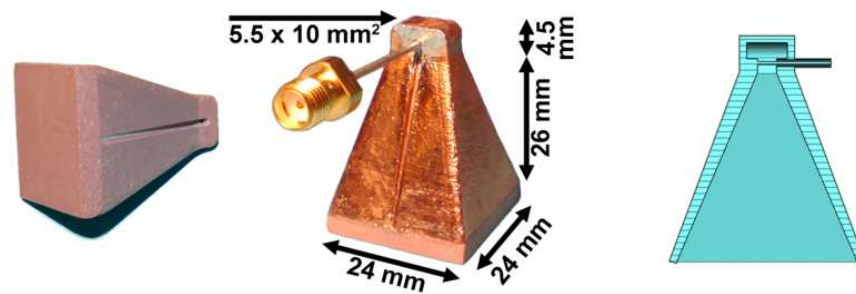
Figure 7. The left-hand panel shows the completely processed ceramic body of the antenna. The center panel depicts the final antenna including metallization, feed line and dimensions. The right-hand panel displays the profile of the ridges.

In order to properly manufacture the antenna and obtain good yield (of around 75 %) and reproducibility, specific manufacturing steps have to be devised, as indicated in the right image of Fig. 8 [22]. First, the white-colored ceramic powder (Fig. 8a) is pressed into the specific pyramidal shape; a cubic base accommodates the asymmetric feed (Fig. 8b). The dimensions of the raw body are slightly enlarged in order to respect the shrinkage upon sintering. The sintered body is complemented by grooves, which form the ridges (Fig. 8c), and is subsequently galvanically metalized with copper or gold (Fig. 8d). Due to the high permittivity of the ceramic body and a feed impedance of 50 Ω, the ridges are nearly linear in geometry, in contrast to the markedly curved shapes found in antennas for operation in air [12][15]. The feed is provided by a coaxial cable whose center conductor is fed through a small bore to the narrow end (diameter about 1.2 mm) of the ridged waveguide. A plastic housing and epoxy fixture provide a compact and mechanically rigid construction, to protect the ceramic body and the coaxial feed against torque and damages due to improper handling. It also provides a mechanical fixture to mount the antennas in an array of complex geometry (Fig. 8e). Further details of the manufacturing processes are given in [23].
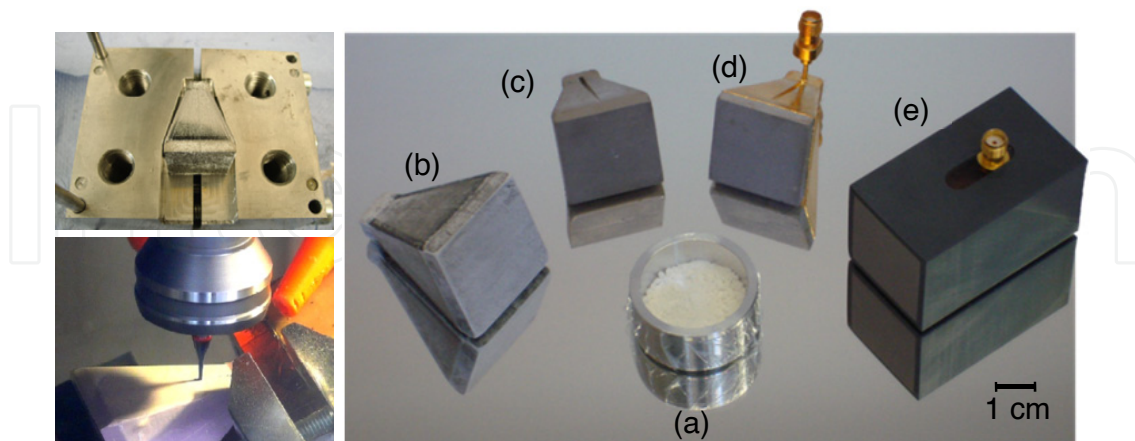

Figure 8. The left-top picture shows a dry pressed green body of the antenna with some lubricant on it inside the dismantled mold. The left-bottom picture depicts the milling process to work in the ridges into the sintered ceramic body. The right picture illustrates the manufacturing steps for the sintered horn antenna: powder raw material (a), pressed raw (b), sintered (c), metallized (d), and fully packaged versions (e).

A further issue of dielectrically scaled antennas is related to their measurement and characterization. As common measurement techniques and equipment cannot be applied, we followed three different strategies: measurements made in the frequency domain, measurements made in the time domain, and basic tests with volunteers.

In order to provide dielectrically matched surrounding conditions for the antenna body, the antennas were tested in de-ionized water. The results were then compared with data obtained in a more realistic environment, i.e. with the antenna put into contact with phantoms mimicking human tissues. The phantoms consisted of oil, water and some additives [24]. The dielectric permittivity ε' and the loss tangent $\varepsilon''/\varepsilon'$ of the phantoms can be controlled by changing the percentage of oil [24], [25] (Section 5.2).

The frequency behavior of the reflection coefficient is shown in Fig. 9. It can be observed that while the reflection coefficient for the test against the phantom (with 40% oil, Section 5.2) approaches levels around –8 dB, the antenna is even better matched in water, leading to a further decrease of the reflection coefficient by 4 dB in the frequency range of interest. The compromise between input matching to a certain medium and the geometrical dimensions of the antenna denotes the key trade-off exploited for our design. In order to study the reflection occurring at the aperture plane, which is influenced by the permittivity matching between the dielectric medium composing the antenna body and the human skin, we performed time domain reflectometry (TDR) measurements by having the antenna radiate into different media [22].
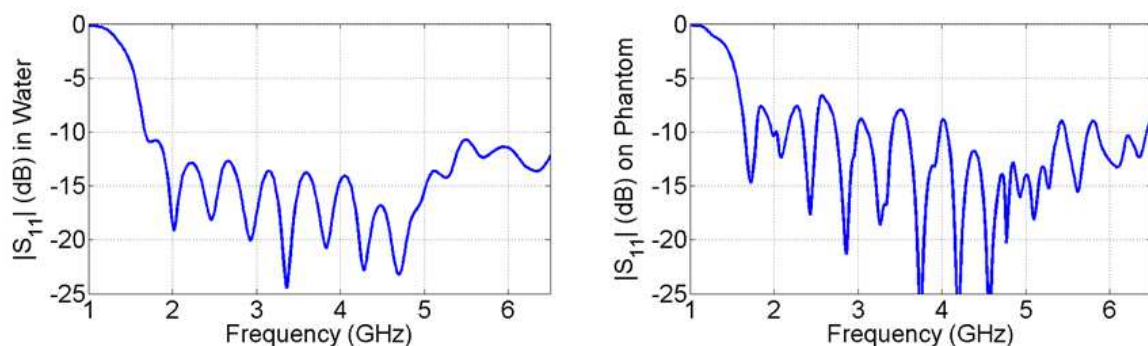

Figure 9. Reflection coefficient measured in water (left) and on a skin mimicking phantom (right).

The results for water and skin (in-vivo) are shown in Fig. 10. The amplitude of the reflected signal with the antenna operating in water is significantly smaller than the one with the antenna operating on skin. This result indicates, in agreement with the frequency domain measurements, that the antenna is better matched to water than to skin. We note from Fig. 10 that the reflection occurring at the aperture due to impedance mismatch results in a signal with a longer decaying time. The larger the impedance mismatch is the longer the decaying time is. This feature is due to the fact that part of the reflected energy does not leave the antenna through the well-matched feed towards the signal source but remains within the antenna body.
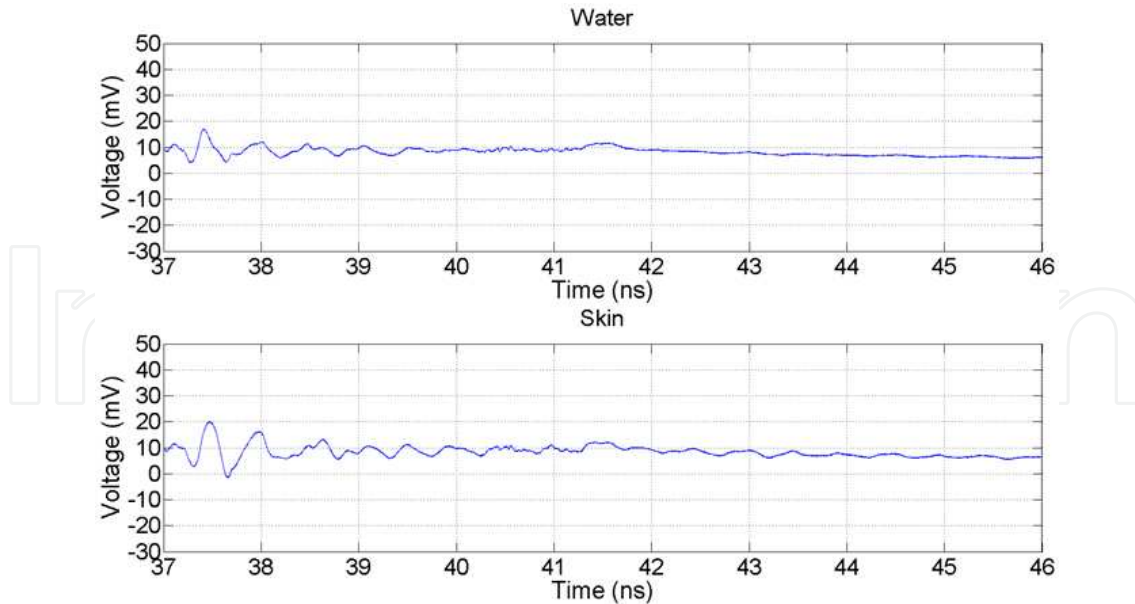
Figure 10. Time domain reflections caused by the aperture plane due to dielectric mismatch between the antenna and water and skin, respectively (top and bottom).

The measurement of the radiating behavior is more complicated. To evaluate standard antenna parameters (e.g. gain, radiation pattern, etc.), the antennas should be placed in the Fraunhofer region. However, due to the high dielectric losses of water, the antenna could be placed at a maximum distance of 10 cm, which is not sufficient to meet the Fraunhofer region (starting from around 35 cm), but still is large enough to let the antennas operate in the Fresnel region. Near-field measurements are of main concern since the antennas are designed to be used in contact mode for biomedical imaging applications. The results show that the antennas present a flat frequency response (measured along the boresight direction), after the compensation of the frequency dispersion of the water (left diagram in Fig. 11), and 3 dB beam widths of nearly 20° for the E-Plane, and nearly 28° for the H-Plane (right diagram in Fig. 11).
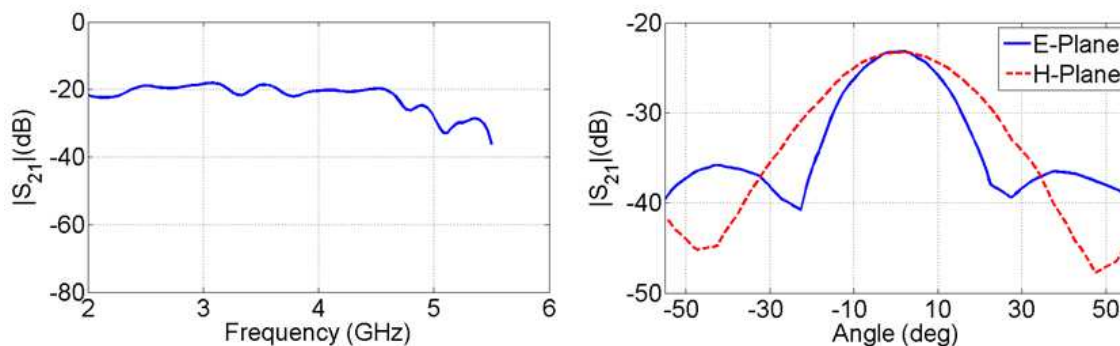

Figure 11. Transmission behavior between two identical antennas operating in de-ionized water at a distance of 10 cm. The frequency response, compensated for water frequency dispersion is shown in the left diagram, while the near-field pattern is represented on the right. The blue and red curves illustrate a cut along the E-Plane and the H-Plane, respectively.

Eventually, in order to demonstrate the functionality of the ceramic antennas under realistic conditions, we have performed preliminary transmission measurements through a breast of a female volunteer, and the monitoring of the heartbeat, as illustrated in Figs. 12 and 13. The dynamic range of the achievable signal can be determined from Fig. 12 in comparison with the ideal transmission through a 4 cm path inside distilled water by a face-to-face arrangement of the antennas. The monitoring of the heartbeat was performed on a 35 years old healthy male volunteer. During measurement, the volunteer was sitting still and was holding breath in the state of maximal breathing in. The measurement was performed with an M-sequence radar in a bi-static configuration [Section 2.2]. Figure 13 shows the heartbeat signals as monitored. Upon Fourier transformation, we extracted a beat rate of nearly 75 beats per minute, which is considered normal for an adult. The results display very clearly the characteristic feature of heartbeat, thus manifesting a favorable dynamic range. This opens up promising applications for realistic monitoring and imaging tasks. Further details of these tests can be found in [26] and [22].

The full dielectric scaling, as previously stated, offers the potential for a further size reduction of the antenna. Accordingly, we continued our research and succeeded in developing a ceramic DRH antenna with an aperture of only 16 mm × 11 mm and a lower cut-off frequency around 1.5 GHz. Due to the input impedance of the antenna below 10 Ω, active receive and transmit versions are under development in the framework of HALOS (Chapter 14), employing an UWB low-noise subtraction circuitry and power amplification [27]. The manufacture of the tiny antenna followed similar production steps as for the previous version. It proved quite challenging because of the reduced size, requiring additional specific production steps and iterative testing procedures [28].
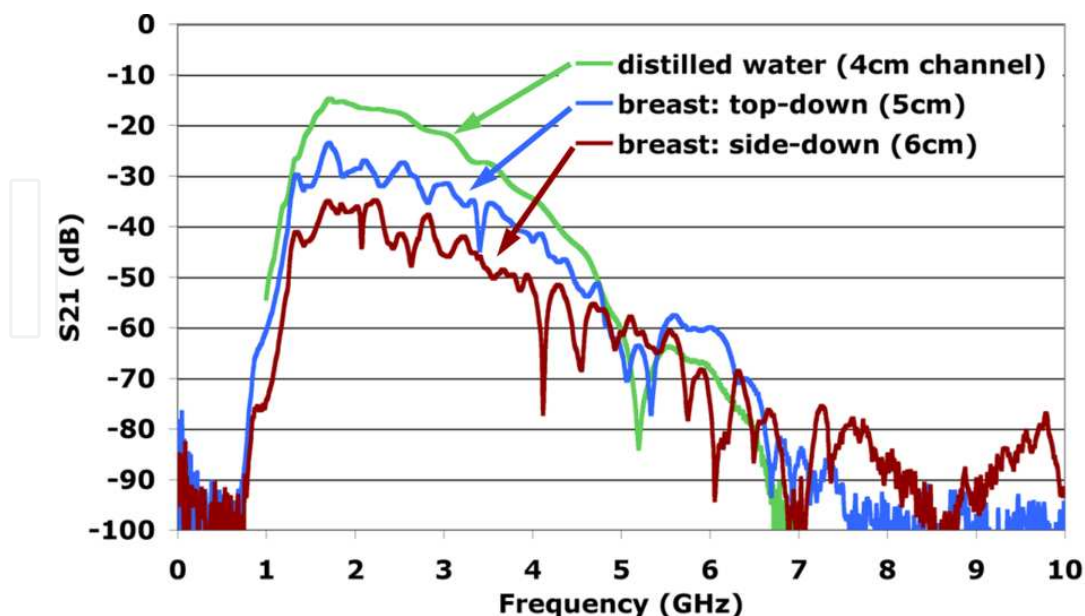

Figure 12. Transmission measurements through a female breast performed with the ceramic double-ridged horn antennas in comparison with a reference measurement of 4 cm distilled water (upper curve).
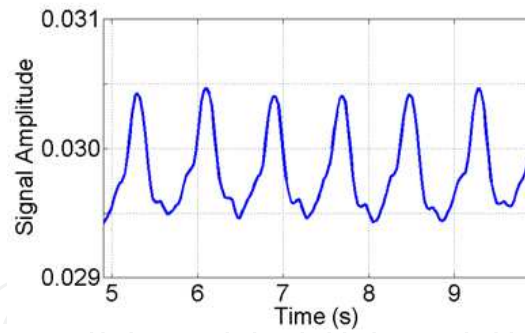
Figure 13. Monitored heartbeat signal of a 35 years old healthy male volunteer. Upon Fourier transformation, we extracted a beat rate of nearly 75 beats per minute.

2.3.3. MRI compatible antennas

Magnetic resonance imaging (MRI) systems are among the most sensitive diagnostic methods in medicine for the visualization of soft tissue [10]. At present, more than ten million MRI examinations of patients are performed per year worldwide. Given such a progressive development, further improvements of this diagnostic technique are under way. However, MRI systems are not *per se* capable of creating focused images of moving objects like the human heart or the thorax of the patient while breathing. Instead, additional techniques like breath holding, ECG triggering, or MR navigation methods are required. Such techniques either cause some inconvenience for the patient, or they are even not applicable for upcoming generations of MR scanners. A novel approach which overcomes these obstacles is the use of low-power multi-static UWB radar as a contactless navigator technology for MR tomography [29], [30]. To devise such navigators, the design of antennas compatible with MRI systems, i.e. antennas which do not interact neither electrically nor mechanically with the operation of the MR scan, is needed. The strategy to follow when designing an MRI compatible antenna is the minimization of mutual interaction between the metallized antennas and the strong static and gradient magnetic fields. Several experiments with conventional wideband antennas showed strong mechanical interactions, pointing out the need for special antenna designs [31]. The operational conditions inside an MR scanner are determined by three different types of fields. First, a static magnetic field B_{stat} = 1.5 to 7 T provides a reference orientation of the nuclear spins of the regions under inspection. Furthermore, gradient magnetic fields with a slope of dB_{grad}/dt = 50 T/s at the rising edge are switched during diagnostic measurements to allow for spatial (depth) information of the acquired molecular information. Finally, the nuclear spins are set into precession by a strong (KW range) RF signal at 42.58 MHz/T. The gradient fields induce eddy currents in the metallized sections of the antenna which, in turn, interact with the static magnetic field by exerting a mechanical torque on the antenna structure. The torque can reach peak values of the order of 0.045 Nm for a contiguous metallized area of 20 mm × 30 mm. This value is high enough to result in mechanical amplitudes of several millimeters, deforming or moving the antenna structure, especially in the case of mechanical resonances. Furthermore, the magnetic fields of the eddy currents can lead to artifacts of the MR-image. These interactions inhibit the beneficial application of UWB navigation for magnetic resonance imaging and,

therefore, must be avoided. We used a 3-T MR scanner with the resulting RF frequency of 127.8 MHz, which is ten times smaller than the lower cut-off frequency of the UWB antennas employed. As the frequency response of a typical antenna corresponds to a high-pass filter of first order, the stop-band attenuation amounts to 20 dB per decade, indicating the risk of collecting RF power even in the presence of path-loss and shadowing.

The minimization of contiguous metallized area and, hence, eddy currents, is therefore the main issue to be addressed by the antenna design. Additional constraints arise from the intended applications in biomedical diagnostics: weakly frequency-dependent radiation patterns over the entire operational bandwidth, good decoupling between neighboring antennas, and a lower cut-off frequency around 1 GHz. The DRH antenna was identified to be a suitable UWB antenna type to accomplish these requirements. Due to the functional principle of DRH antennas, the minimization of contiguous metallized areas and the realization of a weakly frequency-dependent radiation pattern are in conflict with each other. Horn antennas are typically made entirely out of metallic parts of high electrical conductivity σ, thus suffering from the induction of eddy currents under MR-scanner conditions. Therefore, the major challenge was to modify the double-ridged horn antenna to achieve MR-compatibility, without compromising the favorable radiation properties.

Inspired by commercial counterparts of DRH antennas, we removed the H-plane sidewalls of the pyramidal horn, leaving just a thin wire in the plane of the aperture, as illustrated by the left picture in Fig. 14. As a result, the lower cut-off frequency could be reduced from 2.6 GHz to 1.5 GHz for otherwise unchanged dimensions and operation in air. The comparison with a conventional double-ridged horn antenna with a similar bandwidth revealed that this improvement was achieved at the expense of increased beam width, side-lobes and backward radiation, predominantly at frequencies below 3 GHz, due to the modified aperture distribution and diffraction at the edges of the open construction. The increased beam width led to a slightly increased crosstalk [32]. It can easily be compensated for by re-orienting the antennas relative to each other. While the crosstalk for conventional DRH antennas becomes small for an H-plane alignment, the MR-compatible versions have to be aligned along the E-plane due to the removed H-plane sidewalls and, thus, reduced shielding.

The thickness of the metallization was also reduced in order to exploit the skin effect for a decoupling of the low-frequency eddy current paths. The metal planes were replaced by metallized dielectric boards with a metallization thickness of 12 μm (Fig. 14). This value corresponds to about twice the skin depth at the lowest frequency used. The high-frequency currents determining the radiation of the antenna remain essentially undisturbed while the eddy currents in the KHz range are strongly attenuated by the high sheet resistance. For further optimization of the remaining metallized areas, the distribution of surface currents in the UWB frequency range was inspected by electromagnetic simulations (right image of Fig. 14). Typical results for the normalized surface current are illustrated at 5 GHz (left-most). The surface current is concentrated near the position of the ridge and the edges of the pyramidal frame. According to our expectations, the number of current loops was found to increase with frequency; in contrast, the current distribution across the backward cubical

part of the antenna showed little frequency dependence. Based on these observations, a compromise was sought to reduce the plane metallization with the minimal possible distortion of the broadband current distribution. As a result, the conductor faces of the horn sections were separated into strip lines, straight and elliptically shaped, separated by 1 mm, and oriented parallel to the most common current paths, with plain connections at the face edges only. The central part of the right image of Fig. 14 illustrates the resulting geometric arrangement of the slots, while the normalized surface current of the modified antenna at 5 GHz is shown in the right-most part. The main features of the current distribution could be sustained qualitatively both on the pyramidal faces and the backward cubical part of the antenna. Differences occurred mainly for the currents oriented perpendicular to the slots. It is this minor change in current distribution which causes the modified radiation properties discussed above. The ridges themselves required special attention. A grid of holes was eventually identified as the proper solution to reduce the metallization area of the ridges without disturbing the high-frequency current distribution too much. In order to reduce the maximal loop size for low-frequency currents, the outer contour of the horn section was cut and shortened by standard surface-mounted device capacitors.
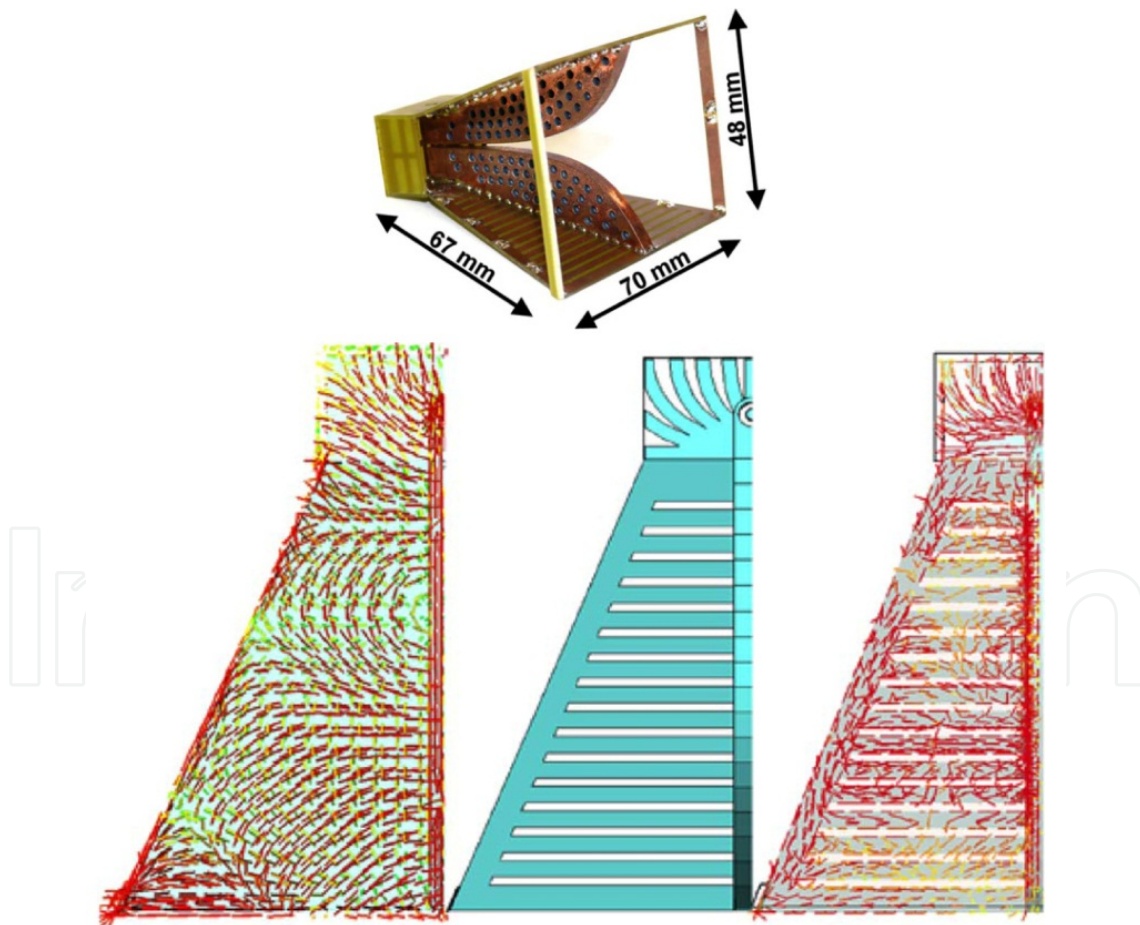

Figure 14. MR-compatible double-ridged horn antenna for a lower cut-off frequency of 1.5 GHz (top). The lower image shows the simulated, normalized current distribution of an unmodified DRH antenna at 5 GHz (left-hand part), the layout of the resulting MR-compatible DRH antenna (center part), and the current distribution of the modified DRH antenna at 5 GHz (right-hand part).
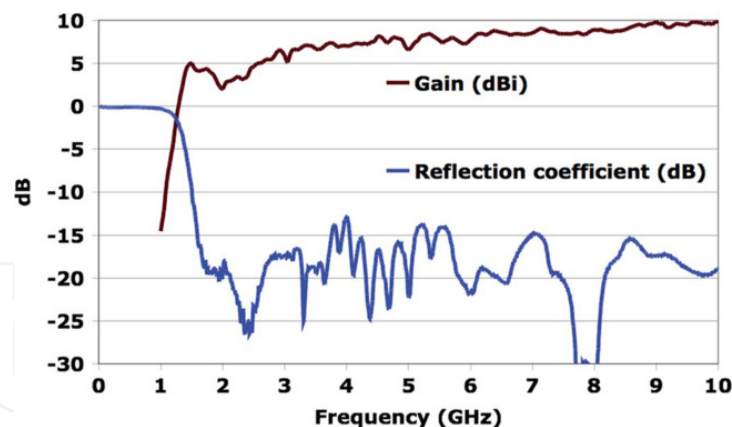
Figure 15. Measured reflection coefficient of the MR-compatible double-ridged horn antenna (lower curve) and the measured antenna gain (upper curve) versus frequency.

Fig. 15 displays measured results for the reflection coefficient and the gain of the modified DRH antenna. A return loss above 10 dB was achieved over the frequency range from 1.5 to 12 GHz. Radiation measurements in an anechoic chamber yielded the radiation patterns illustrated in Fig. 16 for two orthogonal cuts with respect to the plane of the ridges. The half-power beam width, indicated as the black contour line in Fig. 16, was found to vary between 30 and 50 degrees, thus covering a range suitable for the envisaged applications. Except for frequencies around 2 GHz, the main lobe showed little spectral variation. The corresponding frequency variation of the antenna gain is displayed in Fig. 16. These results were found in good agreement with the numerical simulations.
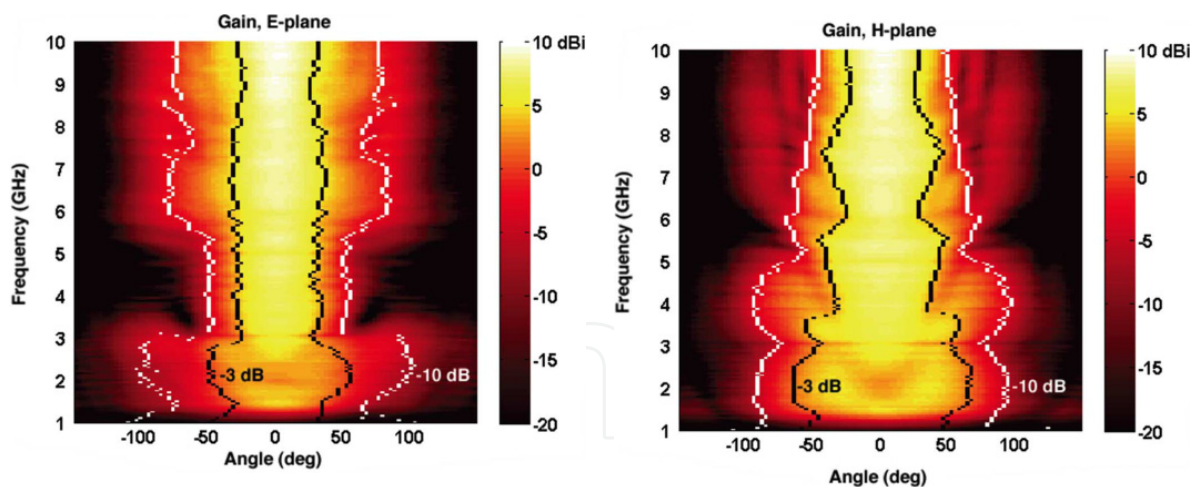

Figure 16. Two-dimensional representation of the measured radiation pattern of the MR-compatible double-ridged horn antenna for the E-plane (left) and the H-plane (right) through the main beam. The scales indicate the antenna gain in dBi. The black and white contour lines illustrate the corresponding beam widths at 3 and 10 dB below the frequency-dependent maximum gain, respectively.

The transient response of the antenna is shown in Fig. 17. Despite the open geometry of the MR-compatible antenna, a low signal distortion could be sustained. The slight angular dependence of the time responses can be attributed to an offset between the phase centers of the antennas and the center of rotation of the antenna positioning system.

The MRI compatible DRH antennas were implemented as part of a UWB MR navigator, by means of which it was possible to take images of the myocardium for the first time without using an ECG as navigator. The quality achieved was comparable with the one achievable with the ECG navigator (see Section 4).
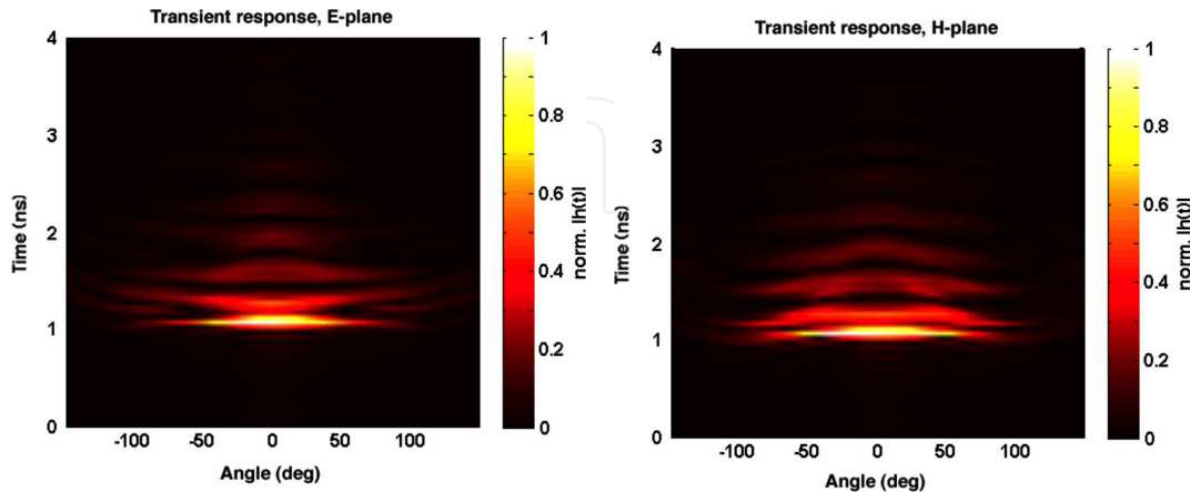

Figure 17. Two-dimensional representation of the measured time domain response of the MR-compatible DRH antenna for the E-plane (left) and the H-plane (right) through the main beam. The scales indicate the normalized impulse response of the antenna.

3. Weak electromagnetic fields and biological tissue

3.1. Impact on living cells

The electrical properties of biological tissues and cell suspensions have been of interest for over a century for many reasons. They determine the pathways of current flow through the body and are very important for the analysis of a wide range of biomedical applications such as functional electrical stimulation and the diagnosis and treatment of various physiological conditions with weak electric currents, radio-frequency hyperthermia, electrocardiography, and body composition. On a more fundamental level, the knowledge of these electrical properties can lead to an understanding of the underlying basic biological processes. Indeed, biological impedance studies have long been an important issue in electrophysiology and biophysics; interestingly, one of the first demonstrations of the existence of the cell membrane was based on dielectric studies on cell suspensions [33].

Biological tissues are a mixture of water, ions, and organic molecules organized in cells, sub-cellular structures, and membranes, and its dielectric properties are highly frequency-dependent in the range from Hz to GHz. The spectrum is characterized by three main dispersion regions referred to as α, β, and γ regions at low, intermediate, and high frequencies [34]. Biological materials can show large dispersions, especially at low frequencies (Fig. 18). Low frequencies are mainly caused by interfacial polarizations at the surfaces between the different materials of which a cell is composed [35]. Reviews of the dielectric properties of cells and the different dispersions are given in the literature [36], [37].
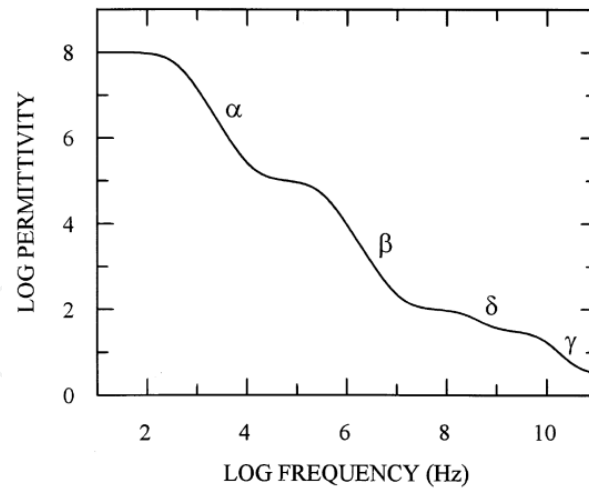
Figure 18. Spectrum of the dielectric properties of cell suspensions and tissues.

The step changes in ε_r are called dispersions and are due to the loss of particular polarization processes as frequency increases. The α-dispersion is due to the flow of ions across cell surfaces, the β-dispersion results from the charge at cell membranes, the δ-dispersion is produced by the rotation of macromolecular side-chains and bound water, and the γ-dispersion is due to the dipolar rotation of small molecules particularly water [35] (figure reproduced with permission from Elsevier).

When exposed to electric fields, living cells behave as tiny capacitors, accumulating charges on the cell surface. The permittivity of living cell suspensions is dependent on the frequency, and falls in a series of the dispersions described above, as frequency increases. The β-dispersion, between 0.1 and 100 MHz, results from the build-up of charges at cell membranes. The difference between permittivity measurements made at two frequencies, on either side of the β-dispersion range, is proportional to the viable biomass concentration. With spherical cells, the permittivity increment is given by equation [38].

$$\Delta\varepsilon = \frac{9\, P\, r\, C_m}{4} \tag{1}$$

As long as there is no change in the cell radius r or the membrane capacitance C_m, the permittivity increment $\Delta\varepsilon$ is proportional to the cell volume fraction P [39].

As a starting point for developing new applications, it is critical to characterize differences in the dielectric properties of the cells, for example human leukocyte subpopulations [40]. Even though, a comparative analysis of the dielectric properties of the cells is necessary, and the UWB radiation on cells itself has to be characterized, too. For this reason, experiments with two different cell lines (tumor cell line BT474 and fibroblasts BJ) were performed. Cell suspensions of these cell lines were disseminated, and the growth rate was determined. Afterwards, the cells were seeded on 96-well plates, cultivated for 24 h and exposed to UWB radiation *via* UWB-M-sequence radar with double-ridged horn antennas of about 10 dBi average gain for 5, 30 or 60 min. As non-treated control, for the same time,

plates were placed in a Faraday cage (to avoid any irradiation). After continued incubation for 24, 48 and 72 h, the vitality of cells was determined by colorimetric identification (MTT assay for measuring the activity of enzymes that reduce MTT [3-(4.5-Dimethylthiazol-2-yl)-2.5-diphenyltetrazolium bromide, yellow tetrazole] to formazan, giving a purple color). The measured vitality of control cells was normalized to 100%, and the vitality of exposed cells was put into relation. The vitality of exposed cells was related to non-exposed cells. Due to biological fluctuations, data between 70% and 120% vitality were assessed as not influenced. As depicted in Fig. 19, none of the determined cells was influenced by ultra-wideband electromagnetic waves.
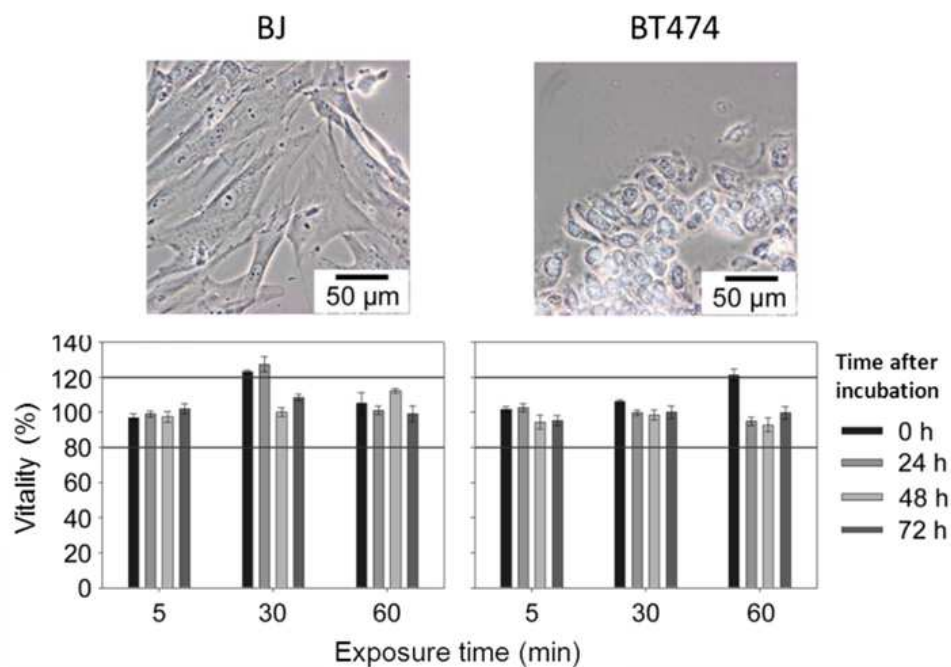

Figure 19. Impact of ultra-wideband electromagnetic waves on the vitality of living cells. The upper part of the figure shows light images of the fibroblast cell line BJ and the cancerous cell line BT474. The lower figure depicts the vitality of the fibroblasts BJ and the cancerous cells BT474 after UWB exposition with 4 mW for 5, 30 or 60 min. The vitality was observed 0, 24, 48 or 72 h after exposure. The depicted vitality of exposed cells is related to non-exposed cells. Due to biological fluctuations, data between 80% and 120% vitality was not considered to be cytotoxic [25].

3.2. Animal tissue

The electrical properties of tissues and cell suspensions are most unusual. They change with frequency in three distinct steps (dispersions as described above) and their dielectric constants reach enormous values at low frequencies. Extensive measurements were carried out over a broad frequency range extending from less than 1 Hz to many GHz. The observed frequency changes of these properties obey causality, i.e., the Kramers-Kronig relationships which relate changes of dielectric constants with conductivity changes. A number of mechanisms were identified which explain the observed data. These mechanisms reflect the various compartments of the biological material. These include membranes and

their properties, biological macromolecules and fluid compartments inside and outside membranes [41]. Special topics include a summary of the significant advances in theories on counter ion polarization effects, dielectric properties of cancer *vs.* normal tissues, properties of low-water-content tissues [42], and macroscopic field-coupling considerations. The dielectric properties of tissues are often summarized as empirical correlations with tissue water contents in other compositional variables. The bulk electrical properties of tissues are needed for many bioengineering applications of electric fields or currents, and they provide insight into the basic mechanisms that govern the interaction of electric fields with tissue [43].

Using devices with our own configurations, the dielectric properties of different porcine and bovine tissues were determined [25]. Different measuring points were defined on the surface of udder, fat, liver, muscle, and kidney of porcine and bovine tissue (homogenous structure) and the permittivity of these points was measured three times (selected tissues in Fig. 20, left panel). Afterwards, the tissue under these measuring points was excised and dried to calculate the water content. Water content and permittivity ε' were related to each other, so we could clearly differentiate between fat, low-water-content tissue, with a low permittivity ($\varepsilon' \approx 8$) and liver, muscle or kidney ($\varepsilon' \approx 40$) as high-water-content tissues. The high-water-content tissues show similar permittivity ε' values whereas fat of porcine and bovine origin can be distinguished (Fig. 20, right panel).
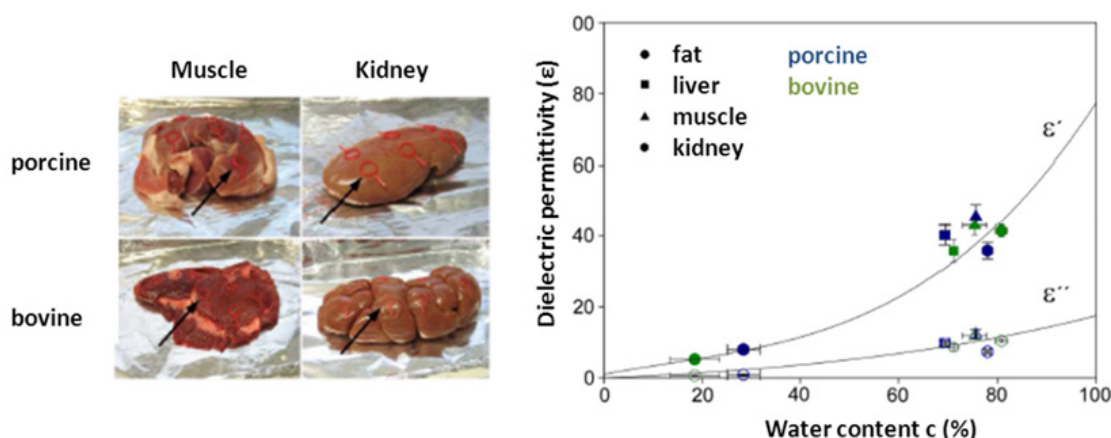

Figure 20. Determination of the dielectric properties of different porcine and bovine tissues at defined measuring points (left panel). Real and imaginary part of permittivity ε' at 2 GHz of porcine and bovine tissue in relation to the water content (right panel). The standard error represents six independent measurements [25].

3.3. Bacterial cell wall identification based on their dielectric properties

The identification of bacterial strains in biological media is a matter of interest in very different fields of modern life. Examples are in food hygiene and food industry, catering and gastronomy [44], [45], in environmental research activities, fermentation processes for the production of medical drugs, such as insulin, antibiotics, and other [46]-[48], and in the diagnosis of infections in clinical and veterinarian applications [49]. Depending on the

respective research and application field, bacterial strains are currently detected by complex methods, for example: polymerase chain reaction (technique to amplify a single or a few copies of a piece of DNA), fluorescent *in situ* hybridization, DNA microarray and Raman-spectroscopy, etc.

Different studies have shed some light into the biomass determination of different microbial suspensions *via* dielectric spectroscopy. Mishima *et al.* investigated growth kinetics of bacterial, yeast and animal cells by dielectric monitoring in the frequency range of 10 kHz - 10 MHz [50]. The determination of bacterial growth by dielectric measurements was also shown by Harris *et al.* [51]. Jonsson *et al.* measured the concentration of bacterial cells *via* indirect methods based on the dielectric determination of ions in the suspension, which are released by killed cells [52]. Benoit *et al.* showed that it is possible to discriminate the hydrophobic or hydrophilic features of bacterial suspensions by determining the dielectric permittivity [53]. Nevertheless, no data are available for discrimination on the basis of bacterial structures *per se*, such as the presence of Gram-positive or Gram-negative bacterial strains in biological samples [54].

Therefore, two different Gram-positive bacterial strains (*Micrococcus luteus* and *Bacillus subtilis*) and two Gram-negative bacterial strains (*Escherichia coli* and *Serratia marcescens*) were cultivated under standard conditions using Standard I media and shaking flasks. Bacterial strains were incubated for 24 h at 37°C in an incubation shaker. To assess whether the Gram-status of bacteria could be determined by dielectric spectroscopy, bacterial suspensions were transferred to 50 ml tubes and centrifuged. The supernatant (liquid above precipitate) was removed, the pellet was washed in 0.9% sodium chloride solution and, finally, the dielectric properties of the bacterial biomass (pellet of 10 ml) were determined. Dielectric spectroscopy of bacterial strains and suspensions was performed using a network analyzer in a frequency range from 30 kHz to 6 GHz (HP 8753D) and a coaxial probe (High temperature probe). The real ε' and imaginary ε'' part of permittivity was determined in a frequency range from 50 MHz to 300 MHz [54].

In the frequency range between 50 and 300 MHz, dielectric spectroscopy revealed higher values of the real part of permittivity ($\varepsilon'_{(+)} \approx 160$ Gram-positive) of the Gram-positive bacterial strains *Micrococcus luteus* and *Bacillus subtilis* compared to the Gram-negative strains *Escherichia coli* and *Serratia marcescens* ($\varepsilon'_{(-)} \approx 100$ Gram-negative). From each strain the same cell count and volume was measured. Particularly at a frequency of 50 MHz (maximum of discrimination), the real part of permittivity ε' of both Gram-positive strains was about 60 units higher than of the Gram-negative strains (Fig. 21)

The clear discrimination between the Gram-positive strains *Micrococcus luteus* and *Bacillus subtilis* as well as the Gram-negative strains *Escherichia coli* and *Serratia marcescens* at a frequency up to 100 MHz can be attributed to the β-dispersion. At these frequencies, proteins and other macromolecules of the bacterial cells polarize according to Markx *et al.* [35]. This effect decreases at frequencies above 100 MHz. With increasing frequency the influence of water becomes more prominent.
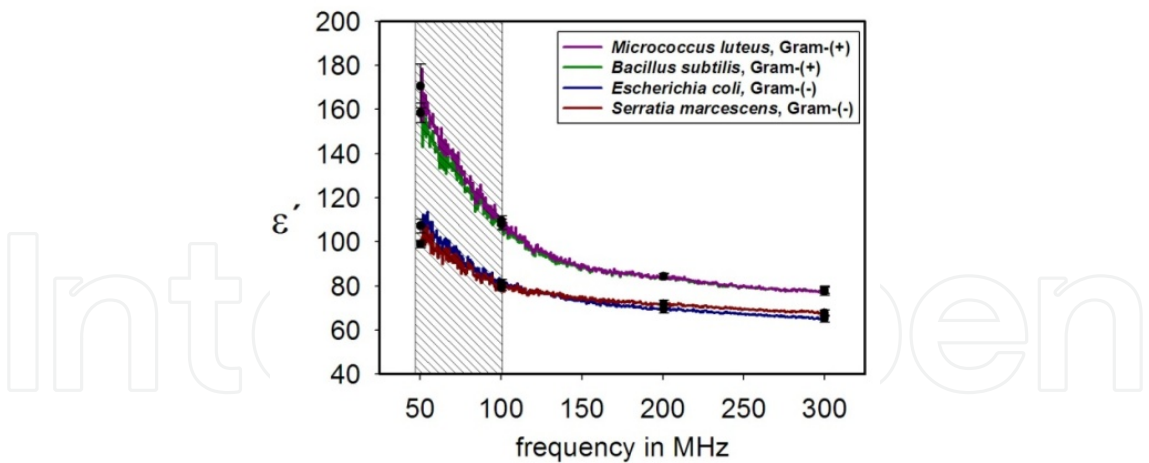
Figure 21. Discrimination of Gram-positive and –negative bacterial strains *via* dielectric spectroscopy. The diagram shows the real part of the permittivity ε' of the biomass of Gram-positive bacterial strains (*Micrococcus luteus* and *Bacillus subtilis* [upper curves]) and Gram-negative bacterial strains (*Escherichia coli* and *Serratia marcescens* [lower curves]) in a frequency range between 50 and 300 MHz. The highlighted area shows the most obvious region of differentiation between Gram-positive and Gram-negative bacterial strains [54].
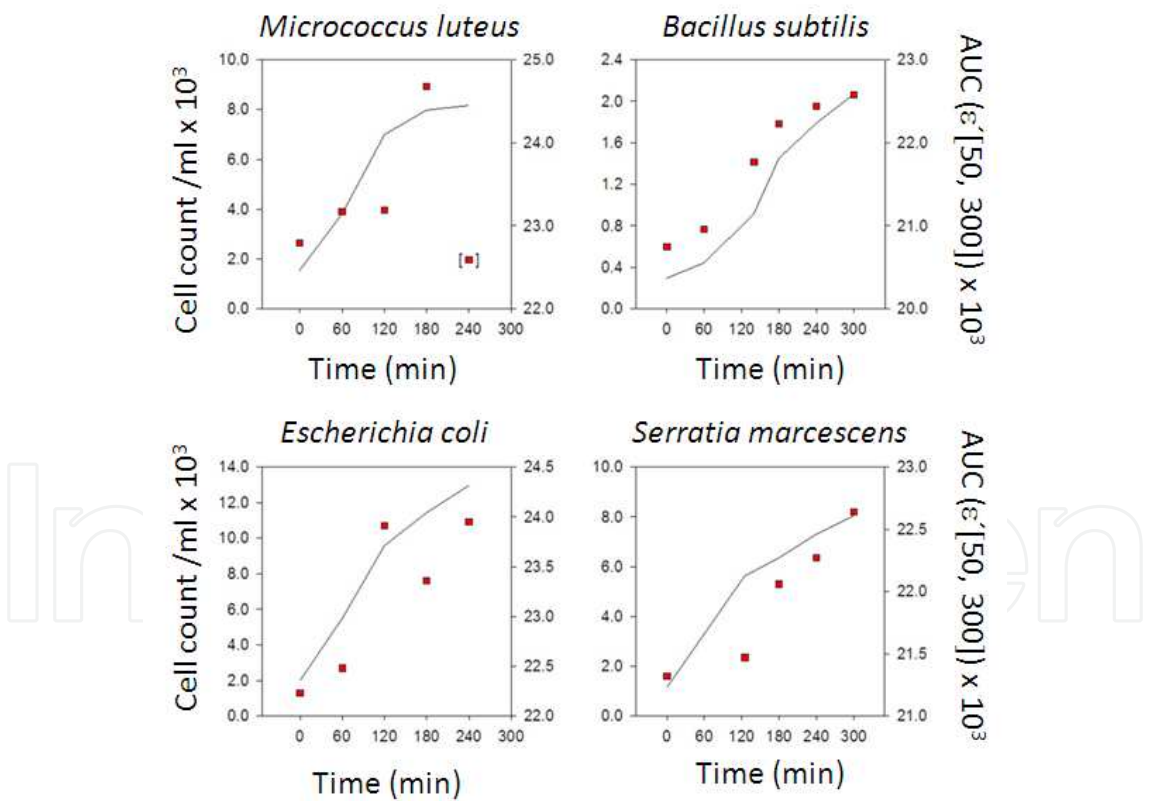

Figure 22. Monitoring of growth kinetics of four bacterial strains (growth phase). Red squares show the area under the curve (AUC) of the real part of permittivity ε' in a frequency range between 50 MHz and 100 MHz derived from measurements during the bacterial growth phase. The permittivity of the cell suspension was taken hourly for 240 or 300 min. Black lines show the cell count per ml taken at the same time as permittivity was measured [54].

All bacterial strains investigated in the present study revealed a characteristic time-dependent correlation between cell counts (black lines in Fig. 22) and ε' (red dots in Fig. 22). The growth kinetics was not influenced by the presence of accumulated metabolites in the culture medium since supernatants (liquid above precipitate) of every bacterial culture showed the same permittivity as the Standard I culture media (Fig. 22; $\varepsilon' = 85 - 78$ and $\varepsilon'' = 600 - 100$ @ $50 - 300\,\mathrm{MHz}$) [54].

3.4. Temperature influence on tissue permittivity

In therapeutic or diagnostic applications or biological effects of the electromagnetic field, dosimetric evaluations are greatly dependent on the precise knowledge of the dielectric parameters of biological tissues (relative permittivity ε and electrical conductivity σ). These parameters are sensitive to many influencing factors, which include the temperature of the target organ [55]. During radio-frequency or microwave radiation exposure, the internal temperature of tissue can change, thus influencing the electrical field distribution. For example, the evaluation of the lesion obtained by thermal ablation is a function of the relative permittivity and conductivity at 37°C and also of their evolution during heating. The influence of temperature in dielectric spectroscopy has been studied by several authors [56]-[58]. However, these effects remain misunderstood and the measured values are sparse at various frequencies and exist only for some organs.

To find out in how far temperature-dependent changes in permittivity can result in a parameter identified by ultra-wideband technology, water and different tissues were examined. To assess the basic capability of UWB radar for monitoring local temperatures, dedicated phantom and *in vivo* experiments were performed. Dielectric spectroscopy of water at different temperatures (25 – 80°C in steps of 5°C) and corresponding experiments using porcine and bovine tissue, such as udder, liver, muscle, and kidney revealed a distinct decrease of permittivity with increasing temperature. Nevertheless, heating of tissues to more than 60 °C might also reduce permittivity due to the reduction of water content. No distinct organ-specific differences in the temperature-dependent dielectric properties have been found so far (Fig. 23). Only fat, as low-water-content tissue, exhibited no influence on permittivity at different temperatures [59].

In addition to further studies with improved probes, corresponding analysis were performed using clinically approved temperature-based methods for tumor eradication, such as radio frequency ablation (RFA) or magnetic thermo ablation. For this experiment, a bovine liver was positioned onto a neutral electrode. The second, active electrode was launched into the liver tissue. Both electrodes together create a stress field, and the tissue around the active electrode becomes heated up to 60°C. Bi-static UWB antennas were first positioned in a distance to the region where RFA was thought to detect the signals of liver tissue itself. Then, the antennas were positioned above the region of radio frequency ablation, and changes in impulse response before, while and after radio frequency ablation were detected. The signal analysis displayed an increase of the impulse response during radio frequency ablation (data not shown) [59].
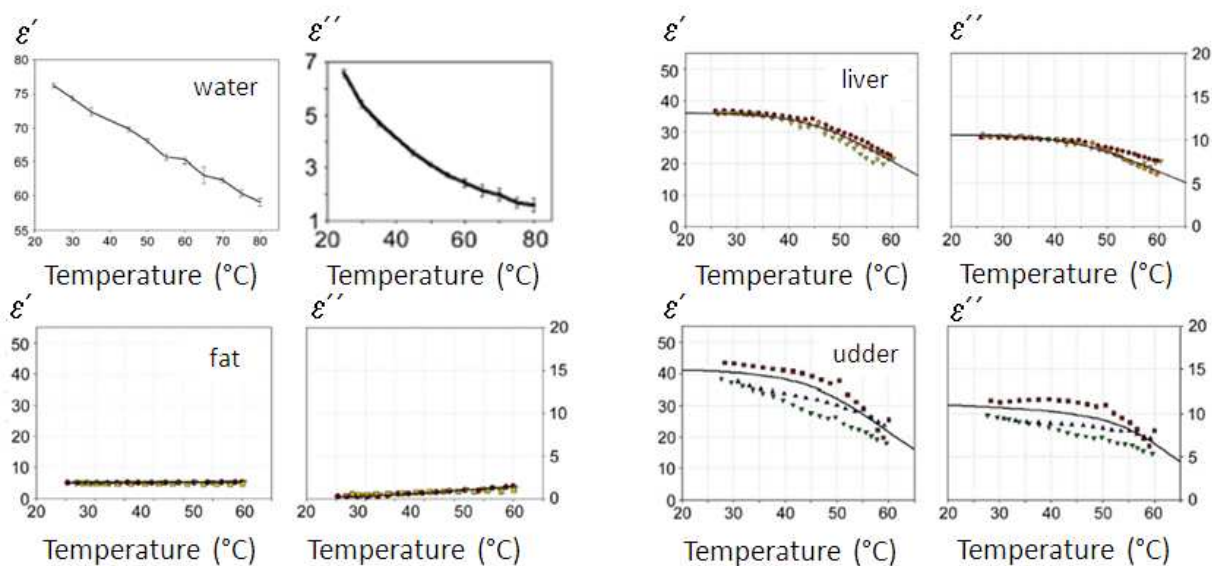
Figure 23. Real part (ε') and imaginary part (ε'') of the permittivity of water, liver, fat, and udder tissue at a frequency of 2 GHz is depicted. Water showed a constant decrease of permittivity in relation to the increase of the temperature. Liver and udder tissue showed a diminished deviation, and in contrast fat showed no change of the permittivity [59] at all.

The applicability of UWB for temperature monitoring was also assessed *in vivo* in mice. Prior to the start of experiments, mice were shaved at the abdominal region. Dielectric spectroscopy of the skin at the animal´s liver region before and after euthanasia showed a time-dependent increase of permittivity as a result of decreasing temperature with on-going time after euthanasia. The data provide a good basis for further development of UWB as a non-invasive temperature measurement technology.

3.5. Permittivity variations by contrast media

Microwave-frequency dielectric contrast between malignant and normal tissue in the breast serves as the physical basis for emerging microwave methods of detecting and treating breast cancer. The effective dielectric properties of breast tissue are influenced at microwave frequencies by endogenous polar molecules, such as free and bound water, peptides, and proteins. Consequently, the dielectric properties depend on the type and physiological state of the tissue. The effective dielectric properties - both the dielectric constant and effective conductivity - can also be influenced by exogenous molecules introduced as contrast agents [60].

Detection of dielectric properties of structures and tissues with similar characteristics (such as breast and breast tumor) pose challenges for imaging by ultra-wideband technologies. Therefore, a phantom serving as a model for blood vessels with a constant flow of ethanol (infusion fluid) was created (Fig. 24 left panel) for first trials to test the sensitivity of the measurement apparatus. Additions of contrast agents (in this case a mixture of ethanol and water) were determined [25]. Such basic search is useful for finding suitable contrast agents including feasibilities and limitations regarding the detectability of, for example,

concentration variations. The practice of clinical diagnostic radiology has been made possible by advances not only in diagnostic equipment and investigative techniques, but also in the contrast media that permit the visualization of the details of the internal structure of organs, which would not be possible without them. .The remarkably high tolerance of modern contrast media has been achieved through successive developments in chemical pharmacological technology.

The phantom serving as a model for blood vessels with a constant flow of ethanol was arranged. In the first step, the signals of this ethanol flow were received. By using a syringe *via* three-way cock 3 ml of the selected contrast agent (mixture of ethanol and water) were added, and the relative signal change was detected. The results show that with a decrease of water the signals become weaker (Fig. 24, right panel).
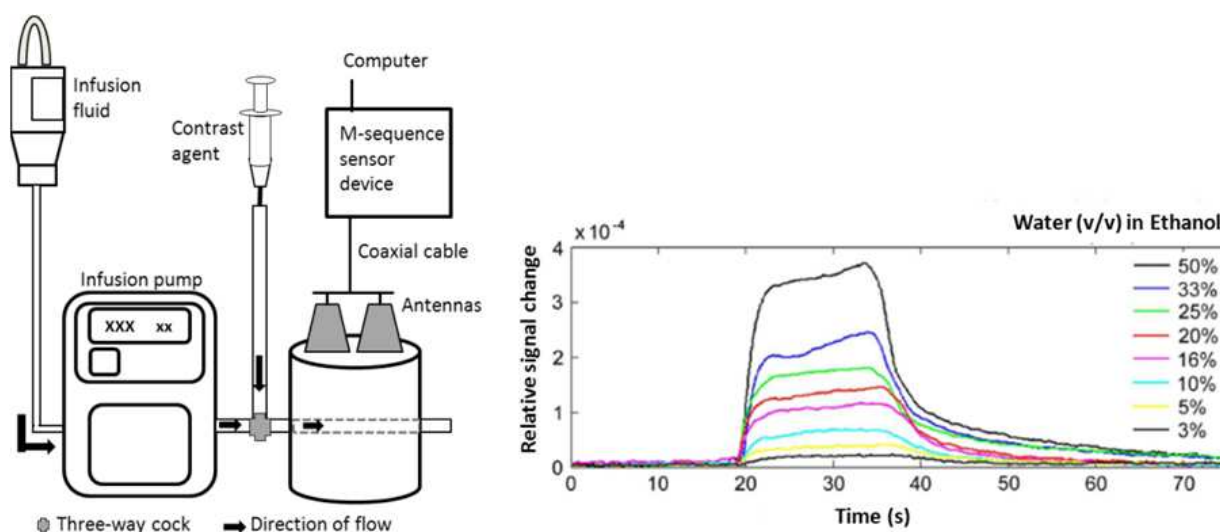

Figure 24. Depiction of the assembly of a phantom serving as a model for blood vessels with a constant flow of ethanol (left panel). The right panel depicts the relative signal variation (change of reflection coefficient) through adding 3 ml of contrast agent in relation to the virgin signal with constant flow of ethanol [43].

Even though dielectric spectroscopy of our group showed promising permittivity values of potential contrast agents such as physiological sodium chloride, the encountered permittivity increases *in vivo* are still to be enhanced to allow for a specific detection *via* UWB radar. One possibility to increase the capability of breast tumor imaging is the application of different clinically approved contrast agents such as ultrasound micro bubbles or iron oxide nanoparticles. Moreover, we expanded our investigations to the assessment of non-clinically approved agents (for example $BaSO_4$) in order to discover potential advantageous mechanistic conditions leading to local signal increase in terms of UWB diagnosis. Experiments will be systematically analyzed using dedicated phantoms, mimicking human tissues and blood flow.

Another challenge is the achievement of a selective accumulation of contrast agents in the target region to be detected by our UWB system. In this regard, a dynamic and transient accumulation *via* the tumor vascularization has been already postulated.

4. Remote organ motion tracking and its application in magnetic resonance imaging

4.1. Cardiac magnetic resonance imaging

Magnetic resonance imaging (MRI) is arguably the most innovative imaging modality in cardiology and neuroscience. It is based on the detection of precessing nuclear spins, mostly from protons of tissue water, in a strong static magnetic field. Using two additional kinds of magnetic fields, the position of the spins inside the human body can be encoded. To this end, the nuclear spin system is excited by resonant RF pulses at the precession frequency of the spin system. After excitation a macroscopic RF signal can be detected by an RF coil providing amplitude and phase information of the precessing nuclear magnetization. Applying additional magnetic field gradients the spin positions can be encoded by generating a well-defined spatial variation of the precession frequencies. Proper sequencing of spin excitation and gradient switching allows the reconstruction of 2D and 3D images from the acquired complex valued MR signals.

MRI data depend crucially on a multitude of physical parameters, e.g. moving spins will cause an additional phase modulation of the signal. One consequence is that MR images of the moving heart or of large vessels with pulsatile blood flow are severely distorted in the whole field of view. Hence, cardiac MRI (CMR) is seriously impaired by cardiac and respiratory motion when no proper gating with respect to both relevant motion types, cardiac and respiratory motion, is applied (Fig. 25). In clinically approved CMR procedures, electrocardiography (ECG) or pulse oximetry are used for cardiac gating and breath holding is applied for freezing respiratory motion [61],[62].
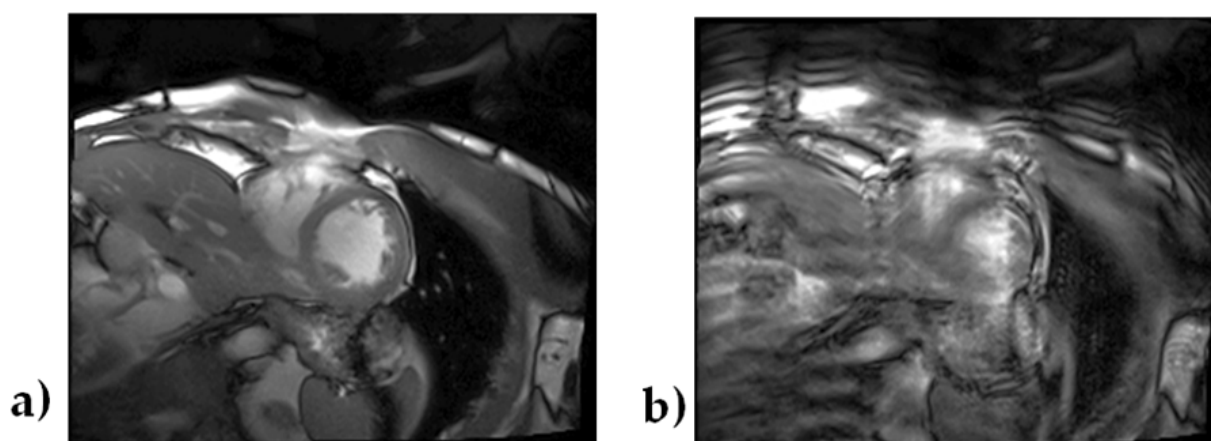

Figure 25. MR image (short axis view) of a human heart. a) Cardiac gating by pulse oximetry and breath hold; b) cardiac gating only, due to free breathing during image acquisition severe image artifacts occur

However, there are unmet needs of clinical CMR, particularly for high (≥ 3 T) and ultra-high (≥ 7 T) field MRI. Higher magnetic fields offer the chance to acquire images of better spatial resolution [63], but on the downside the ECG signal is increasingly perturbed by the magneto-hydrodynamic effect [64] until it becomes effectively useless for cardiac gating at

7 T. Furthermore, ECG electrodes are directly attached to the patient's skin, which may result in local RF burns. In addition, ECG and alternative approaches like pulse oximetric or acoustic cardiac triggering [65] do not provide any information about the respiratory state.

As a cardiac patient's breath hold is typically limited to about 15 s, a 3D whole heart coverage or imaging of the coronaries [66] would require proper respiration gating to acquire MR data under free breathing conditions. A well-established approach for respiration gating is the so-called MR navigator [67]. By means of some extra MR excitations, the momentary position of the diaphragm can be tracked over the respiratory. Unfortunately, these extra excitations interfere with the cardiac imaging sequence itself, making this technique complex and less reliable.

On this background, we propose the simultaneous use of multi-channel UWB radar and MRI to gain complementary information in particular for improving cardiac MRI. The anticipated potentials of this technique are (i) a contactless measuring principle for better patient safety and comfort, thus streamlining the clinical workflow, (ii) concurrent monitoring of a variety of body movements, (iii) direct relation to tissue mechanics [68], (iv) direct tracking of the temporal evolution of inner body landmarks, and (v) absence of any interferences of the UWB radar signals with the MR measurement if MR compatible designed UWB antennas are applied, (s. Section 2.3.3). The decomposition of physiological signatures in UWB radar data is the main challenge of this approach and a prerequisite for a reliable tracking of landmarks within the human body suitable for MRI gating.

Beyond MRI, there are a variety of other possible applications of in vivo UWB radar navigation systems in medical imaging or therapy. Examples are X-ray Computed Tomography (CT), Positron Emission Tomography (PET), Medical Ultrasonography (US), and Radiotherapy using photons or particles, or High Intensity Focused Ultrasound (HIFU). Lessons learned from all these approaches will foster medical applications of standalone UWB radar systems for intensive care monitoring, emergency medical aid, and home-based patient care [70].

4.2. Analytical and numerical modeling of the scenario

4.2.1. Channel-model

For modeling purposes, the human body can be approximated as a multilayered dielectric structure with characteristic reflection coefficients $\Gamma(f)$ (s. Fig. 26) [29], [71], [72]. The UWB signal, which can be a pulse or a pseudo-noise sequence [71] of up to 10 GHz bandwidth, is transmitted utilizing appropriate pulse-radiating antennas T_x (e.g., Double Ridged Horn or Vivaldi antennas). The reflected signal is detected by R_x, and the first step in further signal-processing usually is to calculate the correlation signal $R_{XY}(\tau)$ between received signal S_{Rx} and transmitted signal pulse S_{Tx} is [71], [72]. This represents the impulse response function (IRF) including the transfer functions of the antennas. By UWB measurement of the motion of a multi-layered dielectric phantom [29], the changes of reflections on the single interfaces can be found. Therefore, the signal variance $M(\tau)$ of the correlation signal $R_{XY}(\tau)$ is calculated.
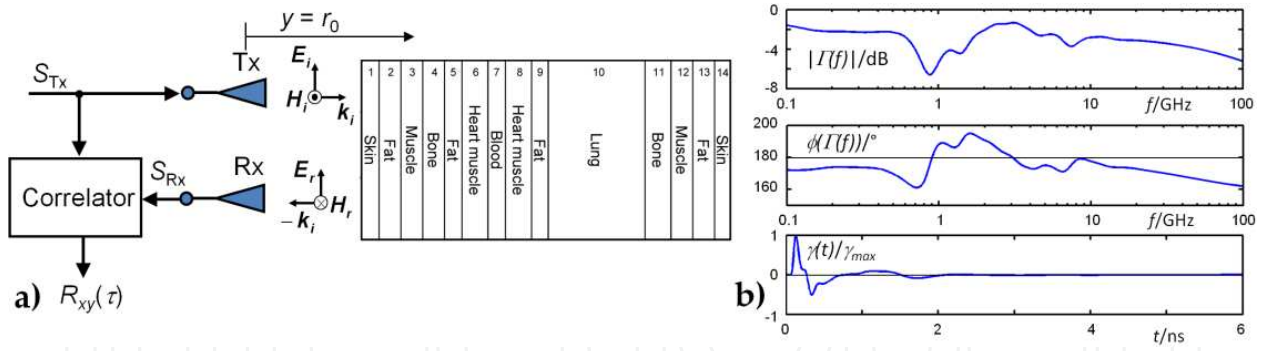
Figure 26. a) 14-layer arrangement to mimic the reflective properties of the human thorax (not to scale). E_i/E_r, H_i/H_r: incident/reflected electric/magnetic field component. k_i: wave vector of incident wave. **b)** Top: calculated magnitude of the reflection response $|\Gamma(f)|$, which is proportional to the frequency response function (FRF) of the object. Middle: unwrapped phase $\phi(f)$ of the reflection response $\Gamma(f)$. Bottom: normalized time domain representation $\gamma(t)$ of $\Gamma(f)$ impulse response function (IRF) of the reflection response.
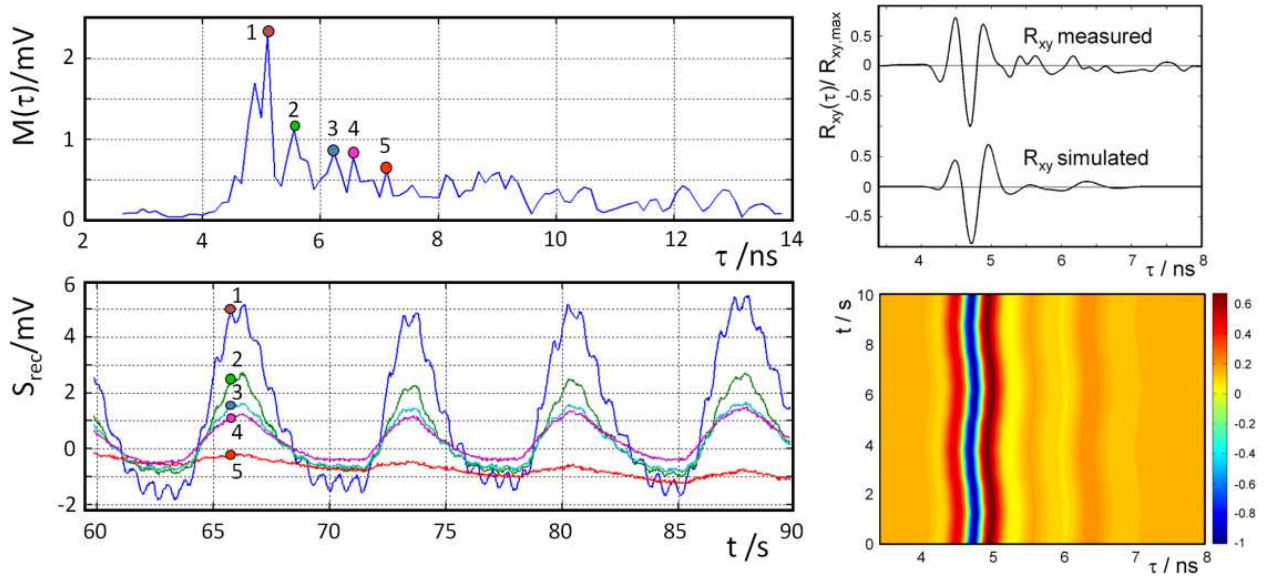

Figure 27. Physiological signatures received by the algorithm described in Ref. [29]. Top: Signal variance $M(\tau)$. Bottom: Physiological signatures corresponding to the label local maxima of $M(\tau)$. Top right: Measured and simulated correlation signal $R_{xy}(\tau)$.
Bottom right: Radargram of the measured and simulated correlation signal $R_{xy}(\tau)$.

The maxima in $M(\tau)$ correspond to the interfaces containing a considerable difference in the permittivity or are close to the illumination side if the transfer functions of the antennas are removed by de-convolution. By these maxima, the time signals corresponding to the interfaces can be extracted [29]. An example of simulated and measured correlation signal $R_{xy}(\tau)$ is given in Fig. 27, top right.

4.2.2. Analytical simulation of the intracranial pulsation detection

It is well known that simultaneously to the head's vibrations intracranial oscillations with spatial varying amplitude occur, induced by physiological sources [73]. Thus, it is only

logical to ask whether these oscillations are detectable by UWB radar. Due to the simultaneous occurrence of the intracranial displacement and the vibration of the whole head, decomposing both signals requires sophisticated methods. As an initial step towards the solution to this problem, we need to get a feeling for the change in the acquired UWB reflection signal due to an intracranial oscillation. An analytical approach [71], [72] was applied which models the signal path and the oscillating stratified arrangement of the brain to get signals free of any interfering compositions. Figure 28 schematically depicts the set-up used to probe the human body with a UWB device, where S_{Tx} symbolizes the excitation signal and S'_{Tx} its temporal derivative representing the free space signal E_i in the channel. By the convolution of the impulse response function γ of the multilayered dielectric structure with S'_{Tx}, the reflected electric field component $\gamma * S'_{Tx} = E_r$ is archived and, accordingly, the received current signal $S_{Rx} = (\gamma * S'_{Tx})'$. The $*$ symbol represents the convolution operator.
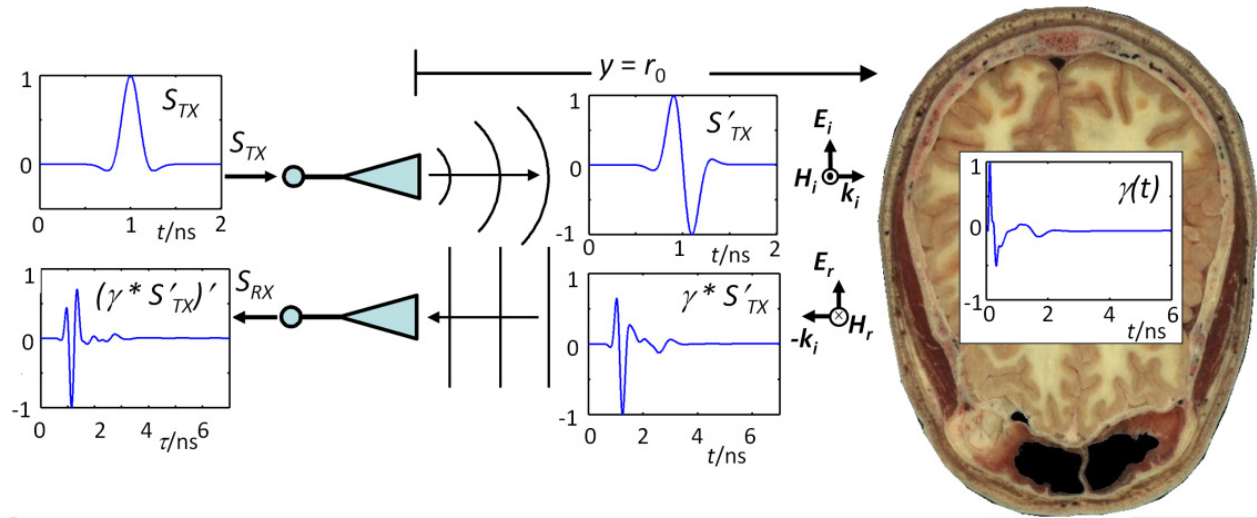

Figure 28. Signal path model for the current transfer function S_{Rx}/S_{Tx}.

Therefore, the spectral response of a dielectric medium is appropriately described in terms of a multiple Cole-Cole dispersion, which – by choosing parameters appropriate to each constituent - can be used to predict the dielectric behavior over the desired frequency range [71]. For such a layered arrangement, the reflection coefficient $\Gamma(\omega)$ can be calculated recursively. In this manner, the response of $\Gamma(\omega, t)$ to the variation of a certain internal interface can be analyzed [68], [73]. We simulated the physiological event by variations of $\Gamma(\omega, t)$, which is done by a sinusoidal oscillation of the white matter. Accordingly, the cerebro spinal fluid varies antipodally [76]. The correlation result $R_{xy}(\tau, t)$ was calculated just as its variation after a certain propagation time. The reconstruction of the intracranial motion applying the reconstruction algorithm proposed in [72] gave us a maximum deviation from the reference oscillation of about 4%. We conclude that the detection of intracranial oscillations using non-contact UWB is indeed feasible [72], [73]. It must be noted that for all real medical applications of this broadband technique trying to monitor variations of the body's interior, sophisticated signal processing techniques must be applied to decompose signals originating from the body's surface and signals originating from deeper sources [74]. The influence of the antenna's transfer function, in contrast, is less of an

issue for real applications. For simplicity, we had assumed an ideal transfer function in the above simulation but non-ideal antenna behavior can be extracted from the received signal by using proper de-convolution techniques. Furthermore, the time courses of the ideal channel can be regained [72].

4.2.3. Full simulation of the electromagnetic field distribution

Beside the analytical approach, we are interested in the detailed temporal evolution of the electromagnetic fields inside and outside the human thorax. To this end, we investigated complex arrangements mimicking the illumination of a realistic human torso [75] model incorporating the geometry of the antennas by finite-difference time-domain method (FDTD) simulations. By FDTD simulation, we studied, e.g., the dependence of the illumination and detection angles of the transmission and receiving antennas on the quality of the received signal, *i.e.* the correlation result. In this way, an estimate of the optimized antenna placement can be found. Furthermore, by varying organs' boundaries by changing their thickness or/and placement of one or more tissue layers, different functional states can be investigated, e.g. the end-systolic and end-diastolic phase of the myocardium, which consequently determines a characteristic change of the received signals.
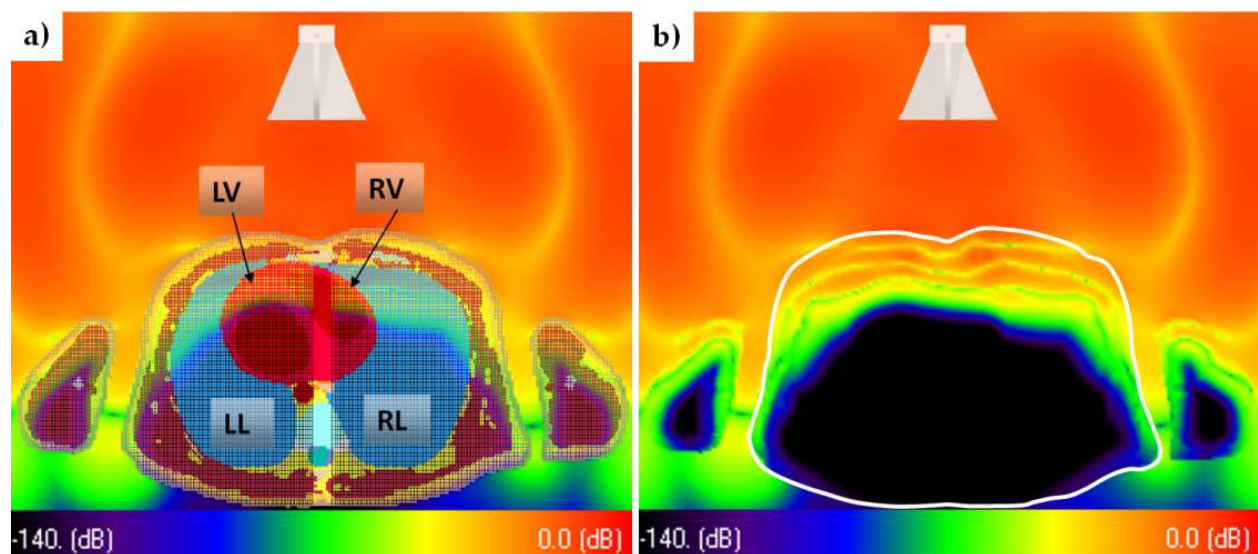

Figure 29. Extra- and intra-corporal electrical field distribution in an axial cross-section of the upper human body **a)** with tissue mesh; **b)** without the mesh showing the wave propagation intra-corporal. The thorax's contour is highlighted by the white line.

An example of the complex wave propagation inside the human torso is shown in Fig. 29. Due to the higher permittivity ε inside the body, the propagation velocity is slowed down according to $c = c_0/\sqrt{\varepsilon}$. Hence, a bending of the extra- and intra-corporal wave fronts results. The transmitted spherical wave fronts are refracted towards the center of the thorax, which is beneficial for the illumination of the myocardial section lying deeper inside the thorax. By these simulations, we achieve an in-depth understanding of the complex electromagnetic field distribution and the dependencies of the resulting output signal of the receiving antenna [73]. Therefore, the results of these simulations are helpful to increase the accuracy

of reconstructed physiological signatures from deep sources by finding the optimized antenna position regarding the better penetrability of selected body areas. This, of course, requires the adaptation of the model to the actual thorax geometry of the patient as obtained by MRI scans.

4.3. Detection of motion by UWB radar

4.3.1. Motion detection for a multilayered phantom

We compared the motion detection by variance calculation in a combined MRI/UWB measurement using appropriate MR-compatible phantoms [29]. The dielectric phantoms were arranged in a sandwich structure to mimic the sequence of biological tissue layers of the human thorax.
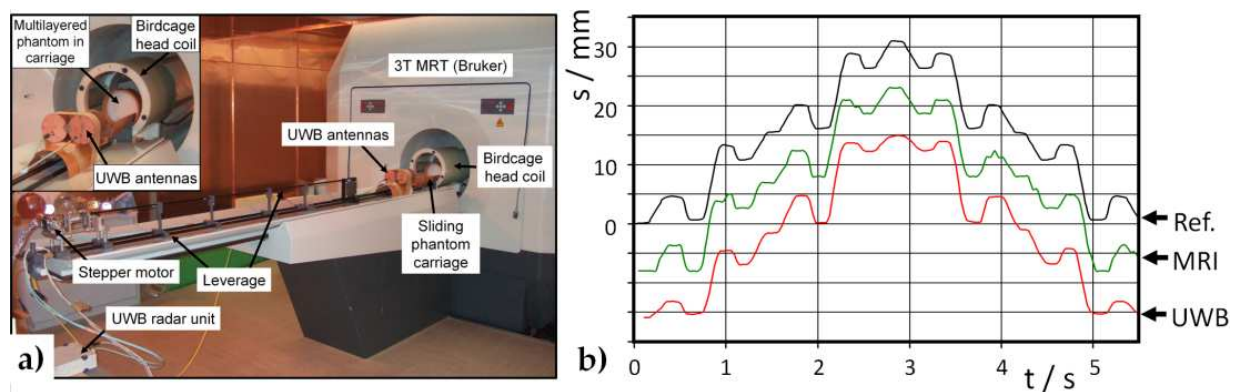

Figure 30. **a)** Set-up of the combined MRI/UWB measurement; **b)** Comparison of the reference profile with the data obtained simultaneously from MR and UWB radar measurements. The profiles are offset for clarity.

Such a sandwich was placed in a moveable sledge-like fixture inside a birdcage MR head coil. The motion profile of the sandwich structure was shaped to approximate respiratory motion of the thorax superimposed by cardiac oscillations (Fig. 30). An M-sequence UWB-Radar system (up to 5 GHz) [76] and MR compatible UWB antennas [10], [32] were utilized to detect the motion of the phantom inside a 3-T MR scanner (Bruker MEDSPEC 30/100). A flow-compensated gradient echo CINE (time resolution 50 ms) sequence was used to reduce artifacts generated by the phantom movements.

Additionally, the physiological signatures monitored by UWB-radar were validated by comparison to simultaneously acquired MR measurements on the same subject [13], [29], [77] (cf. Section 4.5.2 and 4.6).

4.3.2. Detection of micro motion

Subject motion appears to be a limiting factor in numerous MR imaging applications especially in the case of high and ultra-high fields, e.g. high-resolution functional MRI (fMRI). For head imaging the subject's ability to maintain the same head position is limiting the total acquisition time. This period typically does not exceed several minutes and may be

considerably reduced in the case of pathologies. Several navigator techniques have been proposed to circumvent the subject motion problem [73]. MR navigators, however, do not only extend the scan because of the time necessary for acquiring the position information, but also require additional excitation pulses affecting the steady-state magnetization. Furthermore, if the very high spatial resolution offered by ultra-high-field MR scanners shall be exploited, the displacements caused by respiration and cardiac activity have to be considered. Thus, we propose to apply an UWB radar technique to monitor such micro motions.
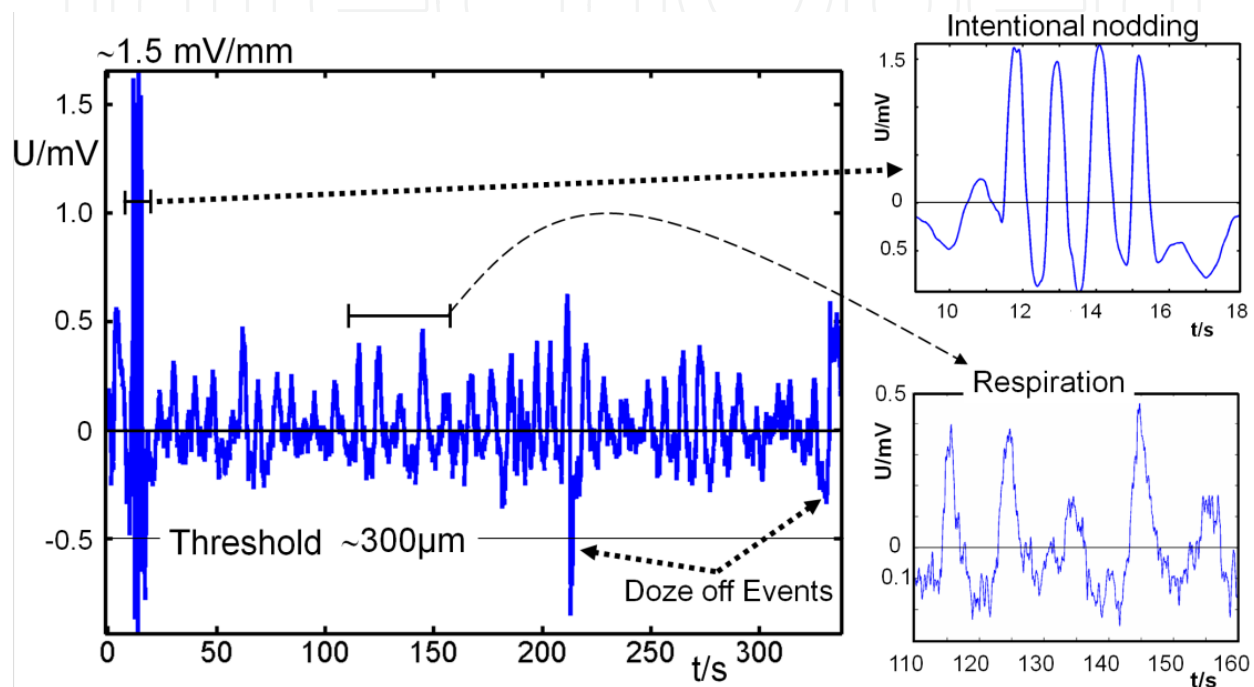

Figure 31. Motion reconstructed from a measured time interval of 350 s. The right inset at the top displays the four nodding events (~1 mm amplitude, episode [t = 10 s,…, t = 18 s]) to localize the surface of the head. Respiratory displacements are clearly visible (right inset bottom, episode [t = 110 s,…, t = 160 s]) and spontaneous twitches are highlighted.

First *in-vivo* motions reconstructed from a measured time interval of 350 s are shown in Fig. 31. By applying appropriate filters in a selected time interval even the cardiac induced displacements were detected with an amplitude of about 40 μm. Thus, we could detect all kinds of involuntary motions (respiratory, cardiac), but also doze-off-events are visible, demonstrating the feasibility of interfacing an MR scanner with an external UWB radar based motion tracking system. Our system is capable of determining the position of interest with sub-millimeter accuracy and an update rate of 44.2 Hz. Using the UWB tracking data of the volunteer's head, the motion artifacts can be compensated for in real time or by post-processing enhancing the actual resolution of the MR scan [73].

4.3.3. Separation of motion components by blind source separation

Monitoring the motion inside the human body, the correlation functions of transmitted and received signals (i.e. the IRF) contain a mixture of all simultaneously occurring motions.

Especially for the human torso where - due to higher harmonics from the highly nonlinear respiratory cycle - the separation of the cardiac cycle by common signal filtering in the frequency domain is limited, another separation of motion components is necessary. For this reason, the separation of motion components based on blind source separation (BSS) was developed.

The IRF from a single UWB shot is a time series of 511 data points with a dwell time of 112 ps. This defines an IRF time scale of 57 ns but is still instantaneous compared to anatomical motions. These shots are then repeated for instance 2000 times at a rate of 44 Hz covering a total time span of 45 s. For further analysis, only the most interesting regime of the IRF data is considered. These are the 100 data points, i.e. a window of 11.2 ns, right after the IRF maximum due to direct cross-talk between *Tx* and *Rx* antenna. Following the temporal evolution of each selected data point over the 2000 repetitions, 100 virtual channels are obtained and subjected to BSS decomposition (ROI, see Fig. 32.a). By removing the mean values in these virtual channels, the changes of the radar signal on the anatomical time scale become visible, see Fig. 32.b. The motion pattern is dominated by respiration; cardiac motion is considerably smaller and not immediately visible in the raw data.
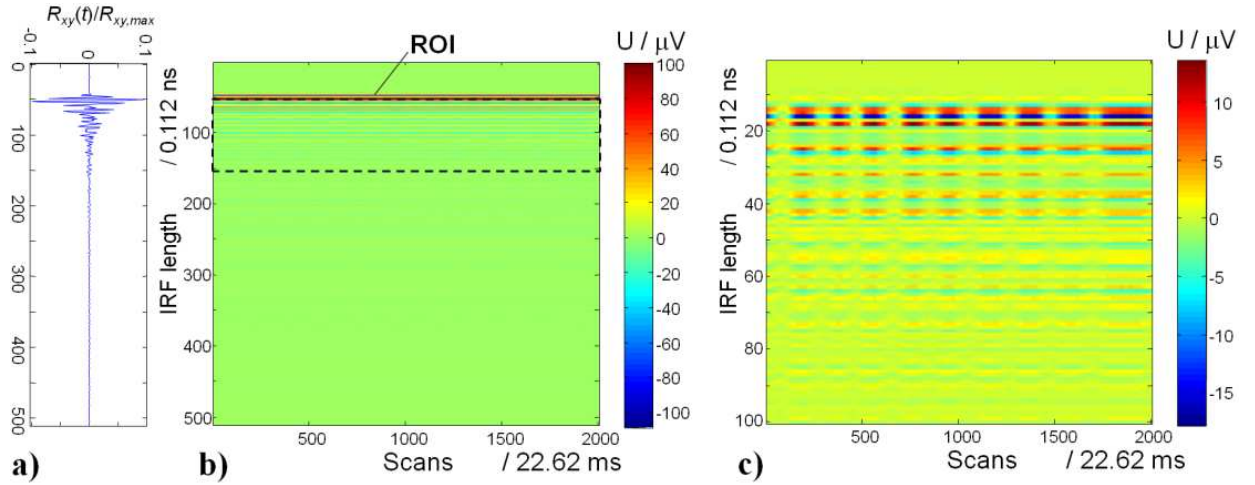

Figure 32. a) Single IRF and **b)** radargram of one channel with region of interest and **c)** selected 100 virtual channels, mean value removed

The data analysis is based on the BSS and assumes a measured signal $x(t)$ to be a linear combination of unknown zero-mean source signals $s(t)$ with an unknown mixing matrix $\mathbf{A}$:

$$x(t) = \mathbf{A}s(t) \quad x = (x_1, ..., x_m)^T \cdot \tag{2}$$

The original sources $s(t)$ can be estimated by the components $y(t)$ which can be calculated from the estimation of the de-mixing matrix $\mathbf{A}^* \approx \mathbf{A}^{-1}$:

$$y(t) = \mathbf{A}^* x(t) = \mathbf{A}^* \mathbf{A}s(t) \tag{3}$$

In our analysis, a second-order time-domain algorithm (TDSEP, Temporal Decorrelation source SEParation) was applied which is described in detail in [78]. In TDSEP the unknown

mixing matrix **A** is calculated by simultaneous diagonalization of a set of correlation matrices $\mathbf{R}_\tau(x)$ for different choices of τ.

$$\mathbf{R}_{\tau(x)} = \left\langle x(t)x^T(t-\tau) \right\rangle$$

$$\mathbf{R}_{\tau(x)} = \left\langle \mathbf{A}s(t)(\mathbf{A}s(t-\tau))^T \right\rangle = \mathbf{A}\mathbf{R}_{\tau(s)}\mathbf{A}^T \qquad (4)$$

where the angular brackets denote time averaging. The quality of signal separation depends strongly on the choice of τ. However, solving $\mathbf{R}_\tau(x) = \mathbf{A}\mathbf{R}_\tau(s)\mathbf{A}^T$ for several τ by simultaneous diagonalization eliminates this obstacle. It is recommended by biomagnetic research to choose the number of time shifts τ larger than 40 and to include the time constant of those components which are known a priori, e.g. the range of possible cardiac frequencies $1/\tau_{cardiac}$ [79]. Additionally, Principal-Component Analysis (PCA) compression was applied to reduce the number of channels used for generating the correlation matrices $\mathbf{R}_\tau(x)$ and reduce computation time for the BSS. The components of the resulting sources are calculated using eq. (3). Automatic identification of the cardiac component was provided by a frequency-domain selection criterion because for non-pathological conditions the main spectral power density of the heart motion falls in a frequency range of 0.5 Hz to 7 Hz. The algorithm searches for the highest ratio between a single narrowband signal (fundamental mode and first harmonic) within this frequency range and the maximum signal outside this range. A high-order zero-phase digital band pass filter of 0.5–5 Hz was applied to the cardiac component of the UWB signal. In a similar way, respiration can be identified by the BSS component with the maximum L2 norm in the frequency range of 0.05 Hz to 0.5 Hz.

4.4. Analyses of cardiac mechanics by multi-channel UWB radar

4.4.1. Compatibility of MRI and UWB radar

Compatibility is the most challenging issue when combining MRI with other modalities. Therefore, the UWB antennas employed are important parts. Eddy currents due to the switching magnetic gradient fields as well as the interference with the powerful RF pulses from the MRI scanner, see Section 2.3.3, were minimized by proper antenna design. The cut-off frequency of the MR-compatible double ridged horn antennas at 1.5 GHz [32] marks the lower limit of the transmitted and received signal frequencies. Coupling to the narrowband MRI frequencies (300 MHz at 7 T, 125MHz at 3T) is thus minimized in both directions. Additionally, the inputs of both our UWB radar systems (MEODAT GmbH, Ilmenau, Germany), one single-module: 1Tx-2Rx-device and one four-module multi-input-multi-output: 4Tx-8Rx-MIMO device, were protected by 1.2 GHz high pass filters. In both UWB systems, the transmitted radar signals were generated by a pseudo-random M-sequence. With $m = 9$ it has a length of $2^m-1 = 511$ clock signals at $f_0 = 8.95$ GHz [76]. The equivalent UWB power spectrum extends up to $f_0/2$. The impulse response function (IRF) is obtained as mentioned before by correlation of the received signal of the investigated object with the M-sequence [76]. By means of this technique, the signal-to-noise ratio is improved due to the removal of the uncorrelated noise by the correlation of the received signals with the transmitted signal pattern. In this way, even smallest parts of the RF pulses of the MRI were avoided.

4.4.2. Multi-channel UWB radar applying two receiver channels for cardiac trigger events

We started our multi-channel UWB radar development with the single module device enabling us to add a second receiver (*Rx*) antenna, oriented towards the left-anterior oblique direction [68] (Fig. 33.a), to the existing *Rx* and *Tx* antennas facing the antero-posterior direction. The UWB data were recorded at 44.2 Hz. Corresponding to the data selection in Section 4.3.3, we obtained 200 virtual data channels from the IRFs of two UWB measurement channels for the decomposition by blind source separation (BSS).
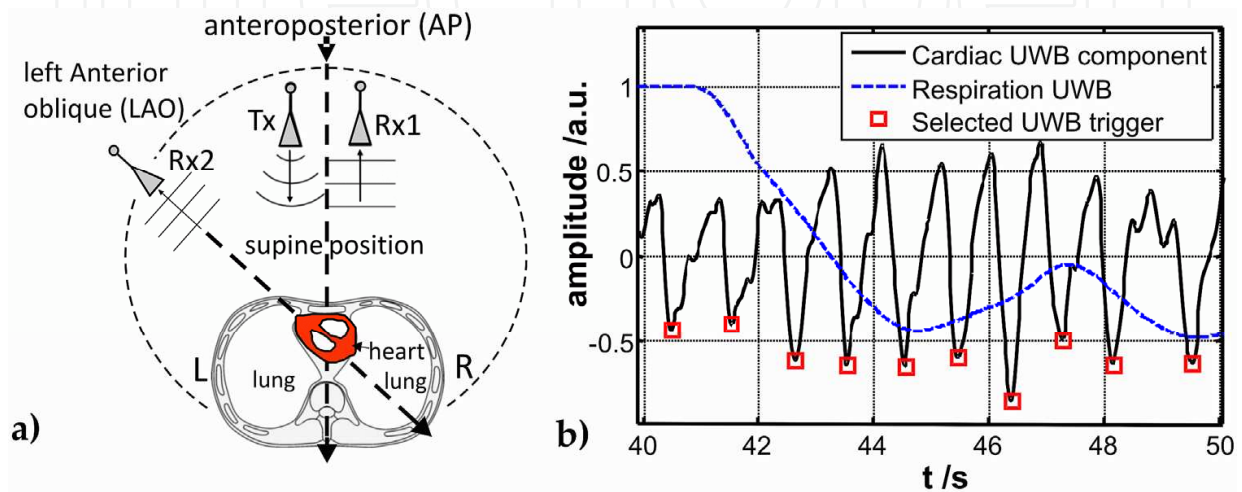

Figure 33. a) Scheme of the UWB radar with one transmitter (*Tx*) and two receiver (*Rx*) antennas and measurement set-up; **b)** Cardiac UWB signal applying both *Rx* channels and the calculated trigger events in the signal by combination of low peak and slew rate calculation.

In the cardiac UWB signal, we chose the points of maximum myocardial contraction during the heart cycle. These points are related to the minima of the UWB signal (Fig. 33.b: squares). To increase the robustness of this detection scheme, we combined it with a simple difference calculation at the trailing edge of the minima. Additional consistency checks on the oscillation amplitude were used to suppress double triggering.

By employing two *Rx* channels (Fig. 33.a) the UWB radar detection of the cardiac cycle worked reliably, even in the free breathing mode. In simple cases, e.g. under breath-holding conditions, it is possible to detect cardiac motion with just one *Rx* channel. However, this will not work in general, more complicated situations.

4.4.3. Application of up to 32 receiver channels

By using two *Rx* channels, it was still necessary to align the antennas properly towards the heart. This becomes more critical for measurements during cardiac MRI where the MR coil is placed on the chest of the subject, partly blocking the free line of sight between radar antenna and the heart, see Fig. 38. With our development of a multiple-antenna set-up it is much easier to handle this adjustment by just choosing the 'good channels' in a pool of available channels.

By integration of a MIMO UWB device (MEODAT GmbH, Ilmenau, Germany) containing four modules, each with one *Tx* and two *Rx* channels [76], up to 32 channels became available. In a 1 *Tx* * 8 *Rx* configuration a sampling frequency up to 530.4 Hz can be realized. Using sequentially activated transmitters the set-up can be extended to 32 channels (4 *Tx* * 8 *Rx*) at a reduced sampling frequency of up to 132.6 Hz. For cardiac motion detection, the four *Tx* and eight *RX* antennas are placed over the chest as depicted in Fig. 34 and adjusted to aim for one central point at a distance of 100 cm.
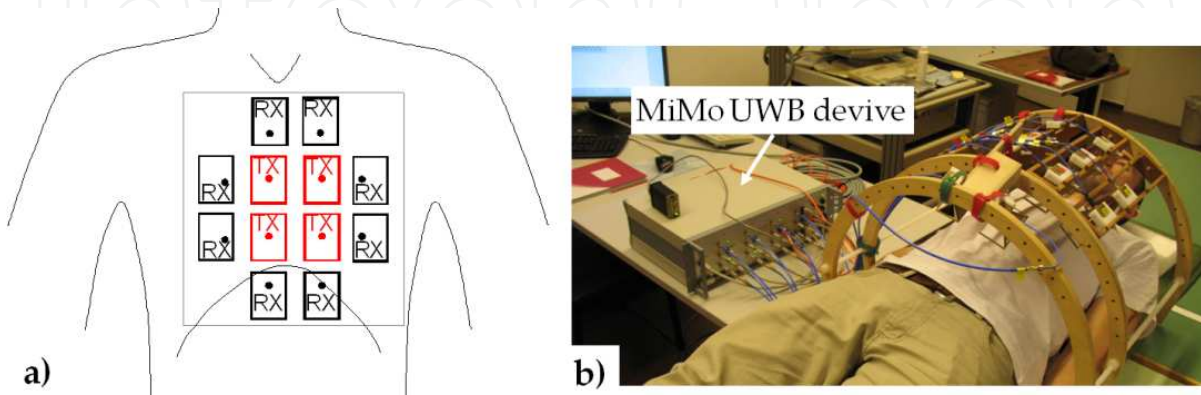

Figure 34. a) Scheme of the UWB radar set-up with 8 *Rx* and 4 *Tx* antennas b) MR compatible measurement set-up.
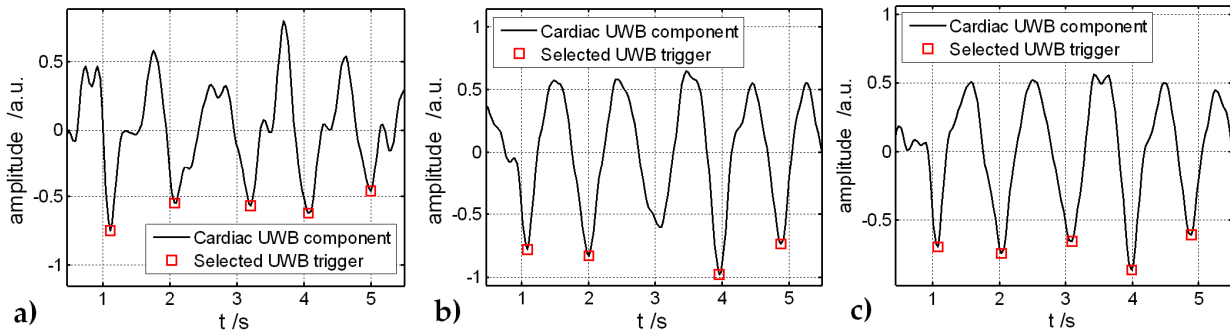

Figure 35. Cardiac signal and detected trigger events for **a)** two hand-picked best channels, **b)** all 32 channels, **c)** the 24 "good channels".

The procedure to identify the most useful channels for triggering starts with a short preparatory measurement, where each channel is analyzed by the BSS to decompose the complex UWB signals [80], extracts the relevant cardiac component and calculates the trigger events as described in Section 4.4.2. The quality of each measurement channel is assessed by calculating the variation of the time interval between trigger events. For comparison, Fig. 35.a depicts the result of the BSS analysis by the best two channels, manually selected for the smallest variation between the trigger events. The cardiac signal based on these two hand-picked channels represents the best achievable result for a set-up like in the section before. By utilizing all 32 channels for the BSS, a smoother cardiac signal is detected, and the motion amplitude shows less variation over the time. However, the sharpness of the trailing slopes is also reduced. Due to this fact, the third trigger event escaped detection (s. Fig. 35.b). Some of the 32 channels contained much noise resulting in a

jitter of their trigger contributions and smearing out the sharpness in the combined signal determined by the BSS. By the preparatory check those channels with the highest variation in their 'cardiac' signals were excluded as they were likely contaminated with noise or other motion components. By rejecting the eight noisiest channels and recalculating the BSS with the remaining channels, a cardiac signal is obtained with sharp trailing slopes and well-defined trigger events (s. Fig. 35.c).

The primary goal of this development was to simplify the system handling during cardiac navigation for high-resolution MRI. In addition, the capability of monitoring non-invasively the cardiac activity of a person in an unknown position, e.g. in a patient bed, can be important for a variety of novel medical applications in clinical medicine and biomedical research. As multi-channel UWB radar is unimpeded by bedding or clothing, it is applicable not only in conjunction with MRI. It would also be a valuable stand-alone modality for intensive care monitoring of patient groups not permitting the use of skin contact sensors. Neonates, children at risk of sudden infant death syndrome or burn victims are just a few examples.

4.4.4. Illumination of human thorax by multiple antenna groups

Stand-alone UWB radar enables the detection of cardiac activities by different illumination conditions as shown in [68] for the radiographic standard position. The illumination of the heart from only one side at a time, like the frontal direction for motion detection as depicted in Fig. 33, was extended to the simultaneous illumination of two sides. No averaging was performed to enable the comparison of single heart beats [30]. This approach can open the field for new diagnostic applications by detecting differences and disturbances in comparative measurements of the left and right ventricle, thus recognizing potentially pathological patterns [69]. Two groups of four Rx and one Tx antennas were applied for this purpose. The first was placed in the left lateral and the second in the right anterior oblique position.

Each antenna group consisted of a single Tx antenna surrounded by four Rx antennas. All antennas were directed towards the estimated center position of the heart. The challenge was to measure the cardiac motion even from the lateral position, where the attenuation of the reflected signals from the heart is much higher due to the prolonged propagation path in tissue. The data analysis by BSS was applied for both antenna groups separately. For comparison, the data of only two or all four Rx channel per group were analyzed.

For lateral position, the UWB signal from the cardiac motion is considerably weaker and much more affected by noise. However, by increasing the number of Rx- channels, the signal quality improved substantially, effectively compensating the strong signal attenuation (s. Fig. 36.b). Only healthy volunteers were examined in this particular study but even among them characteristic peculiarities can be found. In both ventricles, the contraction velocity (trailing edge of the UWB motion curve) is higher than the velocity of ventricle dilatation. The duration of the dilation period, on the other hand, is longer for the right ventricle compared to its counterpart on the left. More characteristic features are expected to be visible in patients with cardiac diseases or malfunctions.

4.5. Simultaneous cardiac UWB/ECG, UWB/MRI measurements

4.5.1. UWB radar and high resolution ECG

UWB and ECG were simultaneously acquired. The radar system was equivalent to Section 4.4.2 with one *Tx* and two *Rx* channels. The ECG was recorded with two channels (left arm and left leg against right arm) at a sampling frequency of 8 kHz. For the UWB signals sampled at 44.2 Hz, the same data analysis (see Section 4.4.2) was applied to extract the cardiac signal and determine the trigger events. The usual R-peak detection was applied to trigger on the ECG signal. Cardiac UWB and ECG signals were both re-sampled at 1 kHz to retain more detailed information of the ECG.

The point of maximum mechanical contraction of the heart in the cardiac UWB signals (s. Fig. 37.a) is delayed to the ECG R-peak, indicating the point of the myocardium's peak electrical activity. Therefore, we have to be aware of the difference between detecting cardiac mechanics by UWB radar and the heart's electrical activity by ECG. For the goal of MRI gating, however, the important thing is the existence of a fixed temporal relationship between ECG and UWB signals with as little jitter as possible. For the time lag between ECG and UWB trigger events, we obtained a standard deviation of less than 20 ms which is already smaller than the UWB sampling time of 22.6 ms. This result proves the consistency and robustness of our procedure.
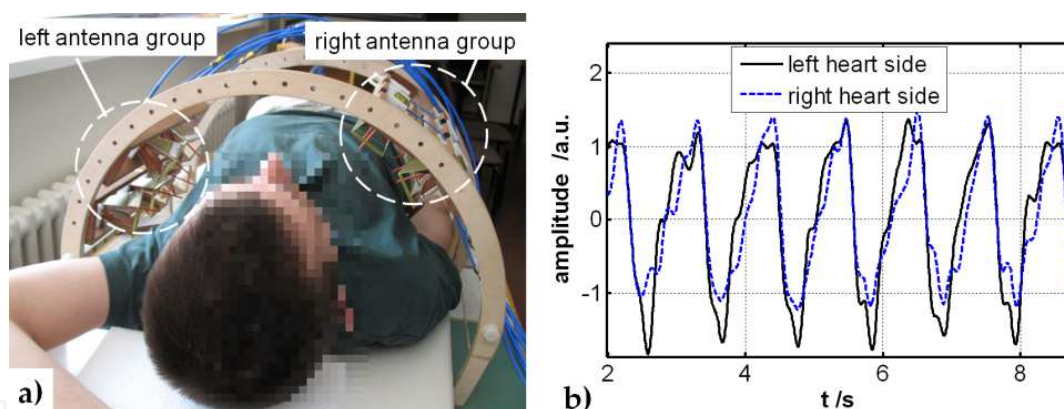

Figure 36. a) Measurement set-up with two antenna groups for separate monitoring of the heart's left and right ventricle; **b)** Cardiac signal for left and right ventricle applying four *Rx* channels.
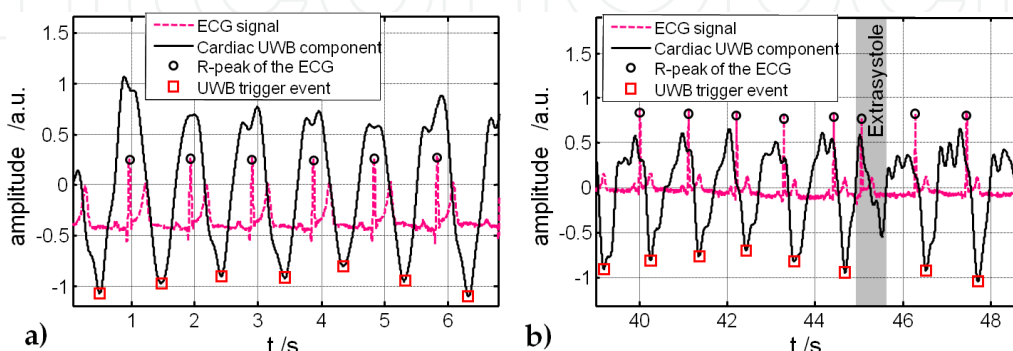

Figure 37. a) ECG signal with R-peak trigger events and UWB signal with trigger events located at the maximum of mechanical contraction; **b)** Measurement with an extra-systole.

Another measurement example depicted in Fig. 37.b shows a cardiac sequence containing an extra-systole at 45.5 s. In the ECG signal, this appears as a spontaneous change in the R-R-duration. In the cardiac UWB signal, we observe an incomplete contraction of the myocardium due to the "erroneous" electric excitation. Consequently, no trigger event was generated by this extra-systole. This ability to analyze cardiac mechanics by stand-alone UWB radar or in conjunction with ECG can be exploited, e.g., for infarction detection, as ischemic tissue shows a modified contraction pattern.

4.5.2. Comparison of cardiac UWB Signal and one dimensional MRI

For better understanding the relationship between actual cardiac mechanics and UWB motion-detection signals, a fast MR-sequence was developed with the aim to monitor myocardial landmarks inside the human body in real time. We implemented a very fast 1D gradient echo sequence for low RF power deposition in tissue and high scan repetition frequency on our MR scanner [77]. One dimensional MR profiles and motion sensitive UWB data were acquired simultaneously allowing the comparison of both techniques and hence a verification of the UWB radar navigator. MR compatible UWB antennas [32] mounted above the chest were directed towards the heart (s. Fig. 38). A flexible RF coil with large openings was used to detect the MRI signal. The UWB data were sampled at 132.6 Hz. Using one Tx and five Rx UWB antennas 500 virtual channels could be constructed from the IRFs.
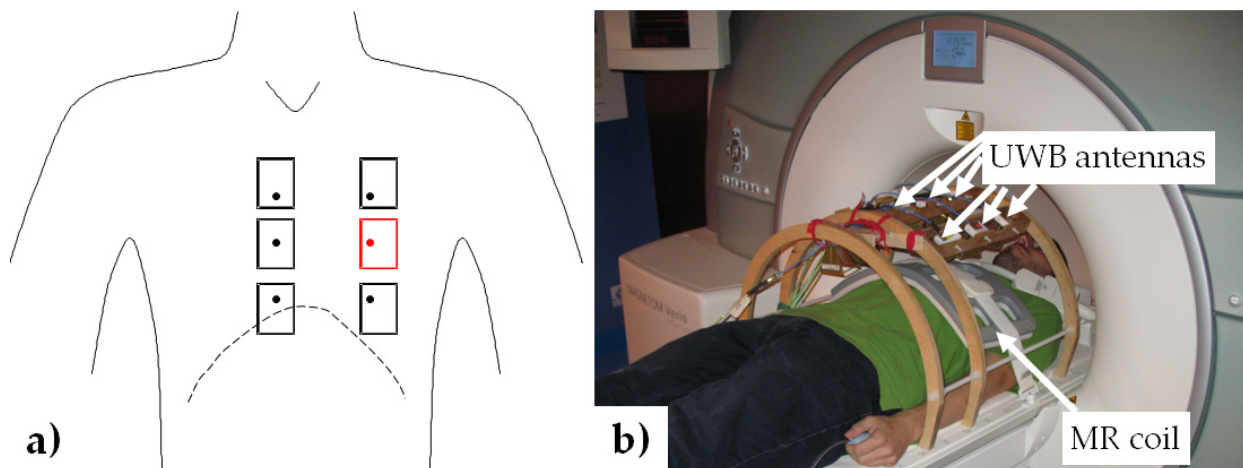

Figure 38. a) Scheme of the antenna configuration; **b)** Set-up of simultaneous UWB and MRI measurement.

In the MRI sequence, the one-dimensional 'pencil-like' imaging region is selected by the intersecting volume of two perpendicular slices (s. Fig. 39.a). Both slices are excited in short succession resulting in a saturation effect in the region of the intersection. When the experiment is repeated with a different delay time between both excitation pulses, the two images differ only in the strength of this saturation effect, and subtraction yields the desired 1D image. Placed through the heart in antero-posterior direction, this 'pencil' was scanned at a repetition frequency of 25.4 Hz. The motion components in both data sets, the 500 virtual UWB channels and the MR pencil, were once again separated by applying BSS decomposition.
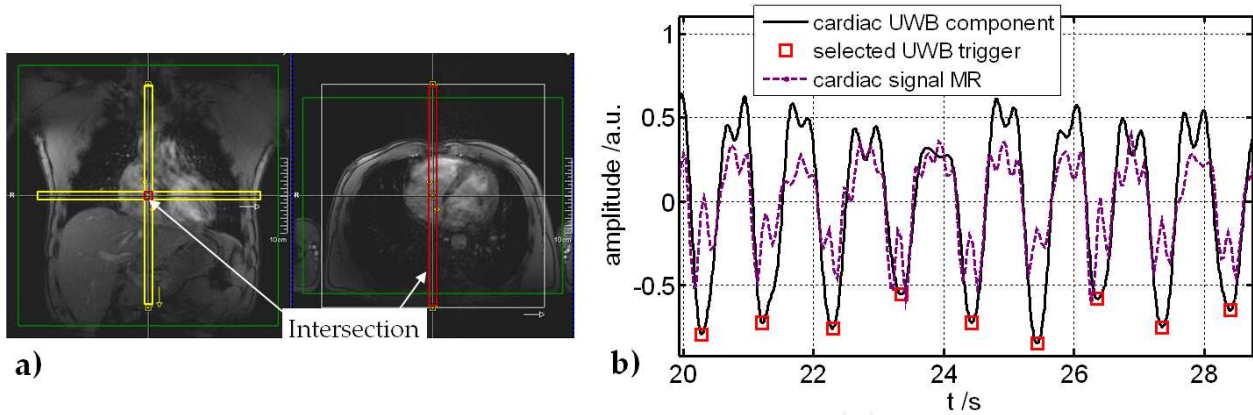
Figure 39. a) Selection of the 'pencil' by two crossing slices in antero-posterior direction through the heart; **b)** Detected cardiac motion component by UWB radar and MR "pencil".

The trigger events (squares in Fig. 39.b) in the UWB cardiac motion data - representing the point of maximum contraction of the myocardium - were determined by applying the algorithm proposed by us. This did not work with the cardiac components of the MR signal due to the pronounced double peaks in this data set. Comparing the cardiac components simultaneously gained by UWB and MR data, we observe perfectly matching slopes of both signals. However, in contrast to UWB radar the MR signal is affected by the blood velocity in the heart producing the double peaks. Keeping this in mind, we can conclude that both modalities render the same motion. Thus, we can assume the cardiac motion detection by UWB radar to be verified.

4.6. Advances for respiratory motions

To establish a UWB navigator for cardiac MRI in free-breathing mode, a landmark tracking of the heart due to the respiration motion is necessary [66]. The time-dependent UWB radar signal contains mainly respiratory motion of the chest, as in Fig. 32.b, which is not necessarily identical to the mechanical displacement of the heart. Therefore, we compared the UWB detected respiratory motion to simultaneously measured 1D MRI as described in Section 4.5.2. Resulting from that comparison, we extended the UWB configuration to allow for the detection of abdominal respiration, too (Fig. 40.a). The antenna configuration applied in the comparison made in Section 4.5.2 was extended by two additional channels above the chest and a second group with one *Tx* and one *Rx* antenna over the abdominal region.

In MR-based navigator techniques [67], the position of the diaphragm is monitored because the shift of the diaphragm is the dominant motion component of the heart due to respiration. The displacement of the diaphragm is mainly orientated in head-foot direction. Hence, the pencil-like one dimensional MRI was placed in head-foot direction across the heart. The UWB data of the first antenna group were decomposed by BSS for detection of breast respiration and cardiac cycle and the second group for the abdominal respiration. In the same way, the motion components were decomposed for "pencil-like" MRI.

The UWB detected breast respiration is not suitable to monitor the mechanical heart shift in head-foot direction. In Fig. 41, a delay between the breast respiration and the heart shift is

depicted, and especially in Fig. 41.b it becomes obvious that these are different processes. However, the UWB detected abdominal respiration correlates well with heart motion due to respiration. The correlation factor in measurement a) is 0.932 and 0.81 in measurement b).
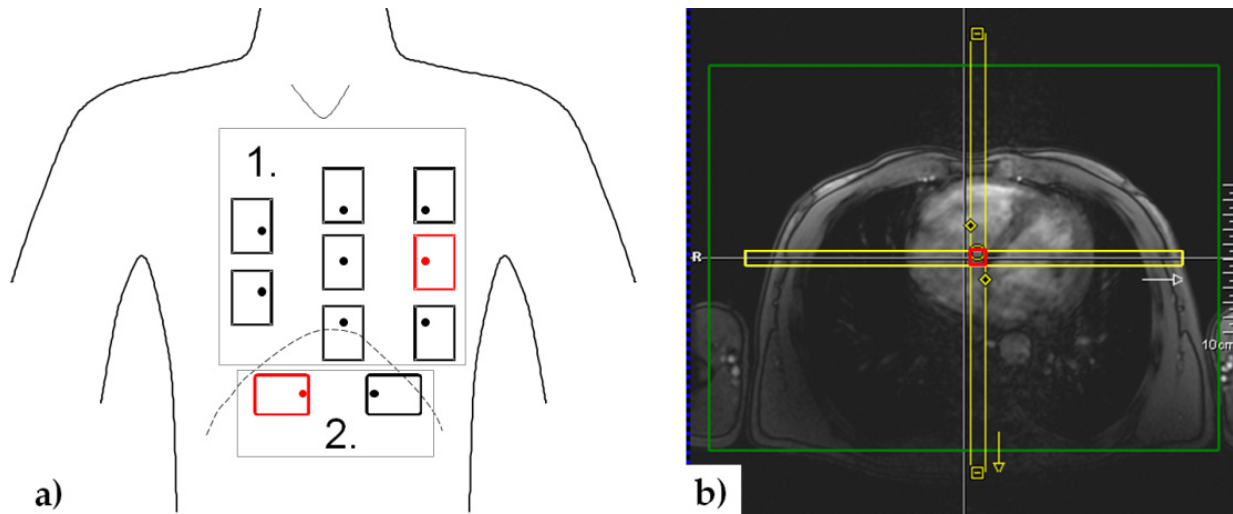

Figure 40. a) Extended antenna configuration with second group over the abdominal region; **b)** Placement of the two slices for the 'pencil-like' MRI (Head ⇔ Foot).
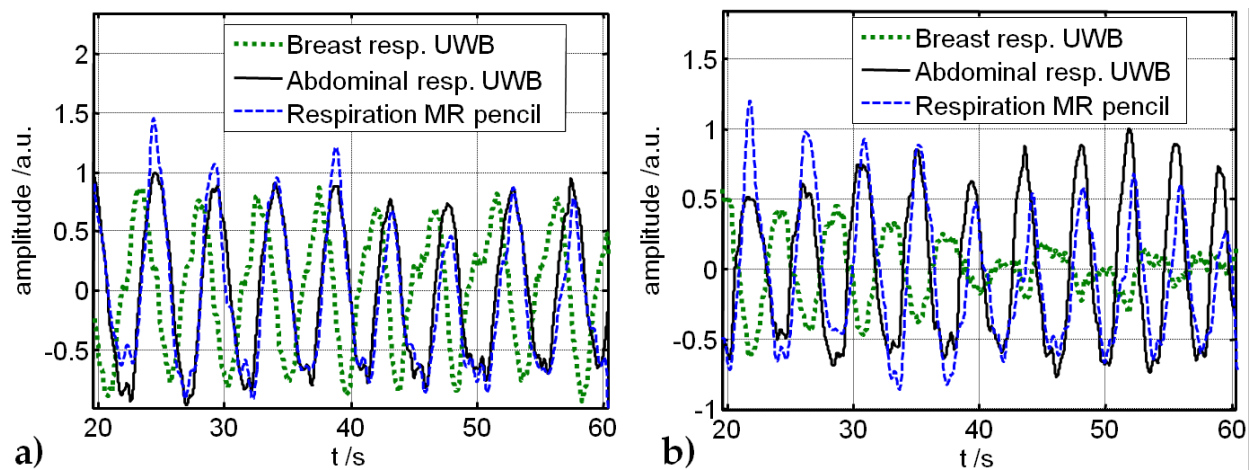

Figure 41. Breast and abdominal respiration by UWB radar and mechanical heart shift in head ⇔ foot direction monitored by MR pencil **a)** with changed breast and abdominal respiration **b)** with fading breast but changed abdominal component.

4.7. UWB triggered cardiac MRI

CMR and UWB signals were acquired simultaneously and synchronously to enable UWB triggering [81]. The UWB antennas were mounted in the same frontal position related to the subject as in Section 4.4.1. Simultaneous pulse oximetry (PO) was applied to compare our approach with another established triggering technique for cardiac MRI.

After acquiring a series of CMR images using a clinical sequence with conventional PO gating, we retrospectively reconstructed the *k*-space data a second time but now using trigger points derived from the simultaneously acquired UWB radar signals [81]. Figure 42.b

shows that both methods give virtually undistinguishable results, thus establishing the feasibility of CMR imaging utilizing non-contact UWB radar for triggering. In contrast to established techniques like ECG or PO, however, contact-less UWB-sensing provides cardiac and respiratory information simultaneously and, thus, a sequence-independent external navigator signal.
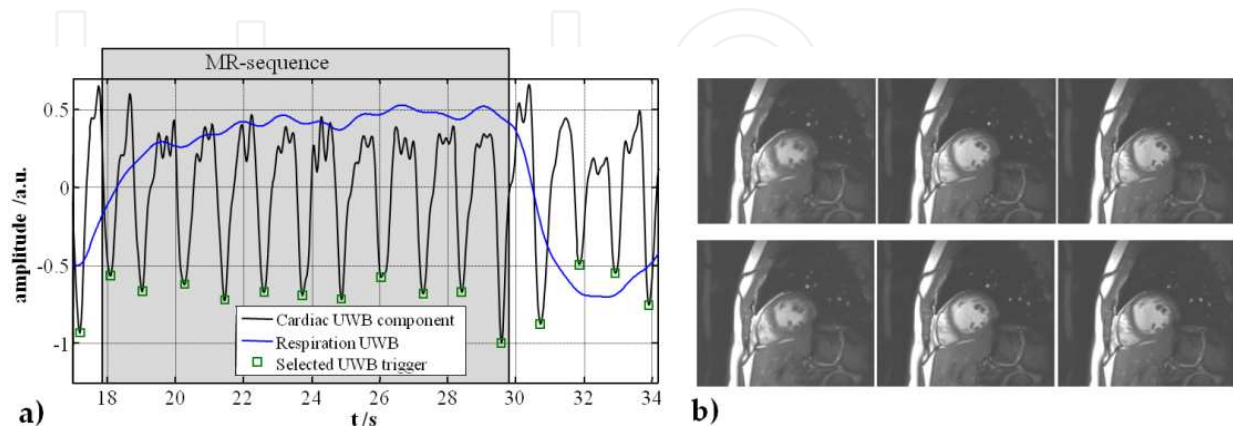

Figure 42. a) Cardiac UWB signal with selected trigger events; **b)** Top: Reconstructed images utilizing PO trigger, Bottom: Image reconstruction by UWB trigger events applied.

5. Microwave imaging in medicine

5.1. Introduction

Microwave ultra-wideband (UWB) sensing and imaging represents a promising alternative for the early-stage screening diagnostics of breast cancer. This perspective results from advantageous properties of microwaves: sensitivity of the dielectric properties of human tissue to physiological signatures of clinical interest in this frequency range, especially water content, their non-ionizing nature (compared to X-rays), and the potential of a cost-efficient imaging technology (compared to MRI) [82].

Numerous research groups have been working in this field since the end of the 1990s. Many studies deal with simulations, several groups perform phantom measurements, but only very few have already started some first clinical measurements. The challenges which have to be met concerning real *in vivo* measurements are multifaceted and depend on the conditions of the measurement scenario. The developed strategies and measurement principles of microwave breast imaging can be classified according to various characteristics: active vs. passive vs. heterogeneous microwave imaging systems [83]; microwave tomography (or spectroscopy) imaging [84] vs. UWB radar imaging [85]; examination in prone vs. supine position [83] and some further differentiations. This chapter deals exclusively with active microwave imaging based on the UWB radar principle which can be applied in general in both examination positions.

Figure 43 shows two basic antenna arrangements for the prone examination position. They differ in the antenna-skin distance.

Non-contact breast imaging: The most significant reason for non-contact breast measurements is the size of the antennas compared with the breast size. Thereby, it is impossible to mount a sufficient number of antennas on the breast surface in order to achieve an adequate image quality. The displacement of the antennas from the breast increases the area where additional antennas can be localized. Besides that, it allows mechanical scanning where the antennas can be rotated around the breast in order to create a synthetic aperture. On the other hand, this non-contact strategy is accompanied by a lot of other problems and challenges.
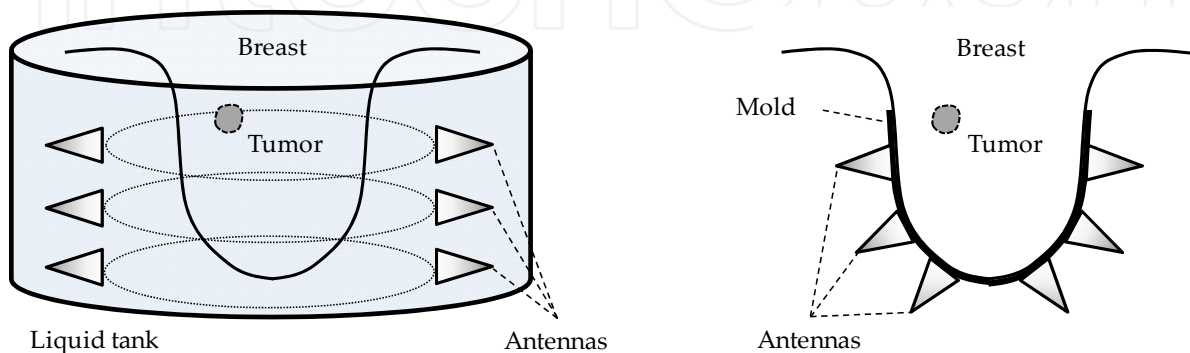

Figure 43. Schematization of non-contact breast imaging using a liquid contact medium (left side) and contact-based breast imaging (right side) in the prone examination position

Depending on the dielectric contrast between the medium surrounding the antennas and the breast tissue, only a fraction of the radiated signal energy will penetrate the breast. The major part will be reflected at the breast surface. It provides clutter which has to be eliminated since it perturbs the signals of interest. In order to reduce the reflection coefficient, several approaches use a liquid coupling medium in which the breast has to be immersed and in which the antennas can surround the breast. The same energy reduction effect appears for reflected components from inside of the breast passing the dielectric boundary in the opposite direction. Furthermore, in the opposite direction (from dielectric dense medium into a less dense medium) waves can only leave the breast below the angle of total reflection which implies an additional reduction of the detectable signal energy outside the breast.

The individual breast shape plays an important role in connection with these effects as well as for image processing. In section 5.3, we describe a method for breast and whole body surface reconstruction based on the reflected UWB signals.

Contact-mode breast imaging: Contact-based breast imaging avoids the disadvantages described above. The antennas are localized directly at the breast surface. Understandably, they have to be small enough in order to arrange a sufficient number of antennas around the breast. The corresponding number of signal channels will be obtained by electronic scanning, that means sequential feeding of all transmitter antennas with simultaneous signal acquisition of all receiving antennas. This strategy involves the problem of individual breast shapes and sizes which influences the contact pressure of the breast skin onto the antenna aperture and, thus, the signal quality [86].

However, we prefer this measurement scenario for our current investigations, and intend to weaken the contact problem in the future by 2 or 3 different array sizes and an additional gentle suction of the breast into the antenna array by a slight underpressure. In section 5.4, we present an experimental measuring set-up where we pursue a strategy of nearly direct contact imaging in order to conjoin the advantages of contact-based imaging with the possibility of mechanical scanning.

5.2. Breast and body phantoms

In the context of UWB tissue sensing, the water content plays a key role as it determines the inherent dielectric properties (ε' and ε'') [43]. Moreover, the water content is known to vary among the different human tissues as well as between specific normal and pathologic ones, thus offering a potentially broad spectrum of UWB applications for biomedical diagnostics.

Oil-in-gelatin phantoms, mimicking the dielectric properties of human tissues, were manufactured according to a protocol from [24]. The water concentration varied between 19 and 95% (v/v; ~ 10% water graduation steps), to obtain a set of materials with different permittivity values (ε' ranging from 8 to 59 and ε'' ranging from 0.5 to 11, both averaged over frequencies from 1 to 4 GHz). The measurements were carried out by means of the M-sequence devices [76], [87] with HaLoS chipsets and a frequency bandwidth of 4.5 GHz, as well as the radar data acquisition and analysis software "ultraANALYSER" developed for this purpose.

The variation of the oil-water-concentration led to the identification of distinct permittivity values ε' (Fig. 44, insert) of the different oil-in-gelatin phantoms. The phantom, which was manufactured without oil (95% water), showed values between 53 and 59 for the real part ε' and between 11 and 10 for the imaginary part ε'' of the permittivity in the frequency range between 1 and 3.5 GHz (Fig. 44, insert). The results for pure distilled water are also displayed. The real part of permittivity agrees well with literature data [88].
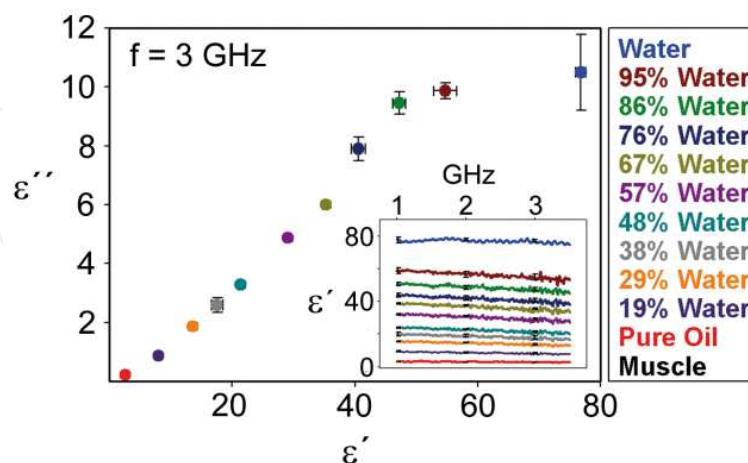

Figure 44. Dielectric properties of nine oil-in-gelatin phantoms with varying percentage of water (from 19% to 95% water (v/v)) and porcine muscle tissue. Depicted is the correlation of the real part ε' and the imaginary part ε'' of the phantoms. Both parts increase with an increasing water-concentration. Error bars represent the standard deviation from an average of three individual measurements on the phantom surface (insert).

5.3. Breast and body surface reconstruction

5.3.1. Method

The benefits of the exact knowledge of the breast surface for non-contact microwave breast imaging are manifold and can improve the results significantly. The inclusion of the breast shape information is essential to calculate the wave traveling path in order to image the interior of the breast based on radar beam-forming techniques. Some approaches use the surface information for initial estimations. Other non-contact measurement approaches strive to illuminate the breast from a specific distance which requires a very fast online surface identification in order to adapt the antenna position during measurement. Furthermore, in the case of varying distances between antenna and breast, the exact knowledge of the breast surface can improve the estimation of the skin reflection component for a better early time artifact removal. In order to reduce the calculation time, the region of interest (i.e. the region for which the image has to be processed) can be restricted based on known surface geometry [89], [90].

Additionally to the significance for breast imaging, UWB microwave radar is suitable for whole body surface reconstruction which can be used in other medical microwave applications as well as in safety-relevant tasks, e.g. under-dress weapon detection.

The Boundary Scattering Transform (BST) represents a powerful approach for surface detection problems. BST and its inverse transform (IBST) were introduced 2004 by Sakamoto and Sato [91] as basic algorithms for high-speed ultra wideband imaging, called SEABED (Shape Estimation Algorithm based on BST and Extraction of Directly scattered waves). Since then, this idea has been extended from mono-static 2D-imaging to the point of bi-static 3D-imaging (IBBST) [92]. The SEABED algorithm represents a high–speed, high-resolution microwave imaging procedure. It does not include the entire radar signal; it uses only wave fronts instead. Furthermore, changes (derivatives) of the propagation time (transmitter → object surface → receiver) depending on the antenna position during the scan process play an important role. SEABED consists of three steps: 1. Detection of the wave fronts and calculation of their derivatives with respect to the coordinates of the scan plane. 2. Inverse Boundary Scattering Transform, which yields spatially distributed points representing the surface of the object. 3. Reconstruction of the surface based on these points.

The practical applicability of the original algorithm to the identification of complex shaped surfaces is limited because of the inherent planar scanning scheme and, therefore, the disadvantage of illuminating only one side of the object. For this reason, we extended the bi-static approach of [92] toward non-planar scanning and a fully three-dimensional antenna movement based on the idea that in the case of arbitrary non-planar scan schemes the current scan plane can be approximated by the tangential plane at each antenna position [93]. An antenna position dependent coordinate transform which ensures that the antenna axis is parallel to the x-axis and the current scan plane is parallel to one plane of the coordinate system allows the application of the IBBST for nearly arbitrary scan surfaces. More precisely, this generalized approach is limited to scenarios where the antennas will be

moved orthogonally or parallel to the antenna axis, which is fulfilled in most practical cases. First results of breast shape identification were published in [94], [95].

Based on the following transform equation, the coordinate of the specular point can be calculated

$$
\begin{aligned}
\bar{x} &= \bar{X} - \frac{2D^3 D_{\bar{X}}}{D^2 - d^2 + \sqrt{(D^2 - d^2)^2 + 4d^2 D^2 D_{\bar{X}}^2}} \\
\bar{y} &= \bar{Y} + \frac{D_{\bar{Y}}}{D^3}\left(d^2(\bar{x} - \bar{X})^2 - D^4\right) \\
\bar{z} &= \bar{Z} + \sqrt{D^2 - d^2 - (\bar{y} - \bar{Y})^2 - \frac{(D^2 - d^2)(\bar{x} - \bar{X})^2}{D^2}}
\end{aligned}
\tag{5}
$$

where $\bar{x}, \bar{y}, \bar{z}$ are the coordinates of the reflective surface point (specular point), $\bar{X}, \bar{Y}, \bar{Z}$ are the coordinates of the center between the two antennas, D is the half distance transmitter → reflection point → receiver, d is the half distance between the two antennas, and $D_{\bar{X}} = \frac{dD}{d\bar{X}}$, $D_{\bar{Y}} = \frac{dD}{d\bar{Y}}$ symbolizes the derivatives of the distance with respect to the denoted direction of antenna movement. The bars above the symbols mark the coordinates of the transformed coordinate system [93].
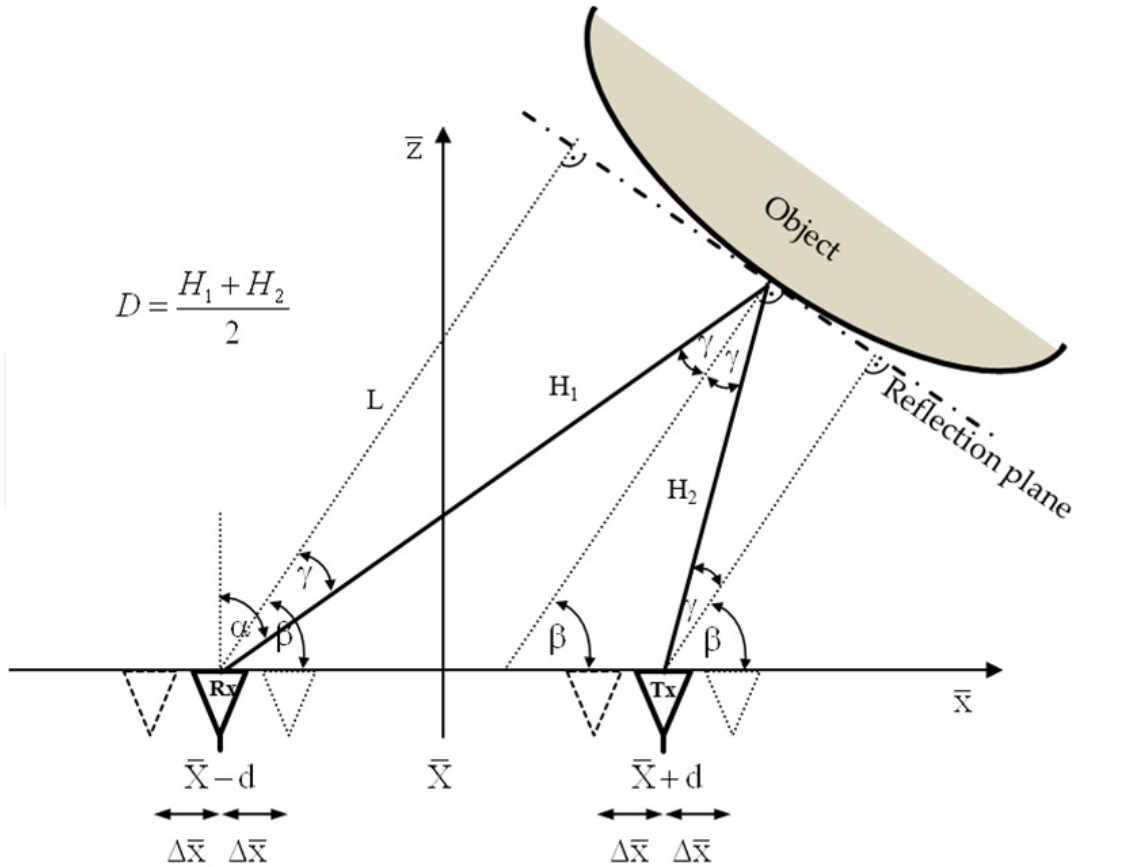

Figure 45. Ray geometry of the inverse bi-static boundary scattering transform (IBBST)

The main challenge is the exact detection of the wave fronts and their proper derivative. For the purpose of wave front detection, we use an iterative correlation-based detection algorithm similar to [96]. In this connection, a short antenna impulse response over a sufficiently wide angular range plays an important role. The difficulties of obtaining appropriate wave front derivatives result from the three-dimensional nature of the problem. The antennas are moved and the transmitted waves are reflected in the three-dimensional space. Especially in the case of wave front crossing and impulse overlapping as well as sparsely detected wave fronts, it is very complicated to recognize which identified wave front at one scan position is related to which wave front at the previous scan position and vice versa. So, it may happen that derivative values are wrongly calculated, which can lead to a spatially false projection of the surface points. In order to avoid such errors, we establish thresholds of feasible derivative values dependent on the antenna beam width.

5.3.2. Detection and elimination of improper wavefronts

General limit values: The range of values of the distance derivatives $D_{\bar{X},\bar{Y}}$ is theoretically bounded between 0 and 1 depending on the slope of the reflection plane (tangent plane of the object surface at the specular point). In the case of parallelism between reflection plane and antenna axis, $D_{\bar{X}} = 0$, whereas in the case of orthogonality, $D_{\bar{X}} = \pm 1$. Thus, calculated values $|D_{\bar{X}}| > 1$ are definitely caused by incorrect wave front detection. Consideration of these general boundaries and exclusion of wave fronts exceeding them yields a significant improvement.

Customized plausibility limit values: The boundary $D_{\bar{X}} = \pm 1$ assumes an antenna radiation angle of 90° or more, which is not given using directive radiators, e.g. horn antennas. In that case, the range of plausible derivative values can further be restricted. Assuming a maximum antenna radiation angle α and a distance between transmitter and receiving antenna of $2d$ the minimum reasonable value $D_{\min}$ can easily be defined by

$$D_{\min} = \frac{d}{\sin \alpha} \tag{6}$$

Wave fronts with lower D values would imply specular points which are located outside the antenna beam and, therefore, can be ignored [98].

Furthermore, a maximum distance derivative $D_{\bar{X}}$ depending on α, d and D can be established:

$$D_{\bar{X}\max} = \frac{\sqrt{\left(L + \cos\beta \cdot \vartriangle x\right)^2 - \left(L + \cos\beta \cdot \vartriangle x\right)\cos\beta \cdot 2d + d^2} - \sqrt{\left(L - \cos\beta \cdot \vartriangle x\right)^2 - \left(L - \cos\beta \cdot \vartriangle x\right)\cos\beta \cdot 2d + d^2}}{2 \cdot \vartriangle x} \tag{7}$$

with the perpendicular from the reflection plane to the distant antenna $L = \cos\gamma \cdot \dfrac{\left(D^2 - d^2\right)}{D - d\sin\alpha}$, its perpendicular angle β and the reflection angle γ as depicted in Fig. 45. This value yields

$D_{\bar{X}\,\mathrm{max}} = \sin\alpha$ for mono-static arrangements $(d = 0)$ and approaches to this value in the case of $L \gg d$, respectively. For further details of the derivation of these thresholds and reconstruction examples illustrating the accuracy enhancement due to the application of these thresholds, we refer to [98].

5.3.3. Reconstruction results

For repeatable measurements, we applied a female dressmaker torso which is filled with tissue-equivalent phantom material (Fig. 46). Based on linear and rotational scanners which can move or rotate the object and/or the antennas, several non-planar scan schemes can be realized in order to scan this torso efficiently. In the following, the results of breast shape identification based on a toroidal scan will be shown. The M-sequence radar device used has a bandwidth of 12 GHz [97].
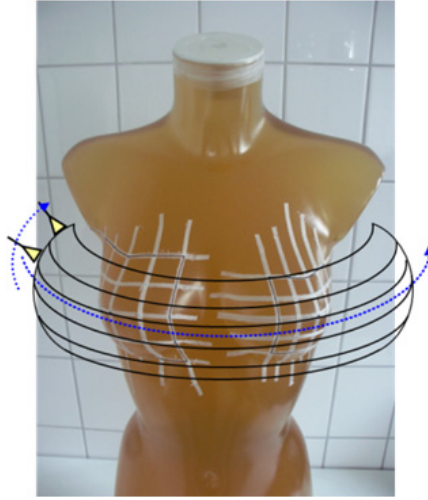

Figure 46. Female torso filled with human tissue mimicking phantom material and delineation of the toroidal scan scheme to reconstruct the chest surface

Numerical problems may arise in the calculation of derivatives from discrete data (discrete time intervals; discrete antenna positions in the space) which have to be considered for setting measurement and processing parameters. The resolutions of spatial scanning and radar signal sampling have to be harmonized carefully with each other in order to avoid derivative artifacts. The maximum possible error of the derivative is $\hat{e}(D_{\bar{x}}) = \dfrac{\triangle t \cdot v_0}{2\triangle x}$ where $\triangle t$ is the time resolution of the wave front detection, $\triangle x$ is the antenna displacement applied for the calculation of $D_{\bar{x}}$ and v_0 is the propagation velocity of the electromagnetic wave. Hence, it will be obvious to meet the requirement of for example $\hat{e}(D_{\bar{x}}) \leq 0.05$ (0.05 is more than 5 percent relative error with respect to $D_{\bar{x}\,\mathrm{max}}$ for antenna beam widths < 90°!) with an antenna displacement such as $\triangle x = 2.5\,\mathrm{cm}$ in air $(v_0 = c_0)$ the wave front detection has to be realized with a time accuracy of 8.33 ps which has to be provided by interpolation within the wave front detection algorithm. Higher performance requirements presuppose

an even more precise wave front identification. Naturally, this is only possible if the radar device fulfills such high time stability requirements.

Figure 47 shows the UWB reconstruction results of the mentioned torso in comparison to a laser reference measurement. In order to quantify the accuracy, the distances between each calculated UWB surface point and the laser-based detected surface is calculated. The resulting mean aberration lower than 1.4 mm underlines the potential of this method. Nevertheless, it is obvious that a further enhancement of the wave front detection represents a residual challenge in order to fill in increasingly the areas of sparsely distributed surface points.
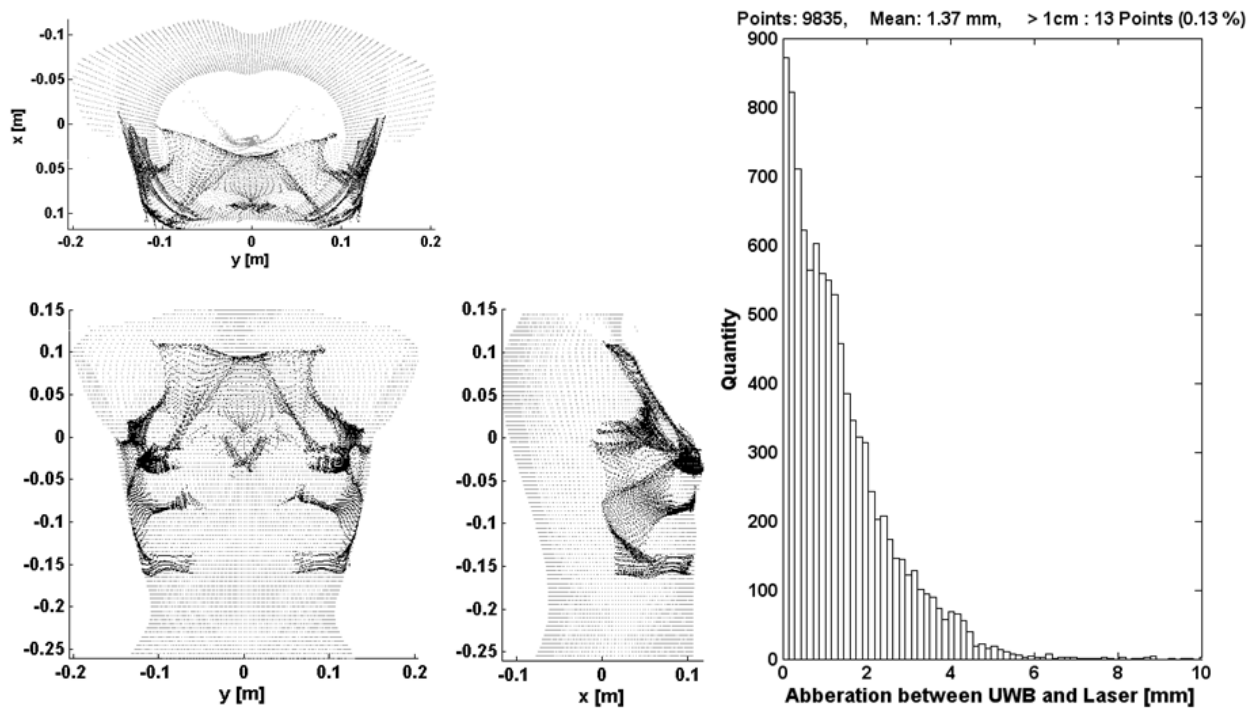

Figure 47. Exact UWB chest surface reconstruction (black) and appraisal of performance values by means of a laser reference measurement (gray) showing a mean aberration lower than 1.4 mm.

Furthermore, the applicability of a 3D-IBBST-based UWB surface reconstruction method for medical applications other than breast imaging as well as for security scenarios (under dress weapon detection) is demonstrated in [98].

5.4. Contact based breast imaging

5.4.1. UWB breast imaging in time domain

The main parts of UWB time domain imaging are the removal of clutter (also referred to as early time artifact removal) and beam-forming (also referred to as migration or back projection). Because the tumor reflections are overlapped by antenna cross-talk and skin reflection, clutter removal is a very important and critical component of signal

preprocessing before beam-forming can be carried out. Most clutter removal approaches assume that the clutter appears very similar in each channel and, thus, its estimation improves with increasing channel number. It must be noted that this holds only for channels with comparable clutter parameters. That means clutter estimation and removal has to be done separately for groups consisting of only associated signals (channels with identical antenna distances and boresight angles Tx-Rx), which accomplishes this task. In scientific work on simulation, this circumstance is commonly ignored. For practical applications, however, it has to be taken into consideration.

The simplest approach is to estimate the clutter by means of the average value. Tumor reflections are assumed to appear uncorrelated in the channels and to be negligible in the averaged signal. Even though publications about advanced clutter removal algorithms emphasize the weak points of this self-evident approach, it must be noted that it works relatively robustly in the case of covering tumor response by clutter when some of the proposed alternatives are not applicable.

Image formation algorithms using time domain beam-forming can be included in the following generalized formula:

$$I(\mathbf{r}_0) = \sum_{\tau_h=-T_h/2}^{T_h/2} h(\tau_h, \mathbf{r}_0) \cdot \left(\sum_{n=1}^{N} \sum_{\tau_W=-T_w/2}^{T_w/2} w_n(\tau_w, \mathbf{r}_0) \cdot S_n(t + \tau_n(\mathbf{r}_0) + \tau_w + \tau_h) \right)^2 \qquad (8)$$

where N is the number of channels, $S_n(t)$ is the clutter subtracted signal of channel n, $\mathbf{r}_0$ symbolizes the coordinates of the focal point (image position vector), $\tau_n(\mathbf{r}_0)$ is the time delay of channel n related to the focal point at $\mathbf{r}_0$ and $I(\mathbf{r}_0)$ is the back scattered energy which has to be mapped over the region of interest inside the breast. Based on two FIR filters, the different extensions of the common delay-and-sum beam former can be expressed. Path-dependent dispersion and attenuation [99], [100] can be equalized by means of $w_n(\tau_w, \mathbf{r}_0)$ which – in the simplest case - can be only a weight coefficient. Other improvements can also be included by convolution in the time domain, e.g. the cross-correlated back projection algorithm [101]. $h(\tau_h, \mathbf{r}_0)$ represents a smoothing window at the energy level or a scalar weight coefficient [102].

5.4.2. Measurement setup based on small antennas

The efficient penetration of the electromagnetic waves into the tissue and the spatial high-resolution registration of the reflected signals are crucial tasks of the antenna array design. In this regard, efficiency is not only a matter of radiation efficiency or antenna return loss, respectively. An efficient antenna array design concerning biomedical UWB imaging purposes comprises also the shape and duration of signal impulses, angle dependence of the impulse characteristics (fidelity), and the physical dimensions of the antenna. These interacting parameters are hardly to accommodate to each other within one antenna design. Generally, compromise solutions have to be found considering basic conditions of scanning,

tissue properties and image processing. Here, we pursue the objective of very small antenna dimensions, short impulses and an application in direct or quasi direct contact mode. Therefore, we investigated the usability of small interfacial dipoles.
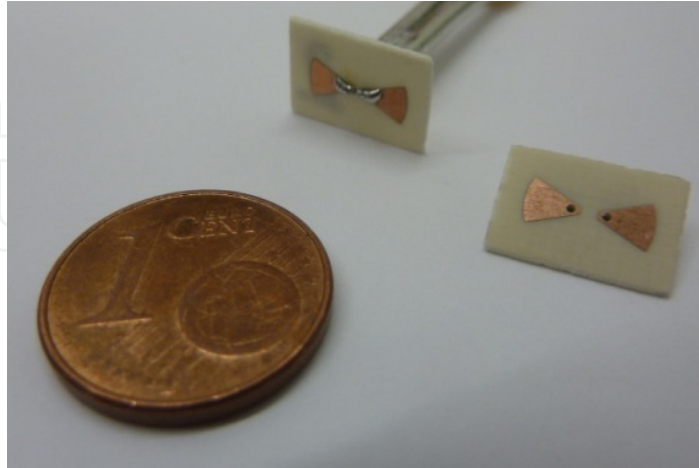

Figure 48. Small bow-ties on Rogers substrate

Initially, we used short bow-ties (Fig. 48) with the dimensions of 8 mm x 3 mm implemented on Rogers® 4003 substrate (0.5 mm) using PCB technology. Dipoles have to be fed differentially. The balanced feeding is realized by differential amplifier circuits [103].

These antennas cannot be matched over a large bandwidth, which leads to unwanted reflections between antenna and amplifier. There are two options concerning the handling of this problem: realization of a sufficient line length between antenna and amplifier (in order to gate out the reflections) or implementation of the amplifier circuits directly at the antenna feed point. On an interim basis, we pursued the first strategy using long cables between antenna and amplifier. Assuming a maximum mean tissue permittivity $\varepsilon' \leq 50$, a 70 cm cable will ensure that any reflections from inside of the breast (diameter ~ 10 cm) and unwanted reflections at the amplifier do not overlap.

As mentioned above, the contact between antennas and breast skin represents a crucial aspect for sufficient signal quality. Regarding clinical requirements (e.g. disinfection) we plan to place the antennas behind a thin examination mold. But this additional interface reduces the signal quality significantly. Therefore, a thin (~2 mm) matching layer consisting of tissue mimicking phantom material was inserted between the examination mold and the antennas in order to increase the signal energy penetrating the tissue and reduce the backward radiation (Fig. 49). The benefit achieved when using a thin contact layer was also investigated and verified by simulations (Fig. 5 in section 2.3.2).

We built up two preliminary array set-ups for phantom measurements, both including eight antennas and distributing them around a circular segment (diameter 9.5 cm) in steps of 22.5°. An array with a horizontal antenna arrangement is shown in Fig. 50. Exemplary phantom measurement results achieved with these prototypes are published in [104] and [105] and will be summarized in section 5.4.3.
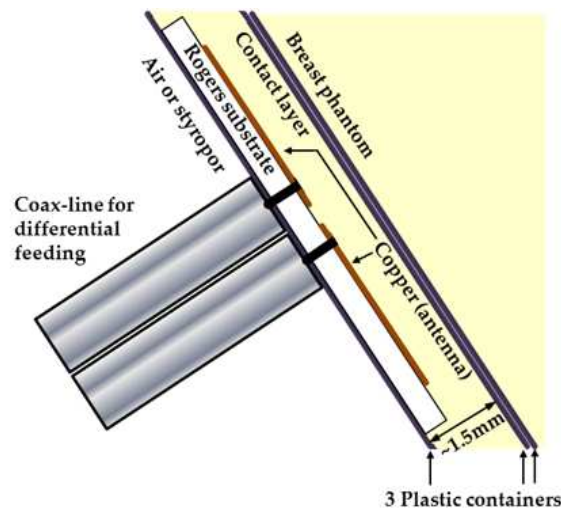
Figure 49. Schematic illustration of the contact layer filled with phantom material and mounted antennas inside

Figure 50. Antenna array: Assembly stage before casting the contact layer. The connected and affixed differential fed antennas and the container for the outer boundary of the contact layer are still visible (left panel). Finished antenna array with inserted rotatable breast phantom (right panel)

After this preliminary development stage, the differential feeding amplifier was relocated into the antenna feed point. By this step, reflections due to antenna mismatch will be avoided, and the quantity of feeding cables will be bisected, because each active antenna element can be fed single-ended (Fig. 51).

In conjunction with this enhancement, the mechanical part of the antenna array was improved. A developed slide-in mounting system (Fig. 51) allows flexible antenna application and replacement and, therefore, facilitates investigations of various Rx-Tx-arrangements without destruction and rebuild of the whole array as it is the case with the preliminary set-up shown in Fig. 50 [106].

Because the contact layer will not be hermetically sealed in this case, the chemical instable oil-gelatin phantom material cannot be used anymore for this task. Thus, investigations of alternative materials have to be considered. We propose polymer-powder composites where

dielectric powders (e.g. carbon meal or barium titanate powder) will be admixed to silicone rubber. This special challenging topic is currently under investigation.
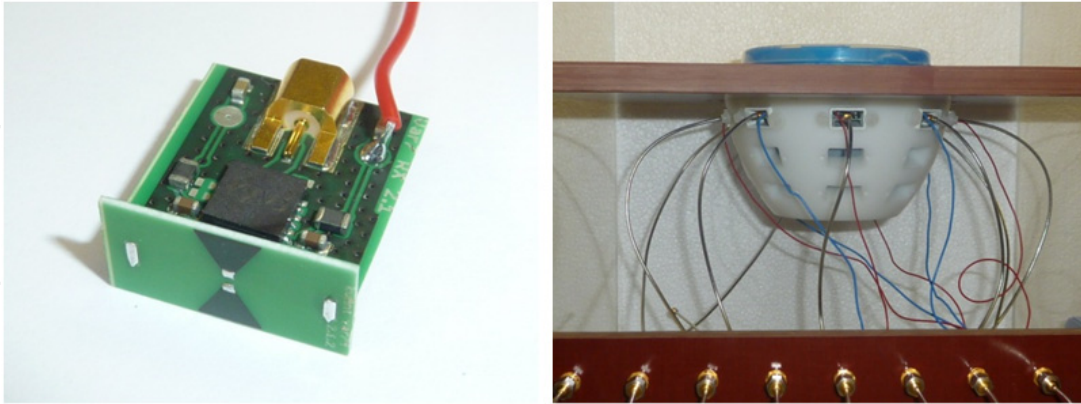

Figure 51. Photographs of an active antenna element (Rx) with 8 mm dipole with amplifier circuit board (left panel) and the slide-on mounting system for phantom measurements as well as *in vivo* measurements

5.4.3. Imaging results of phantom trials

The breast phantoms are tissue mimicking oil-gelatin phantoms according to [24] and described in section 5.2, where the dielectric properties can be adjusted by means of the oil content. For our measurements we used two types of material: 40% oil (57% water) content material mimics healthy tissue which approximately corresponds to group II of adipose-defined tissue (31%-84% adipose tissue) [106]. The 10% oil (85.5% water) content material simulates tumor tissue. Fig. 52 illustrates permittivity, attenuation losses and reflection coefficient between both tissues. In order to realize an optimal contact to the antenna array, the phantom material is filled in identical plastic containers (diameter 9.5cm) as used for the examination mold. The containers are hermetically sealed and stored in the fridge to avoid chemical instability of the phantom material. The phantoms have to be acclimatized at least 3 hours before starting the measurements.
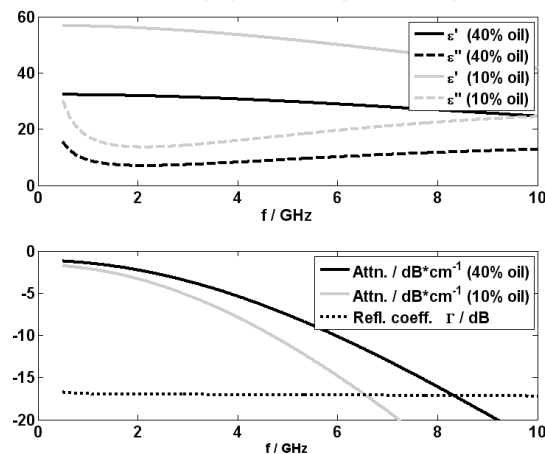

Figure 52. Dielectric values of the tissue mimicking phantom material: Permittivity (above), transmission losses per cm and reflection coefficient between them (below)

Figure 53 shows two measured signals of the proposed antennas which illustrate the appropriate time domain characteristics. The measurement through 6 cm tissue (mimicked by means of phantom material) as well as the cross-talk signal between two antennas show relatively short impulse shapes with low ringing, which is essential for UWB imaging. Including the dispersive tissue impact the spectral bulk ranges between 1 GHz and 3 GHz with a bandwidth greater than 2 GHz for both received impulses. Obviously, because of the dielectric scaling due to the direct contact between tissue and antenna, such small antennas are capable of radiating waves in a frequency range with acceptable attenuation and penetration depth.
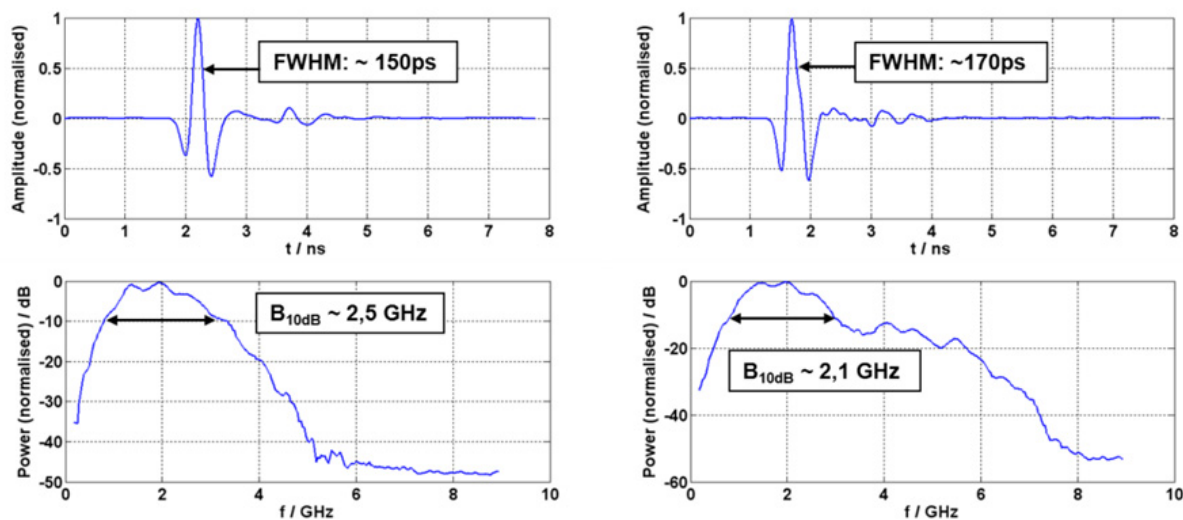

Figure 53. Measurement signals based on the described bow-ties: measurement through 6 cm tissue mimicking phantom material with 40% oil content (left panel) and cross-talk signal between adjacent antennas, separated by 2.5 cm (right panel)

During the phantom measurements, four antennas acted as receivers and are permanently connected with Rx1…Rx4 of the radar device. The transmitter signal was connected to one of 4 transmitter antennas by a coaxial switch matrix. Thus, 16 signal channels could be achieved without rearrangement. Their angles between the boresight directions of Tx and Rx differed in the range 22.5 - 157.5°. Because this amount of signal channels is insufficient for high-resolution imaging, we had to consider robust and reproducible mechanical scanning to achieve a sufficient number of channels. In order to simulate antenna rotation, the phantoms were rotated in steps of 11.25°. This resulted in 512 signals (16 channels x 32 rotations) which could be included into the imaging process of one phantom.

Figure 54 shows exemplary imaging results of the described breast phantoms applying the presented measuring set-up and time domain beam-forming. Despite the relatively low dielectric contrast between both tissue simulations, the tumor inclusions can clearly be identified. The highest interferences (side lobes) are about 11dB (15mm tumor) and around 7dB (10mm tumor) lower than the tumor representation. Additionally, the lower panels of Fig. 54 illustrate the capability of localization and differentiation between multiple tumors, for example two 15 mm tumors with a distance of 30 mm between them. Despite of the

relatively low dielectric contrast between healthy and cancerous tissue mimicking phantom material, the tumors can be detected and separated.

The results underline that small dipoles can be profitably applied for UWB breast imaging. The impressive identification of the tumor surrogates promises also the detection of weaker dielectric contrasts. On the other hand, it must be noted that the tumor surrounding tissue imitation is completely homogeneous which does not correspond to reality. Therefore, our breast phantoms must be enhanced in the future toward a better approximation of the breast tissue heterogeneity.
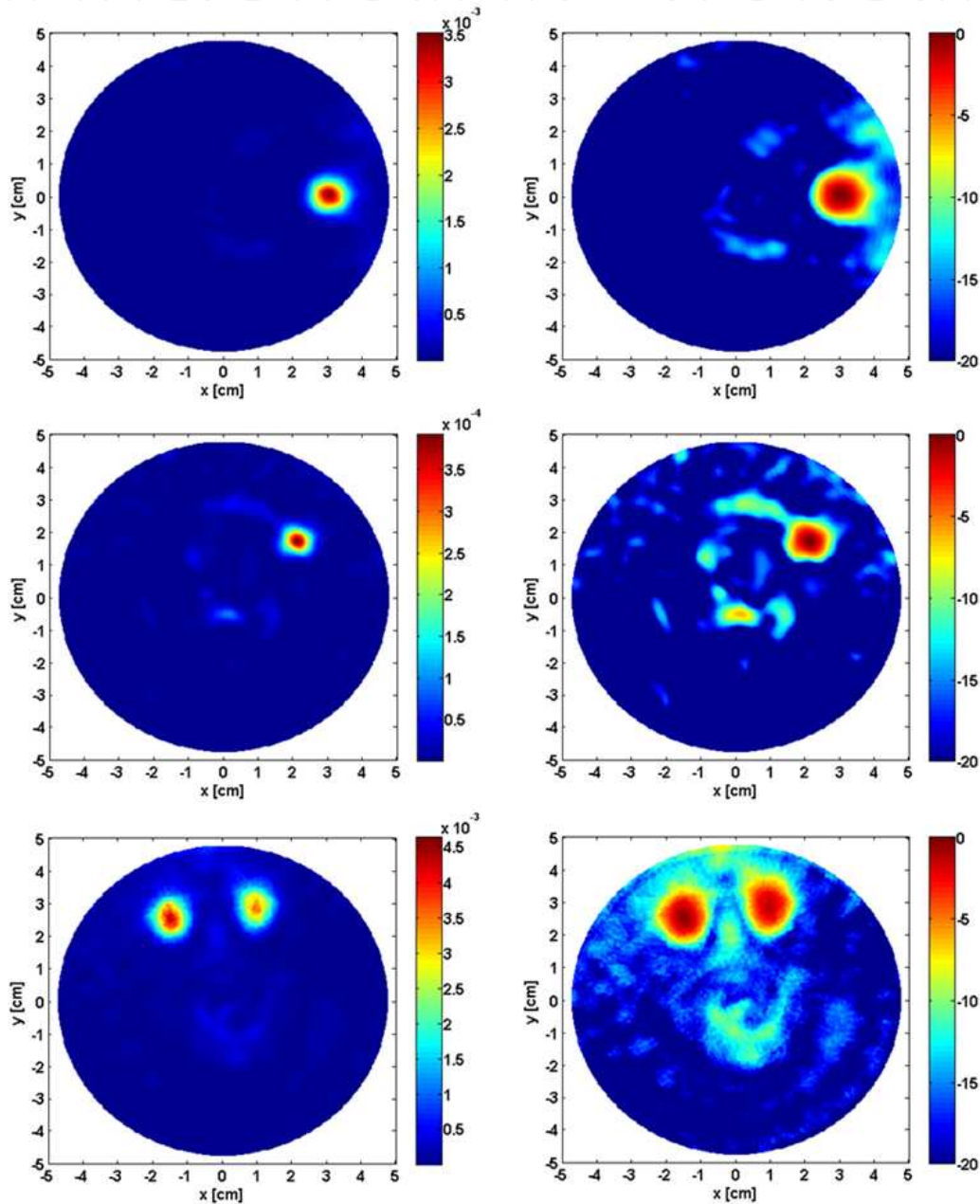
Figure 54. UWB images of phantom trials including a 15mm (top) and a 10 mm (middle) tumor surrogate as well as two 15 mm tumor surrogates, separated by 30 mm (below). Left: linear energy scale; Right: logarithmic scale in dB.

6. Conclusions

In this chapter, we dealt with ultra wideband sensing in medical engineering, i.e. using electromagnetic waves of large bandwidth for probing the human body and biological tissue. Sufficient penetration of the human body combined with antennas of manageable size were our major concern. Also, the frequency band from 1 GHz to 5…8 GHz turned out to be best suited for our purposes. By using active or dielectrically scaled antennas for this frequency range, they can be built sufficiently small. Wave propagation at these frequencies is mostly influenced by water, the most abundant component of biological tissue. The effect of salt becomes less detrimental above 1 GHz. Above 5…8 GHz, however, water absorption will drastically increase the propagation losses. The given frequency band also provides acceptable resolution for microwave imaging and ample micro-Doppler sensitivity.

For experimental investigations, we exploited ultra-wideband pseudo-noise devices. They provide probing signals of very low power, thus avoiding damages to biological tissue. Furthermore, they provide sufficient dynamic range, measurement speed and short term stability for super resolution techniques of microwave imaging and weak-motion tracking.

We demonstrated medical applications of ultra-wideband sensing by three distinctive examples, each standing for a specific class of applications.

1. Contact-based measurements (impedance spectroscopy) aimed to estimate tissue permittivity. This mainly gives some hints on water concentration and water bonds. At lower frequencies, other molecules will also leave their traces in the measured impedance value.

2. Remote motion tracking of organs inside the human body like cardio-pulmonary activity for example of motion correction for magnetic resonance imaging. Remote vital sign detection is a related topic with relaxed conditions referred to tracking precision but increased requirements with respect to area coverage. The analysis of cardiac mechanics for separate heart region accessible by stand-alone UWB radar or in conjunction with the electrical activity from the ECG contains valuable diagnostic information, e.g. for infarction detection, as ischemic tissue shows a modified contraction pattern.

Remote or contact-based microwave imaging of inner organs or malignant tissue, for example the detection of breast tumors.

Author details

Ingrid Hilger, Katja Dahlke, Gabriella Rimkus and Christiane Geyer
Jena University Hospital, Germany

Frank Seifert, Olaf Kosch, Florian Thiel
Physikalisch-Technische Bundesanstalt Berlin, Germany

Matthias Hein, Francesco Scotto di Clemente, Ulrich Schwarz, Marko Helbig, Jürgen Sachs
Ilmenau University of Technology, Germany

Acknowledgement

7. References

[1] U. Pliquett, "Electricity and biology," in 11th International Biennial Baltic Electronics Conference, BEC 2008, pp. 11-20.

[2] K. Nowak, W. Gross, K. Nicksch *et al.*, "Intraoperative lung edema monitoring by microwave reflectometry," *Interactive Cardiovascular and Thoracic Surgery*, pp. 540-544, 2011.

[3] J. Sachs, E. Zaikov, M. Helbig *et al.*, "Trapped Victim Detection by Pseudo-Noise Radar," in 2011 International Conference on Wireless Technologies for Humanitarian Relief (ACWR 2011) Amritapuri, Kollam, Kerala, India, 2011, pp. 265-272.

[4] E. Zaikov, and J. Sachs, "UWB radar for detection and localization of trapped people," *Ultra Wideband*, B. Lembrikov, ed., Rijeka, Croatia: Scivo, 2010.

[5] J. Sachs, M. Helbig, R. Herrmann *et al.*, "Merkmalsextraktion und semantische Integration von Ultrabreitband-Sensoren zur Erkennung von Notfällen," in 3. Deutscher AAL-Kongress 2010 Assistenzsysteme im Dienste des Menschen, Berlin, 2010.

[6] R. Herrmann, J. Sachs, and F. Bonitz, "On benefits and challenges of person localization using ultra-wideband sensors," in Indoor Positioning and Indoor Navigation (IPIN), 2010 International Conference on, 2010, pp. 1-7.

[7] R. Herrmann, J. Sachs, K. Schilling *et al.*, "12-GHz Bandwidth M-Sequence Radar for Crack Detection and High Resolution Imaging," in International Conference on Ground Penetrating Radar (GPR), Birmingham, UK, 2008.

[8] R. Herrmann, "M-sequence based ultra-wideband radar and its application to crack detection in salt mines" PhD-Thesis, Faculty of Electrical Engineering and Information Technology, Ilmenau University of Technology (Germany), Ilmenau, 2011.

[9] J. Sachs, "Ultra-Wideband Short-Range Sensing - Theory, Sensors, Applications", Berlin: Wiley-VCH, 2012.

[10] M. A. Hein, C. Geyer, M. Helbig *et al.*, "Antennas for ultra-wideband medical sensor systems," in 3rd European Conference on Antennas and Propagation, EuCAP 2009, 2009, pp. 1868-1872.

[11] R.C. Hansen, "Fundamental Limitations in Antennas", in Proc. of the IEEE, vol. 69, n. 2, pp. 170-182, Feb. 1981

[12] U. Schwarz, M. Helbig, J. Sachs, R. Stephan, M.A. Hein, "Design and application of dielectrically scaled double-ridged horn antennas for biomedical UWB radar applications", 2009 IEEE International Conference on Ultra-Wideband ICUWB 2009, pp. 150-154

[13] F. Thiel, M.A. Hein, J. Sachs, U. Schwarz and F. Seifert: "Physiological signatures monitored by ultra-wideband-radar validated by magnetic resonance imaging", IEEE International Conference on Ultra-Wideband, ICUWB 2008, pp. 105-108

[14] The Visible Human Project, U.S. National Library of Medicine, 8600 Rockville Pike, Bethesda, MD 20894

[15] U. Schwarz, M. Helbig, J. Sachs, F. Seifert, R. Stephan, F. Thiel, M.A. Hein, "Physically small and adjustable double-ridged horn antenna for biomedical UWB radar applications", IEEE International Conference on Ultra-Wideband, ICUWB 2008, pp. 5-8

[16] H. Schantz, "Ultrawideband Antennas", Artech House, Inc., 2005

[17] MRA Laboratories, Adams, MA, USA. Available online: www.mralabs.com (accessed May 2012)

[18] J. Krupka, R.G. Geyer, J. Baker-Jarvis, J. Ceremuga, "Measurements of the complex permittivity of microwave circuit board substrates using split dielectric resonator and reentrant cavity techniques", 7th International Conference on Dielectric Materials, Measurements and Applications, (Conf. Publ. No. 430), 1996, pp. 21-24

[19] R.E. Collin, "Foundations for microwave engineering", 2nd ed., McGraw-Hill, 1992

[20] J. Krupka, "Computations of Frequencies and Intrinsic Q Factors of TE0nm Modes of Dielectric Resonators", IEEE Transactions on Microwave Theory and Techniques, 1985, pp. 247-277

[21] F. Scotto di Clemente, R. Stephan, and M. Hein, "Compact permittivity-matched ultra-wideband antennas for biomedical imaging", Topical Conference on Antennas and Propagation in Wireless Communications (APWC), 2011 IEEE-APS, pp. 858-860

[22] F. Scotto di Clemente, M. Helbig, J. Sachs, U. Schwarz, R. Stephan, M.A. Hein, "Permittivity-matched compact ceramic ultra-wideband horn antennas for biomedical diagnostics", Proceedings of the 5th European Conference on Antennas and Propagation (EUCAP), pp. 2386-2390

[23] U. Schwarz, R. Stephan, M.A. Hein, "Miniature double-ridged horn antennas composed of solid high-permittivity sintered ceramics for biomedical ultra-wideband radar applications", 2010 IEEE Antennas and Propagation Society International Symposium (APSURSI), 2010, pp. 1-4

[24] M. Lazebnik, E. Madsen EL, G. Frank, S. Hagness, "Tissue-mimicking phantom materials for narrowband and ultra-wideband microwave applications", Physics in Medicine and Biology 2005; 50:4245-4258.

[25] C. Geyer, "Wechselwirkungen von elektromagnetischen Wellen im Radiofrequenzbereich mit biologischen Systemen und lebenden Organismen," Dissertation, Biologisch-Pharmazeutische Fakultät, Friedrich-Schiller-Universität Jena, 2011.

[26] U. Schwarz, R. Stephan, M.A. Hein, "Experimental validation of high-permittivity ceramic double-ridged horn antennas for biomedical ultra-wideband diagnostics", IEEE

International Conference on Wireless Information Technology and Systems (ICWITS), 2010, pp. 1-4.

[27] M. Hein, M. Helbig, M. Kmec, J. Sachs, F. Scotto di Clemente, R. Stephan, M. Hamouda, T. Ussmueller, R. Weigel, M. Robens, R. Wunderlich, S. Heinen, "Ultra-Wideband Active Array Imaging for Biomedical Diagnostics", Topical Conference on Antennas and Propagation in Wireless Communications (APWC), 2012 IEEE-APS (Accepted).

[28] F. Scotto di Clemente, R. Stephan, U. Schwarz, M.A. Hein, " Miniature body-matched double-ridged horn antennas for biomedical UWB imaging", Topical Conference on Antennas and Propagation in Wireless Communications (APWC), 2012 IEEE-APS (Accepted)

[29] F. Thiel, M. Hein, J. Sachs, U. Schwarz, and F. Seifert, "Combining magnetic resonance imaging and ultrawideband radar: A new concept for multimodal biomedical imaging," Rev. Sci. Instrum., vol. 80, no. 1, 2009.

[30] O. Kosch, F. Thiel, F. Scotto di Clemente, M.A. Hein, F. Seifert, "Monitoring of human cardio-pulmonary activity by multi-channel UWB-radar", Topical Conference on Antennas and Propagation in Wireless Communications (APWC), 2011 IEEE-APS, pp.382-385

[31] U. Schwarz, F. Thiel, F. Seifert, R. Stephan, M. Hein, "Magnetic resonance imaging compatible ultra-wideband antennas," in 3rd Eur. Conf. on Antennas and Propagation, 2009, pp. 1102–1105.

[32] U. Schwarz, F. Thiel, F. Seifert, R. Stephan, M.A. Hein, "Ultra-Wideband Antennas for Magnetic Resonance Imaging Navigator Techniques", IEEE Trans. on Antennas and Propag, vol. 58, no. 6, June 2010.

[33] D. Miklavcic, N. Pavselj, and F. X. Hart, "Electrical properties of tissues," *Wiley Encyclopedia of Biomedical Engineering*, M. Akay, ed.: Wiley-Interscience, 2006.

[34] C. Gabriel, "Dielectric properties of biological tissue: Variation with age," *Bioelectromagnetics*, pp. S12-S18, 2005.

[35] G. H. Markx, and C. L. Davey, "The dielectric properties of biological cells at radiofrequencies: Applications in biotechnology," *Enzyme and Microbial Technology*, vol. 25, no. 3-5, pp. 161-171, Aug, 1999.

[36] R. Pethig, "Dielectric-Properties of Biological-Materials - Biophysical and Medical Applications," *IEEE Transactions on Electrical Insulation*, vol. 19, no. 5, pp. 453-474, 1984.

[37] H. P. Schwan, "Analysis of Dielectric Data - Experience Gained with Biological-Materials," *IEEE Transactions on Electrical Insulation*, vol. 20, no. 6, pp. 913-922, Dec, 1985.

[38] H. P. Schwan, and C. F. Kay, "The Conductivity of Living Tissues," *Annals of the New York Academy of Sciences*, vol. 65, no. 6, pp. 1007-1013, 1957.

[39] A. S. Arnoux, L. Preziosi-Belloy, G. Esteban *et al.*, "Lactic acid bacteria biomass monitoring in highly conductive media by permittivity measurements," *Biotechnology Letters*, vol. 27, no. 20, pp. 1551-1557, Oct, 2005.

[40] J. Yang, Y. Huang, X. J. Wang *et al.*, "Dielectric properties of human leukocyte subpopulations determined by electrorotation as a cell separation criterion," *Biophysical Journal*, vol. 76, no. 6, pp. 3307-3314, Jun, 1999.

[41] H. P. Schwan, "Mechanisms responsible for electrical properties of tissues and cell suspensions," *Med Prog Technol,* vol. 19, no. 4, pp. 163-5, 1993.

[42] S. R. Smith, and K. R. Foster, "Dielectric properties of low-water-content tissues," *Phys Med Biol,* vol. 30, no. 9, pp. 965-73, Sep, 1985.

[43] K. R. Foster, and H. P. Schwan, "Dielectric-Properties of Tissues and Biological-Materials - a Critical-Review," *Critical Reviews in Biomedical Engineering,* vol. 17, no. 1, pp. 25-104, 1989.

[44] J. A. Evans, S. L. Russell, C. James *et al.,* "Microbial contamination of food refrigeration equipment," *Journal of Food Engineering,* vol. 62, no. 3, pp. 225-232, May, 2004.

[45] M. Grossi, A. Pompei, M. Lanzoni *et al.,* "Total Bacterial Count in Soft-Frozen Dairy Products by Impedance Biosensor System," *IEEE Sensors Journal,* vol. 9, no. 10, pp. 1270-1276, Oct, 2009.

[46] Y. J. Chang, A. D. Peacock, P. E. Long *et al.,* "Diversity and characterization of sulfate-reducing bacteria in groundwater at a uranium mill tailings site," *Applied and Environmental Microbiology,* vol. 67, no. 7, pp. 3149-3160, Jul, 2001.

[47] S. K. Haack, L. R. Fogarty, T. G. West *et al.,* "Spatial and temporal changes in microbial community structure associated with recharge-influenced chemical gradients in a contaminated aquifer," *Environmental Microbiology,* vol. 6, no. 5, pp. 438-448, May, 2004.

[48] G. Haferburg, D. Merten, G. Buchel *et al.,* "Biosorption of metal and salt tolerant microbial isolates from a former uranium mining area. Their impact on changes in rare earth element patterns in acid mine drainage," *Journal of Basic Microbiology,* vol. 47, no. 6, pp. 474-484, Dec, 2007.

[49] S. E. Beekmann, D. J. Diekema, K. C. Chapin *et al.,* "Effects of rapid detection of bloodstream infections on length of hospitalization and hospital charges," *Journal of Clinical Microbiology,* vol. 41, no. 7, pp. 3119-3125, Jul, 2003.

[50] K. Mishima, A. Mimura, Y. Takahara *et al.,* "Online Monitoring of Cell Concentrations by Dielectric Measurements," *Journal of Fermentation and Bioengineering,* vol. 72, no. 4, pp. 291-295, 1991.

[51] C. M. Harris, R. W. Todd, S. J. Bungard *et al.,* "Dielectric Permittivity of Microbial Suspensions at Radio Frequencies - a Novel Method for the Real-Time Estimation of Microbial Biomass," *Enzyme and Microbial Technology,* vol. 9, no. 3, pp. 181-186, Mar, 1987.

[52] M. Jonsson, K. Welch, S. Hamp *et al.,* "Bacteria counting with impedance spectroscopy in a micro probe station," *Journal of Physical Chemistry B,* vol. 110, no. 20, pp. 10165-10169, May 25, 2006.

[53] E. Benoit, A. Guellil, J. C. Block *et al.,* "Dielectric permittivity measurement of hydrophilic and hydrophobic bacterial suspensions: a comparison with the octane adhesion test," *Journal of Microbiological Methods,* vol. 32, no. 3, pp. 205-211, May, 1998.

[54] Dahlke, K., Geyer, C.; Dees, S.; Helbig, M.; Sachs, J.; Scotto di Clemente, F.; Hein, M.; Kaiser, W.A.; Hilger, I.,"Effects of cell structure of Gram-positive and Gramnegative bacteria based on their dielectric properties," *The 7th German Microwave Conference (GeMiC), 2012,* 12-14 March 2012.

[55] F. Jaspard, and M. Nadi, "Dielectric properties of blood: an investigation of temperature dependence," *Physiological Measurement*, vol. 23, no. 3, pp. 547-554, Aug, 2002.

[56] H. F. Cook, "A Comparison of the Dielectric Behaviour of Pure Water and Human Blood at Microwave Frequencies," *British Journal of Applied Physics*, vol. 3, no. Aug, pp. 249-255, 1952.

[57] H. P. Schwan, and K. Li, "Capacity and Conductivity of Body Tissues at Ultrahigh Frequencies," *Proceedings of the Institute of Radio Engineers*, vol. 41, no. 12, pp. 1735-1740, 1953.

[58] H. P. Schwan, and K. R. Foster, "Rf-Field Interactions with Biological-Systems - Electrical-Properties and Biophysical Mechanisms," *Proceedings of the IEEE*, vol. 68, no. 1, pp. 104-113, 1980.

[59] L. Schmuntzsch, "Thermische Abhängigkeit der Permittivität in biologischem Gewebe," Diploma, Fachbereich Medizintechnik/ Biotechnologie, Fachhochschule Jena, Jena, 2010.

[60] A. Mashal, B. Sitharaman, X. Li *et al.*, "Toward Carbon-Nanotube-Based Theranostic Agents for Microwave Detection and Treatment of Breast Cancer: Enhanced Dielectric and Heating Response of Tissue-Mimicking Materials," *IEEE Transactions on Biomedical Engineering*, vol. 57, no. 8, pp. 1831-1834, Aug, 2010.

[61] Noeske R., Seifert F., Rhein K.H., Rinneberg H., "Human cardiac imaging at 3T using phased array coils", *Magn. Reson. Med*. 44, 978-82 (2000)

[62] Haacke E.M., Li D., Kaushikkar S., "Cardiac MR Imaging: Principles and Techniques". *Top Magn Reson Imaging* 7:200-17, (1995).

[63] Dieringer M.A., Renz W., Lindel T., Seifert F., Frauenrath T., von Knobelsdorff-Brenkenhoff F., Waiczies H., Hoffmann W., Rieger J., Pfeiffer H., Ittermann B., Schulz-Menger J., Niendorf T., "Design and application of a four-channel transmit/receive surface coil for functional cardiac imaging at 7T", *Journal of Magnetic Resonance Imaging* 33 (3): 736-741 (2011-03).

[64] Nijm G.M., Swiryn S., Larson A.C., and Sahakian A.V., "Characterization of the Magnetohydrodynamic Effect as a Signal from the Surface Electrocardiogram during Cardiac Magnetic Resonance Imaging", in *Computers in Cardiology*, Valencia, Spain, p. 269–272, (2006)

[65] Frauenrath T., Hezel F., Renz W., de Geyer T., Dieringer M., von Knobelsdorff-Brenkenhoff F., Prothmann M., Schulz-Menger J., Niendorf T., "Acoustic cardiac triggering: a practical solution for synchronization and gating of cardiovascular magnetic resonance at 7 Tesla", *Journal of Cardiovascular Magnetic Resonance* 12 (1): 67 (2010-11-16).

[66] van Geuns R.J., PA. Wielopolski, HG. de Bruin, et al: "MR coronary angiography with breath-hold targeted volumes: preliminary clinical results", *Radiology* (2000); 217:270–7

[67] Hinks, R.S.. "Monitored echo gating for reduction of motion artifacts". *Magn Reson Imaging*, 6(48), (1988).

[68] Thiel F., Kreiseler D., Seifert F., "Non-contact detection of myocardium's mechanical activity by ultra-wideband RF-radar and interpretation applying electrocardiography", *Rev. Sci. Instrum*., vol. 80, 11, 114302, ISSN 0034-6748, Melville, NY: American Institute of Physics (AIP), 12 pages, (2009)

[69] Morguet A.J.; Behrens S., Kosch O., Lange C., Zabel M., Selbig D., Munz D.L., Schultheiss H.P., Koch H.: "Myocardial viability evaluation using magnetocardiography in patients with coronary artery disease"; *Coron Artery Dis* 15, 2004: 155 – 162

[70] Muehlsteff J., Thijs J., Pinter R., Morren G., Muesch G., "A handheld device for simultaneous detection of electrical and mechanical cardio-vascular activities with synchronized ECG and CW-Doppler Radar", *IEEE Int. Conf. Engineering in Medicine and Biology Society* (EMBS) 22-26 Aug. (2007), 5758 – 5761

[71] Thiel F. and Seifert F., "Non-invasive probing of the human body with electromagnetic pulses: Modelling of the signal path", *J. Appl. Phys.*, vol.105, issue 4, 044904, ISSN 0021-8979, Melville, NY, American Institute of Physics (AIP), 8 pages, (2009)

[72] Thiel F. and Seifert F., "Physiological signatures reconstructed from a dynamic human model exposed to ultra-wideband microwave signals", *Frequenz, Journal of RF/Microwave-Engineering, Photonics and Communications*, vol. 64, no. 3-4, 34-41, ISSN 0016-1136, (2010).

[73] Thiel F., Kosch O., Seifert F., "Ultra-wideband Sensors for Improved Magnetic Resonance Imaging, Cardiovascular Monitoring and Tumour Diagnostics", Special Issue "*Sensors in Biomechanics and Biomedicine*", 10, 12, 10778-10802, doi:10.3390/s101210778, ISSN 1424-8220, 25 pages, (2010)

[74] Kosch O., Thiel F., Yan D.D., and Seifert F., "Discrimination of respirative and cardiac displacements from ultra-wideband radar data", *Int. Biosignal Processing Conf.* (Biosignal 2010), 14th – 16th July; Berlin, Germany, (2010)

[75] Christ A. et al., "The virtual family – development of surface-based anatomical models of two adults and two children for dosimetric simulations", *Phys. Med. Biol.* 55, N23-N38, (2010)

[76] Sachs J., Peyerl P., Wöckel S., et al., "Liquid and moisture sensing by ultra-wideband pseudo-noise sequence signals", *Meas. Sci. Technol.*, vol. 18, no. 4, pp. 1074-1088, April 2007.

[77] Kosch O., Thiel F., Schneider S., Ittermann B., and Seifert F., "Verification of contactless multi-channel UWB navigator by one dimensional MRT", *Proc. Intl. Soc. Mag. Reson. Med.* 20, (ISMRM), Melbourne, Australia, p.601, (2012)

[78] Ziehe A. and Müller K.R., TDSEP - "An efficient algorithm for blind separation using time structure", *Proc. Int. Conf. Artifical Neural Networks* (ICANN'98), Skövde, Sweden, pp.675-680, (1998).

[79] Sander T.H., Lueschow A., Curio G., Trahms L., "Time delayed decorrelation for the identification of the cardiac artifact in MEG data", *Biomed. Tech.* 2002, 47(1/2), pp. 573-576, (2002).

[80] Kosch O., Schneider S., Ittermann B., and Seifert F., "Self-adjusting multichannel UWB radar for cardiac MRI", *Proc. Intl. Soc. Mag. Reson. Med.* 20, (ISMRM), Melbourne, Australia, p.2467, (2012)

[81] Kosch O., Thiel F., Ittermann B., and Seifert F., "Non-contact cardiac gating with ultra-wideband radar sensors for high field MRI", *Proc. Intl. Soc. Mag. Reson. Med.* 19, (ISMRM), Montreal, Canada, ISSN 1545-4428, p.1804, (2011)

[82] M. Helbig, "Mikrowellen- Ultrabreitband- und THz-Bildgebung," in O. Dössel, T. M. Buzug, (Hrsg.) "Medizinische Bildgebung", Lehrbuchreihe der Biomedizinischen Technik, Bd. 7, Berlin, de Gruyter, 2012

[83] E. C. Fear, S. C. Hagness, P. M. Meaney *et al.*, "Enhancing breast tumor detection with near-field imaging," *Microwave Magazine, IEEE,* vol. 3, no. 1, pp. 48-56, 2002.

[84] P. M. Meaney, M. W. Fanning, D. Li *et al.*, "A clinical prototype for active microwave imaging of the breast," *IEEE Transactions on Microwave Theory and Techniques,* vol. 48, no. 11, pp. 1841-1853, Nov, 2000.

[85] M. Klemm, I. J. Craddock, J. A. Leendertz *et al.*, "Radar-Based Breast Cancer Detection Using a Hemispherical Antenna Array - Experimental Results," *IEEE Transactions on Antennas and Propagation,* vol. 57, no. 6, pp. 1692-1704, 2009.

[86] M. Klemm, I. J. Craddock, J. A. Leendertz *et al.*, "Clinical trials of a UWB imaging radar for breast cancer," *Proceedings of the Fourth European Conference on Antennas and Propagation (EuCAP),* 2010, pp. 1-4.

[87] J. Sachs, "M-sequence radar," *Ground penetrating radar*, D. J. Daniels, ed., pp. 225-237, London: The Institution of Engineering and Technology, 2004.

[88] U. Kaatze, "Complex permittivity of water as a function of frequency and temperature," *J Chem Eng Data,* vol. 34, no. 4, pp. 371-374, Oct, 1989.

[89] T. C. Williams, J. Bourqui, T. R. Cameron *et al.*, "Laser Surface Estimation for Microwave Breast Imaging Systems," *IEEE Transactions on Biomedical Engineering,* vol. 58, no. 5, pp. 1193-1199, 2011.

[90] D. W. Winters, J. D. Shea, P. Kosmas *et al.*, "Three-Dimensional Microwave Breast Imaging: Dispersive Dielectric Properties Estimation Using Patient-Specific Basis Functions," *IEEE Transactions on Medical Imaging,* vol. 28, no. 7, pp. 969-981, 2009.

[91] T. Sakamoto, and T. Sato, "A target shape estimation algorithm for pulse radar systems based on boundary scattering transform," *IEICE Transactions on Communications,* vol. E87b, no. 5, pp. 1357-1365, May, 2004.

[92] S. Kidera, Y. Kani, T. Sakamoto *et al.*, "Fast and accurate 3-D imaging algorithm with linear array antennas for UWB pulse radars," *IEICE Transactions on Communications,* vol. E91b, no. 8, pp. 2683-2691, Aug, 2008.

[93] M. Helbig, M. A. Hein, U. Schwarz *et al.*, "Preliminary investigations of chest surface identification algorithms for breast cancer detection," *IEEE International Conference on Ultra-Wideband, ICUWB 2008*, pp. 195-198.

[94] M. Helbig, C. Geyer, M. Hein *et al.*, "A Breast Surface Estimation Algorithm for UWB Microwave Imaging," IFMBE Proceedings 4th European Conference of the International Federation for Medical and Biological Engineering, J. Sloten, P. Verdonck, M. Nyssen *et al.*, eds., pp. 760-763: Springer Berlin Heidelberg, 2009.

[95] M. Helbig, C. Geyer, M. Hein *et al.*, "Improved Breast Surface Identification for UWB Microwave Imaging," IFMBE Proceedings World Congress on Medical Physics and Biomedical Engineering, September 7 - 12, 2009, Munich, Germany, O. Dössel and W. C. Schlegel, eds., pp. 853-856: Springer Berlin Heidelberg, 2009.

[96] S. Hantscher, B. Etzlinger, A. Reisenzahn *et al.*, "A Wave Front Extraction Algorithm for High-Resolution Pulse Based Radar Systems," *IEEE International Conference on Ultra-Wideband, ICUWB 2007*, pp. 590-595.

[97] J. Sachs, R. Herrmann, M. Kmec *et al.*, "Recent Advances and Applications of M-Sequence based Ultra-Wideband Sensors," *IEEE International Conference on Ultra-Wideband, ICUWB 2007*, pp. 50-55.

[98] M. Helbig, " UWB for Medical Microwave Breast Imaging," in J. Sachs, "*High-Resolution Short-Range Sensing - Basics, Principles and Applications of Ultra Wideband Sensors*, Berlin: Wiley-VCH, 2012

[99] E. J. Bond, X. Li, S. C. Hagness *et al.*, "Microwave imaging via space-time beamforming for early detection of breast cancer," *IEEE Transactions on Antennas and Propagation*, vol. 51, no. 8, pp. 1690-1705, Aug, 2003.

[100] Y. Xie, B. Guo, L. Xu *et al.*, "Multistatic Adaptive Microwave Imaging for Early Breast Cancer Detection," *IEEE Transactions on Biomedical Engineering*, vol. 53, no. 8, pp. 1647-1657, 2006.

[101] R. Zetik, J. Sachs, and R. Thoma, "Modified cross-correlation back projection for UWB imaging: numerical examples," *IEEE International Conference on Ultra-Wideband, ICU 2005*, pp. 650-654.

[102] M. Klemm, I. J. Craddock, J. A. Leendertz *et al.*, "Improved Delay-and-Sum Beamforming Algorithm for Breast Cancer Detection," *International Journal of Antennas and Propagation*, vol. 2008.

[103] M. Kmec, M. Helbig, J. Sachs et al., "Integrated ultra-wideband hardware for MIMO sensing using pn-sequence approach," *IEEE International Conference on Ultra-Wideband*, ICUWB 2012, Syracuse, USA, 17-20 Sept. 2012

[104] M. Helbig, I. Hilger, M. Kmec, *et al.*, "Experimental phantom trials for UWB breast cancer detection", *Proc. German Microwave Conf.*, Ilmenau, Germany, pp. 1-4, 12-14 March 2012.

[105] M. Helbig, M. Kmec, J. Sachs *et al.*, "Aspects of antenna array configuration for UWB breast imaging," Proc. European Conf. on Antennas and Propagation, EuCAP 2012, Prague, pp. 1-4, 26-30 March 2012.

[106] M. Helbig, M. A. Hein, R. Herrmann *et al.*, "Experimental active antenna measurement setup for UWB breast cancer detection," *IEEE International Conference on Ultra-Wideband*, ICUWB 2012, Syracuse, USA, 17-20 Sept. 2012

[107] M. Lazebnik, D. Popovic, L. McCartney *et al.*, "A large-scale study of the ultrawideband microwave dielectric properties of normal, benign and malignant breast tissues obtained from cancer surgeries," *Physics in Medicine and Biology*, vol. 52, no. 20, pp. 6093-6115, Oct 21, 2007.